
Measurements and simulations of drift gas properties

von

Lukas KOCH

MASTERARBEIT IN PHYSIK

vorgelegt der

FAKULTÄT FÜR MATHEMATIK, INFORMATIK UND NATURWISSENSCHAFTEN
der RWTH AACHEN

im September, 2013

angefertigt im

III. PHYSIKALISCHEN INSTITUT B

bei

PD Dr. Stefan ROTH

Abstract

For the successful design and operation of gas based particle detectors, one needs a good understanding of the drift properties of the deployed gas. This includes the drift velocity of electrons, their diffusion and the gas amplification in different electric and magnetic fields.

This work presents simulations and precision measurements of the drift velocity v_d in low electric fields ($< 400 \text{ V/cm}$) for argon-based gas mixtures with up to two additives. The additives used are CH_4 , CO_2 , CF_4 , iC_4H_{10} and H_2 .

The simulations were done using Garfield++ and Magboltz. The measurements were taken with T2K/ND280-type monitoring drift chambers, which allow v_d measurements in the range of about $20 \mu\text{m/ns} - 100 \mu\text{m/ns}$. Experiment and simulation are in good agreement and most remaining deviations are below $1 \mu\text{m/ns}$. To make the obtained data available for interested parties, a database was established at <http://web.physik.rwth-aachen.de/gasDB/>.

Finally, a promising method for the measurement of the first Townsend coefficient α_T is presented.

Contents

List of figures	7
1. Introduction	9
1.1. Electron transport in gases	9
1.1.1. Primary and secondary ionisation	9
1.1.2. Electron drift in an electric field	11
1.1.3. Diffusion	13
1.1.4. Influence of a magnetic field	15
1.1.5. Gas amplification at high electric fields	15
1.2. Examples of gas based particle detectors	16
1.2.1. Drift tubes	16
1.2.2. Time projection chambers	17
2. Setup	21
2.1. The drift chambers	21
2.2. DAQ	21
2.3. Gas mixing	23
2.4. Simulation software	25
2.5. Calibration and systematic errors	26
2.5.1. Drift length	27
2.5.2. Timing	27
2.5.3. Electric field	27
2.5.4. Temperature	28
2.5.5. Pressure	28
2.6. Putting it all together	32
3. Results	33
3.1. Ar-CH ₄ -CO ₂ mixtures	33
3.2. Ar-CF ₄ -iC ₄ H ₁₀ mixtures	38
3.3. Ar-CH ₄ -H ₂ mixtures	40
4. Measuring the first Townsend coefficient	45
4.1. Theory	46
4.2. Modifications	47
4.3. Future improvements	52
5. Conclusion	53
6. Acknowledgements	55

References	57
A. Gas properties	59
B. Measurements	61
B.1. Ar-CH ₄ -CO ₂ mixtures	61
B.2. Ar-CF ₄ -iC ₄ H ₁₀ mixtures	80
B.3. Ar-CH ₄ -H ₂ mixtures	91

List of figures

1.1. Particle identification by energy loss and momentum	10
1.2. Energy loss of antimuons in copper	10
1.3. Electron cross-sections for argon and methane	14
1.4. A drift tube of the CMS muon system	17
1.5. Principle of operation of time projection chambers	18
1.6. The T2K/ND280 TPCs	19
2.1. Schematic view and picture of the used drift chambers	22
2.2. Schematic view and picture of a MicroMeGaS	22
2.3. DAQ setup	23
2.4. Histogram of measured drift times	24
2.5. Picture of the experimental setup	24
2.6. Field strips of unassembled field cage	28
2.7. Temperature curve of a DS18S20 temperature sensor in melting ice	29
2.8. Pressure distribution at calibration points	29
2.9. Jump in pressure signals due to missing codes in the ADCs	30
2.10. Correlation between pressure signals for different offset corrections	31
2.11. Histogram of pressures before and after ADC correction	31
3.1. Example of raw v_d measurements with Ar 93 % – CH ₄ 7 %	34
3.2. Example “condensed” v_d measurements with Ar 93 % – CH ₄ 7 %	34
3.3. v_d measurements and simulations of P5, P10, P15, P20 and P25	35
3.4. v_d curve shape examples	36
3.5. Example working point fit for Ar 93 % – CH ₄ 7 %	37
3.6. Working points for Ar-CH ₄ -CO ₂ mixtures	37
3.7. Working points for Ar-CH ₄ -CO ₂ mixtures in dependence of η	38

3.8. v_d curve of Ar 95 % – CF ₄ 3 % – iC ₄ H ₁₀ 2 %, also known as T2K-gas	39
3.9. Working points for Ar-CF ₄ -iC ₄ H ₁₀ mixtures	39
3.10. Working points for Ar-CF ₄ -iC ₄ H ₁₀ mixtures in dependence of η	40
3.11. Working points for Ar-CH ₄ -H ₂ mixtures	41
3.12. Working points for Ar-CH ₄ -H ₂ mixtures in dependence of η	41
3.13. Fit to very wide maximum of Ar 89 % – CH ₄ 5 % – H ₂ 6 %	42
3.14. Influence of the H ₂ fraction on Ar-CH ₄ -H ₂ mixtures with 4 % CH ₄	42
3.15. Ar-CH ₄ -H ₂ mixtures that show a wide v_d plateau	43
3.16. Behaviour of Ar-CH ₄ -H ₂ plateau mixtures up to very high E -fields (simulations only)	43
4.1. Measurements of the MicroMeGaS geometry	45
4.2. Experimental setup by Auriemma et al.	46
4.3. Modified setup for the α_T measurement	48
4.4. Typical light bulb filament before and after the use as hot cathode in gas	48
4.5. Measured and corrected anode current of P5	49
4.6. Anode current vs voltage of P5	50
4.7. Measured and simulated α_T of P5	50
4.8. Measured and simulated α_T of P7	51
4.9. Proposed upgrade of the α_T measurement setup	52
5.1. Simplified influences of the additives on the working points	53

1. Introduction

Gas based particle detectors have proven to be a reliable technology and offer a few advantages over other detector technologies:

- They allow large sensitive volumes with very little material in the particles' path.
- Utilising gas amplification, one can use less sensitive electronic amplification.
- They can measure the energy loss of the particle. Together with a momentum measurement (reconstructed track in a magnetic field), this allows particle identification (see figure 1.1).
- In the case of TPCs¹, they offer a fine track reconstruction with comparatively few read-out channels.

To make use of these advantages, one needs a good understanding of the properties of the employed gas mixture. This includes everything from the first ionisation of the gas by a passing high energy particle, to the signal generation when the created free electrons are amplified and collected at the anode. This thesis will concentrate on the transportation of the electrons from the place of ionisation to the amplification region, namely it will study the drift velocity. In addition, this chapter will give a short overview over the whole process from ionisation to detection.

1.1. Electron transport in gases

The transport of electrons in a gas is a very complex process and this introduction can only cover the most important derivations and results. For an in-depth discussion of the processes involved, please refer to reference [2], as most of the following is taken from there.

1.1.1. Primary and secondary ionisation

When high energy charged particles traverse a gas, they lose energy due to interactions with the matter. Depending on the particle's energy, different processes contribute to the energy loss (see figure 1.2). This energy excites the gas molecules and if the incident particle's energy is high enough, some of the deposited energy goes into ionising the molecules along its trajectory. One distinguishes between primary and secondary ionisation. Primary ionisation is the direct ionisation of a gas molecule A by a passing charged particle P^\pm .

$$P^\pm + A \rightarrow P^\pm + A^+ + e^-$$

¹Time Projection Chamber

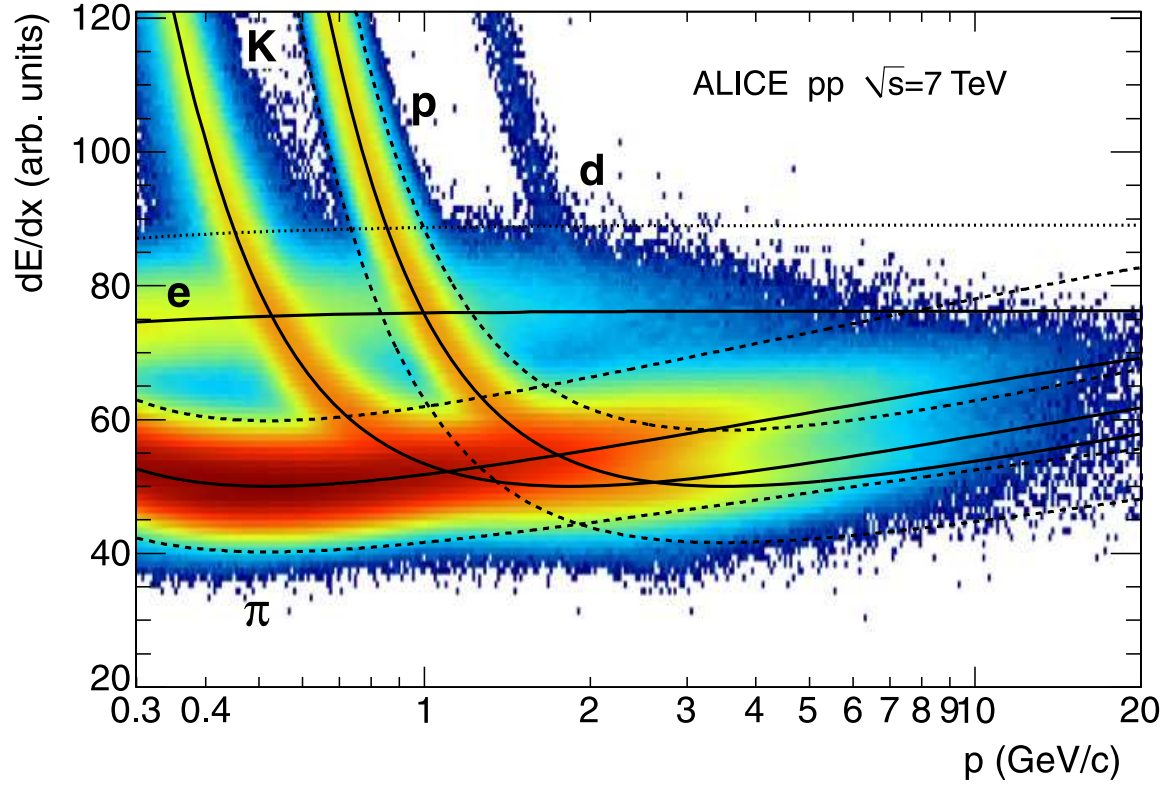


Figure 1.1.: Particle identification by energy loss and momentum [1]

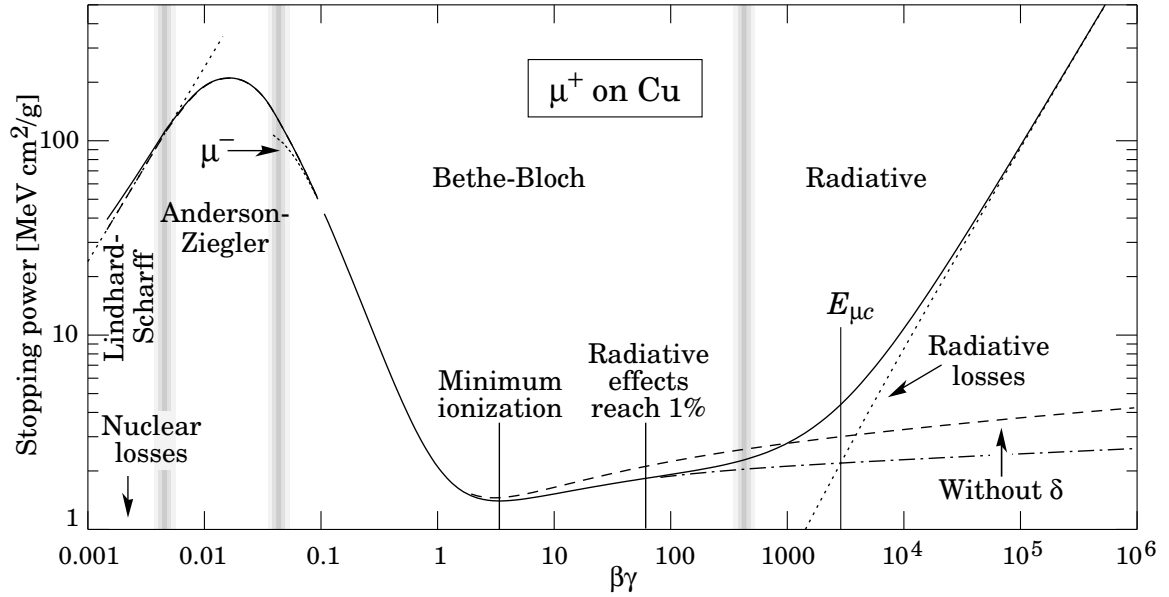
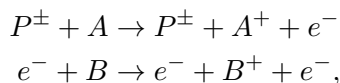
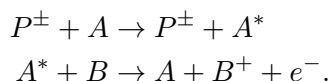


Figure 1.2.: Energy loss of antimuons in copper [3]. The behaviour is very similar for other particles and materials.

Secondary ionisation occurs if a molecule is not ionised directly by the passing particle, but by a product of the interaction with another molecule. This can either be a comparatively highly energetic ionisation electron, also called δ -electron,



or an excited state of a molecule,



In the latter case, the ionisation energy of molecule B must be lower than the energy of the excited state A^* . Ionisation by excited gas molecules is known as Penning effect, if the energy transfer from A^* to B happens through a collision, or Jesse effect, if it happens via an emitted photon. Most ionisation electrons along a particle track are created by secondary ionisation.

By measuring the separated charge along the particle track, one can reconstruct the energy loss of the ionising particle. Unfortunately, only a certain fraction of the energy that a particle loses when traveling through the gas does go into ionisation of the gas molecules. Therefore, one cannot simply use the ionisation energies of the gases to derive the energy loss. For a correct calculation, one has to use the average energy W that is needed to produce one ionisation pair. If a particle traverses a distance L in a gas mixture, it will, on average, lose the energy $\langle \Delta E \rangle$ and produce $\langle N \rangle$ ion electron pairs. W is then the ratio of energy loss to the number of produced ionisation pairs:

$$W = \frac{\langle \Delta E \rangle}{\langle N \rangle} = \left\langle \frac{dE}{dx} \right\rangle \frac{L}{\langle N \rangle}$$

This value depends on the type of ionising particle, its energy and, of course, the gas mixture that is being ionised. The energy dependence vanishes for high energies, i.e. a few keV for ionising electrons and a few MeV for ionising alpha particles. If one knows W (through measurement or simulation), one can use it to reconstruct the energy loss of the traversing particle by measuring the ionisation charges that were separated along its track. This information can then be used to identify the particle. Typical values of W range between 20 eV and 50 eV (see appendix A).

1.1.2. Electron drift in an electric field

To prevent the ion-electron-pairs from recombining and to transport the electrons to an anode where the charge can be measured, one applies an electric field to the gas. The electrons will then drift along the field lines² towards the anode.

On their way the electrons collide with gas molecules, and due to the large mass difference between molecules and electrons, they are scattered isotropically with an average instantaneous microscopic velocity v_{inst} . This velocity does not directly contribute to the drift

²For now we assume that there is no magnetic field present.

velocity v_d , due to the isotropic nature of the scattering. Between collisions the electrons, and thus their mean position \bar{z} , are accelerated by the electric field in the z -direction. This macroscopic movement is stopped at the next collision, when the direction is randomised again. The time between two collisions t is exponentially distributed with the mean value τ . The additional velocity that has been picked up during that time is the macroscopic drift velocity v_d .

$$v_d = \frac{\langle \Delta \bar{z} \rangle}{\langle t \rangle} = \frac{\langle \frac{1}{2} a t^2 \rangle}{\langle t \rangle} = \frac{\frac{1}{2} a \langle t^2 \rangle}{\langle t \rangle} = \frac{\frac{1}{2} a 2 \tau^2}{\tau} = \frac{eE}{m_e} \tau \quad (1.1)$$

This additional velocity corresponds to an energy gain of the electron. In equilibrium, when the drift velocity and the electron energy ε are constant over time, this additional energy must (on average) be lost at the next collision. We therefore introduce the average fractional energy loss per collision λ . The energy gained from drifting a distance Δz through the electric field must be equal to the energy loss due to collisions with the gas molecules:

$$eE\Delta z = \varepsilon \lambda \frac{\Delta z}{v_d \tau} \quad (1.2)$$

The mean time between collisions can be expressed with the microscopic velocity v_{inst} , the number density of gas molecules n and the cross-section of the scattering process σ .

$$\tau = \frac{1}{v_{\text{inst}} n \sigma} \quad (1.3)$$

The electron energy ε is also a function of v_{inst} .

$$\varepsilon = \frac{1}{2} m_e v_{\text{inst}}^2 \quad (1.4)$$

Combining equations (1.1) through (1.4) yields the following expression:

$$v_d^2 = v_{\text{inst}}^2 \frac{\lambda}{2} = \frac{e}{m_e \sigma} \sqrt{\frac{\lambda}{2}} \frac{E}{n}$$

These equations suggest a proportional relationship between E and v_d^2 , but σ and λ strongly depend on the electron energy ε and thus on v_{inst} . One often combines these dependencies into the electron mobility μ which is then a function of E/n .

$$v_d = \sqrt{\frac{e}{m_e \sigma} \sqrt{\frac{\lambda}{2}} \frac{n}{E} \frac{E}{n}} = \mu(E/n) \frac{E}{n}$$

Up to now we assumed that all electrons behave like the average electron with a single distinct value of v_{inst} and thus σ and λ . In reality these values are statistically distributed and this has to be considered in the calculations. A calculation that takes the distribution of v_{inst} into account, but assumes constant σ and λ , yields [2, p.81]

$$\begin{aligned} \langle v_{\text{inst}}^2 \rangle &= 0.854 \frac{e}{m_e \sigma} \sqrt{\frac{2}{\lambda}} \frac{E}{n}, \\ v_d^2 &= 0.855 \frac{e}{m_e \sigma} \sqrt{\frac{\lambda}{2}} \frac{E}{n}. \end{aligned} \quad (1.5)$$

It is noteworthy that the dependency on the electric field E only appears in the fraction E/n . Hence, if the density of a drift gas changes (due to temperature or pressure changes), one can compensate for that by changing the electric field accordingly.

For an exact reproduction of the real behaviour of electrons in the field, one has to consider the (energy dependent) cross-sections of all relevant elastic scattering, excitation and ionisation processes of the different gases in the mix. This can only be done numerically. Figure 1.3 shows example cross-sections for argon and methane.

The prominent dip in the elastic scattering cross-section at around 0.2 eV is called the Ramsauer minimum. According to equation (1.5), a low σ means a high drift velocity, but argon has no excitation states in that energy region. Therefore, the electrons lose only very little energy in the elastic collisions and will quickly be accelerated beyond the Ramsauer minimum to higher energies and slower drift velocity.

Methane, on the other hand, has considerable cross-sections for inelastic processes in that energy region. So by adding methane to the gas mixture, one can lower the average electron energy towards the Ramsauer minimum, thereby increasing the drift velocity. This is the general principle of drift gas mixtures, the details of which depend on the excitation states and cross-sections of the deployed gases. Usually the drift velocity increases with increasing electric field and then reaches a plateau or a maximum due to combined effects of the elastic and inelastic scattering cross-sections.

1.1.3. Diffusion

Due to the random isotropic scattering of the electrons, the electron cloud traversing the drift volume will diffuse. In the simplest case, we can assume the diffusion to be isotropic while the electron cloud as a whole drifts through the gas with the velocity v_d . The electron number is conserved, so the current density \vec{j} and number density n_e have to satisfy the following equations:

$$\frac{\partial n_e}{\partial t} + \vec{\nabla} \cdot \vec{j} = 0 \quad (1.6)$$

$$\vec{j} + D\vec{\nabla}n_e = 0 \quad (1.7)$$

Here D is the diffusion constant. Combining (1.6) and (1.7) we get

$$\frac{\partial n_e}{\partial t} - D\Delta n_e = 0.$$

For an initially point-like electron cloud that is created at $x = y = z = t = 0$, this equation is satisfied by the Gaussian distribution

$$n_e = \left(\frac{1}{\sqrt{4\pi Dt}} \right)^3 \exp \left(\frac{-r^2}{4Dt} \right),$$

where $r^2 = x^2 + y^2 + (z - v_d t)^2$ is the distance from centre of the drifting electron cloud. The mean squared deviation from the centre (in any direction) is thus

$$\sigma_r^2 = 2Dt.$$

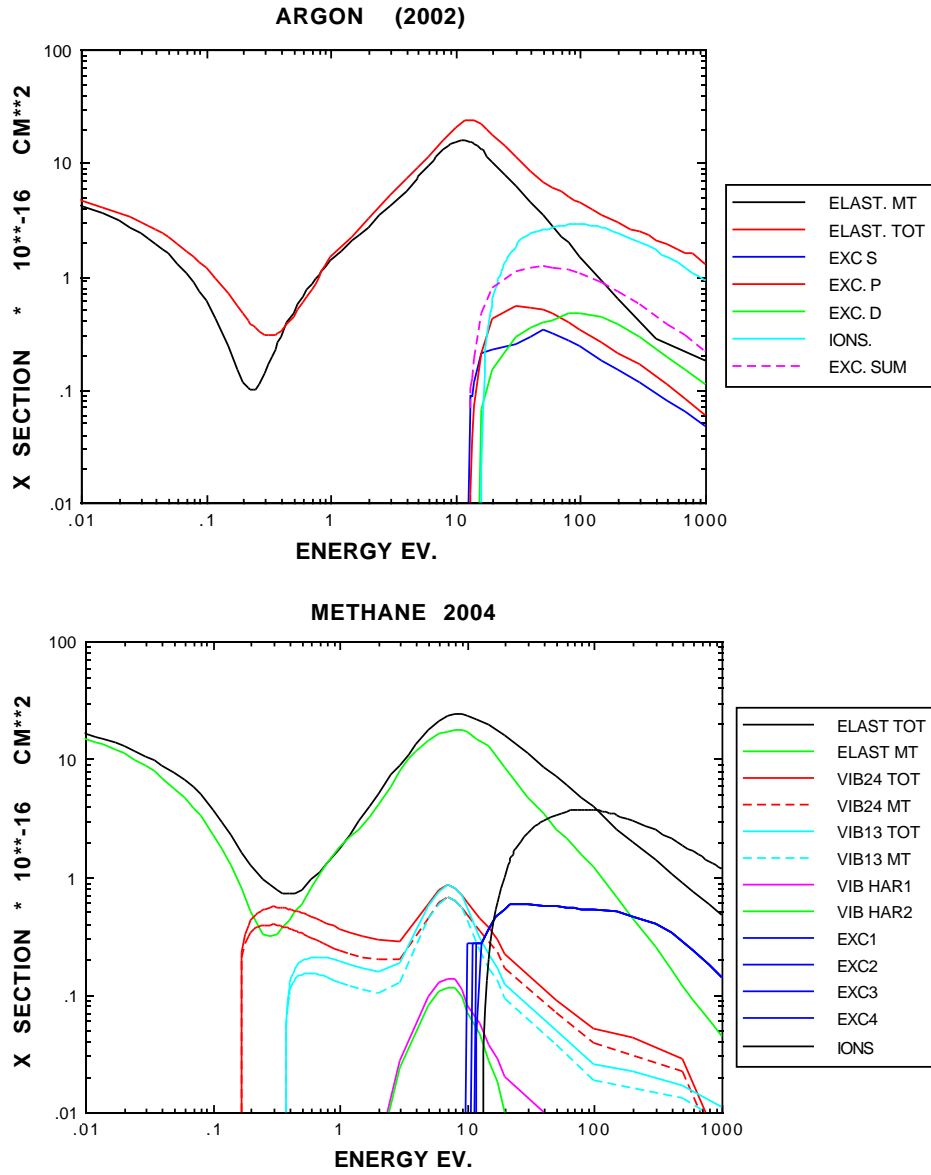


Figure 1.3.: Elastic and inelastic electron cross-sections for argon and methane in dependence of the electron energy [4]

Further calculations reveal that the diffusion constant depends on the microscopic electron velocity v_{inst} and the mean free drift time τ [2, p. 68]:

$$D = \frac{v_{\text{inst}}^2 \tau}{3} \stackrel{(1.3)}{=} \frac{v_{\text{inst}}}{3n\sigma}$$

Please note that n is the number density of gas molecules, while n_e denotes the number density of the drifting electrons. This simple relationship again assumes a singular value of v_{inst} and more complicated calculations have to be performed in order to take the v_{inst} distribution into account. Also, due to the differential movement of the electron cloud with respect to the gas, the diffusion is not exactly isotropic. Electrons moving parallel to the direction of drift have a higher v_{inst} with respect to the gas than electrons moving antiparallel to v_d .

Sometimes it is more useful to treat the diffusion as dependent from the drift length and not the time, e.g. when choosing a gas mixture for a detector of given length. Since the electron cloud is drifting at a constant velocity v_d , the relation is simple:

$$\sigma_r = \sqrt{2Dt} = \underbrace{\sqrt{\frac{2D}{v_d}}}_{:=d} \sqrt{\Delta z} = d\sqrt{\Delta z}$$

The unit of the new diffusion constant d is $\sqrt{\text{cm}}$.

1.1.4. Influence of a magnetic field

If one also applies a magnetic field to the drift volume, the rotational symmetry around the E -field vector is broken³ and the drift direction is not parallel to the E -field anymore. Mathematically we take this into account by replacing the scalar electron mobility μ from (1.5) with a tensor $\boldsymbol{\mu}$ and treating the drift velocity and E -field as the vector quantities they are.

$$\vec{v}_d = \boldsymbol{\mu}(E/n, B/n, \varphi) \frac{\vec{E}}{n}$$

Here φ denotes the angle between E - and B -field.

The diffusion gets treated similarly and we replace the scalar diffusion constant with a tensor. The mean squared deviation of the cloud in the direction \vec{e} is then

$$\sigma_e^2 = 2\vec{e}\mathbf{D}(E/n, B/n, \varphi)\vec{e}t.$$

1.1.5. Gas amplification at high electric fields

Once the electrons reach the anode, they create an electric signal. But without amplification, the charge created by the ionising particle would not be sufficient for a reliable detection. One can use gas amplification to boost the signal into regions that are more easily detectable by electronic readouts.

³With the exception of $\vec{E} \parallel \vec{B}$, of course.

In high electric fields, the electron energy ε will be sufficient to ionise gas molecules, thus creating more free electrons. Those electrons will then ionise even more gas molecules and so on. This exponential amplification process is called an electron cascade.

Mathematically the amplification is described by the so called Townsend coefficient α_T . It describes the number of ionisations by a single electron per unit length. The ionisation cross-section is energy dependent and thus a function of E/n . Additionally the ionisation rate is proportional to the number density of gas molecules, so the functional dependence of α_T can be written as

$$\alpha_T(E/n, n) = \left\langle \frac{N}{\Delta z} \right\rangle = f(E/n) n,$$

where N is the number of ionisations along the drift length Δz . The gain factor G can then be calculated from the integrated Townsend coefficient along the drift path.

$$G = \left\langle \frac{N_e}{N_{e,0}} \right\rangle = \exp \left(\int \alpha_T(E(z)/n, n) dz \right)$$

Here $N_{e,0}$ and N_e are the total number of free electrons before and after the amplification.

In principle, it is possible to calculate α_T just like v_d if one knows the cross-sections for the scattering and ionisation processes. But the ionisation rate calculated this way only covers direct ionisation by the electrons and, as described in section 1.1.1, a large fraction of the separated charges is produced by indirect secondary ionisation. The Penning and Jesse effects, at the moment, cannot be calculated and have to be measured. Mathematically they are modelled by a probability P that an excited gas molecule with an excitation energy over the lowest ionisation energy in the gas mix will produce a secondary ionisation.

$$P = \left\langle \frac{N_{e,sec}}{N_{E>E_{min}}^*} \right\rangle$$

Here $N_{E>E_{min}}^*$ is the number of excited molecules with an excitation energy above the lowest ionisation potential in the gas mixture and $N_{e,sec}$ is the number of free electrons produced by the Penning and Jesse effects.

Gas amplification starts in electric fields of the order of 10 kV/cm. To create such high fields without having to create unmanageable voltages, one uses small structures such as thin wires or micro patterns.

1.2. Examples of gas based particle detectors

1.2.1. Drift tubes

Drift tubes are probably the simplest type of gas-based particle detectors that use the drift velocity of the electrons to reconstruct the ionising particles location. They consist of an anode wire inside a gaseous volume that is encased by a cathode. If one knows the time of the ionisation and the drift velocities in the volume, one can reconstruct the distance of the

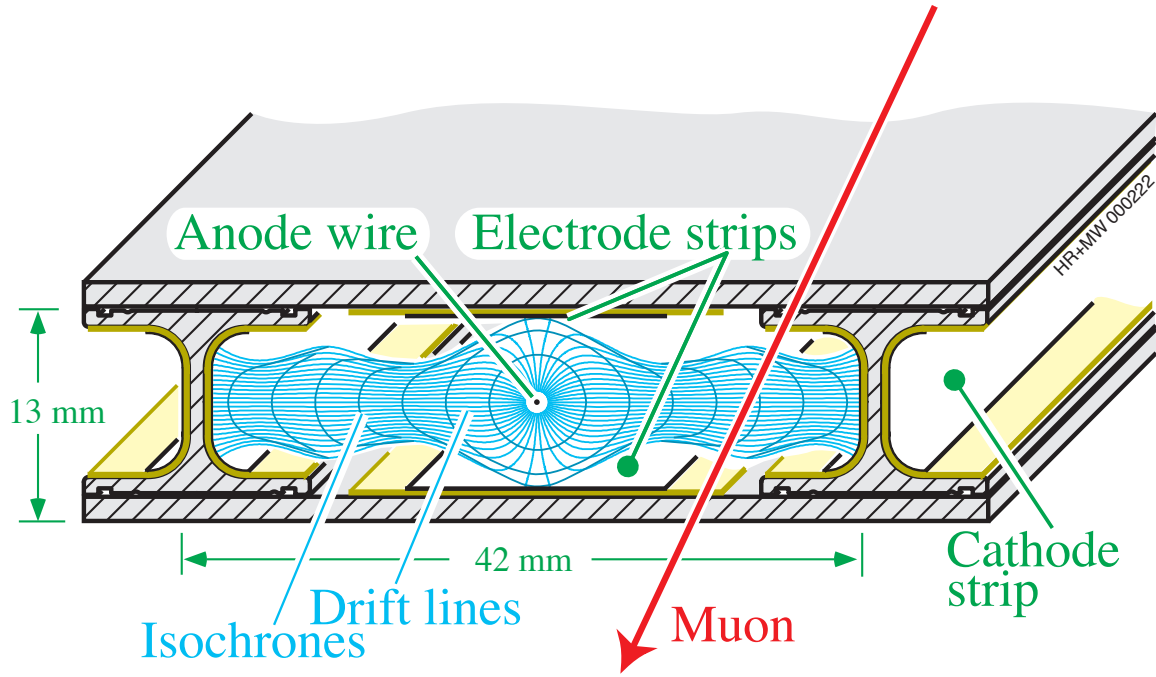


Figure 1.4.: A drift tube of the CMS muon system [5]

track from the wire. Drift tubes don't have to be cylindrical, as is shown in figure 1.4, which shows a drift tube of the muon system of the CMS⁴ detector at the LHC⁵.

1.2.2. Time projection chambers

Time projection chambers consist of a large gaseous volume in which one creates a homogeneous electric field (see figure 1.5). Ionisation tracks are transported to the anode, where a two dimensional detector records the position as well as the time of the signal. Since the electric field in the chamber is homogeneous, the drift velocity is also constant and one can easily reconstruct the full three-dimensional coordinates of a track.

If one also applies a magnetic field to the gas volume, one can use the track curvature to measure the particle's momentum. Together with the dE/dx information from the amount of ionisation, this can be used to identify the ionising particle.

One experiment that uses these capabilities is the ND280⁶ near detector of the long baseline neutrino experiment T2K⁷. Figure 1.6 shows the whole detector and one of the three TPCs. Together the TPCs account for a sensitive volume of $\sim 8.5\text{ m}^3$, which is read out with $\sim 124\,000$ channels. This provides a space point resolution of about 0.7 mm [7]. If one were to instrument the whole volume instead of just the anode sides (as would be necessary for a silicon pixel detector), one would need orders of magnitude more read-out channels.

⁴Compact Muon Solenoid

⁵Large Hadron Collider

⁶Near Detector 280 m

⁷Tokai To Kamioka

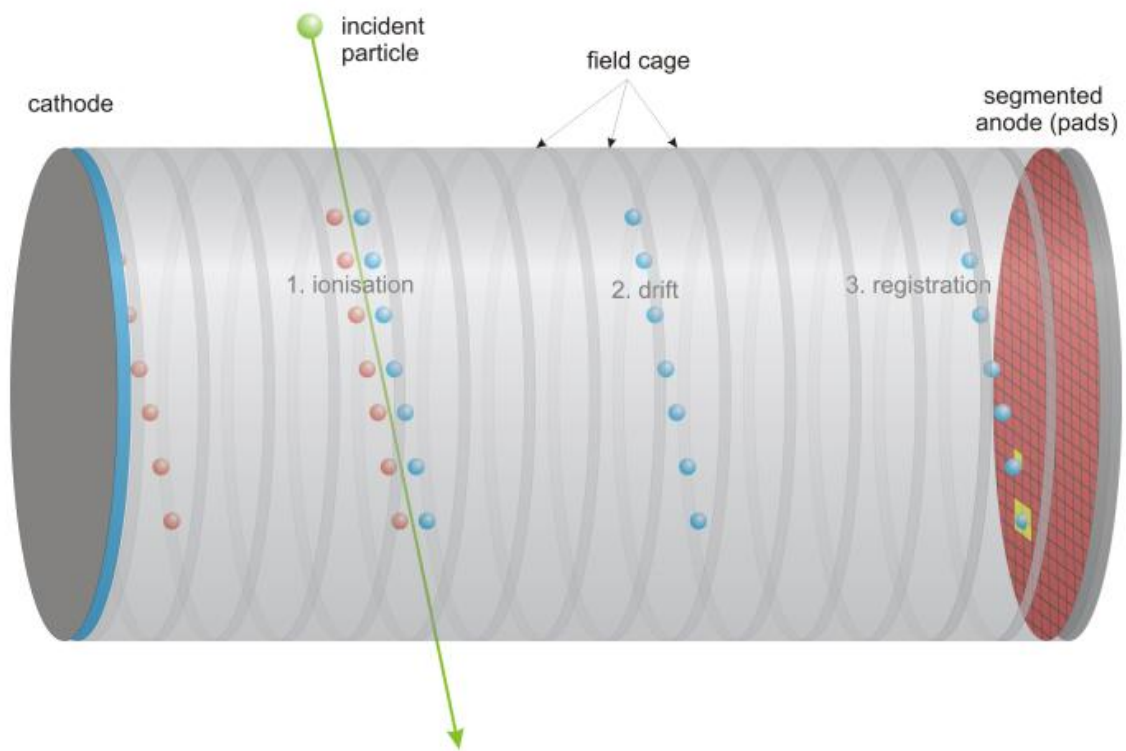
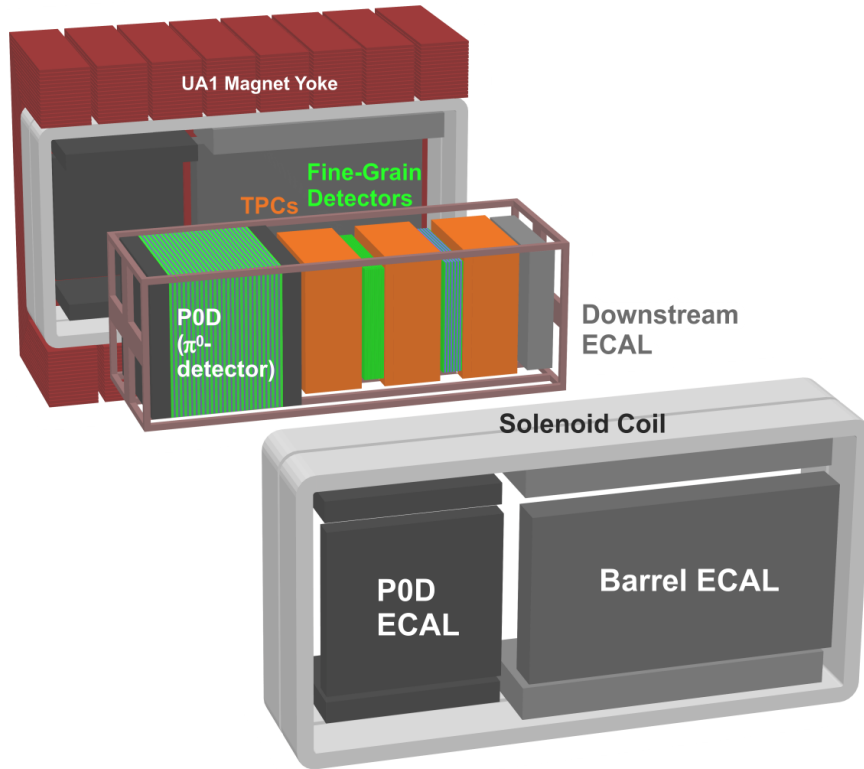


Figure 1.5.: Principle of operation of time projection chambers [6]



(a) Exploded view of the ND280 detector and position of the TPCs



(b) One of the TPCs during assembly

Figure 1.6.: The T2K/ND280 TPCs [8]

2. Setup

2.1. The drift chambers

We measure the electron drift velocity using T2K/ND280-type monitoring chambers [9, 10, 11]. They are specifically designed for the measurement of the electron drift velocity and feature a gas volume with a field cage of 14.8 cm length. One of the chambers can be seen in figure 2.1. For a v_d measurement, electrons of ~ 0.5 MeV are emitted into the chamber by a ^{90}Sr source. These electrons traverse the chamber and ionise the gas along their trajectory. At the other end of the chamber the electrons hit a scintillator and trigger the measurement. An electric field along the z -axis transports the ionisation electrons towards a MicroMeGaS¹ at the end of the chamber, where the signal is amplified and recorded so one can determine the drift time of the electrons.

MicroMeGaS consist of a printed circuit board (PCB) with anode pads and a fine wire mesh, suspended $\sim 100\text{ }\mu\text{m}$ above those pads (figure 2.2). If one applies a voltage of about 300 V – 500 V between mesh and pads, the electric field will be strong enough to achieve gas amplification of the electrons drifting into the structure.

There are two ^{90}Sr sources at different z -positions to minimise systematic errors due to effects of the amplification region. The drift time at both z -positions is measured and the drift velocity

$$v_d = \frac{\Delta z}{\Delta t} = \frac{z_1 - z_2}{t_1 - t_2}$$

is then calculated only from the drift path between the two ^{90}Sr positions. This way, systematic offsets on the time measurement (electronic delays, field inhomogeneities near the walls of the chamber, etc.) cancel out, since they are the same for both measurements.

The ND280 monitoring chambers have a Δz of 120.4 mm, which in combination with the used DAQ² setup allows v_d measurements between about $20\text{ }\mu\text{m}/\text{ns}$ and $100\text{ }\mu\text{m}/\text{ns}$. The chambers also feature a slot for the insertion of an ^{55}Fe gamma source for the measurement of the gain at the MicroMeGaS, but this is not used in this study.

2.2. DAQ

The basic DAQ setup can be seen in figure 2.3. It is built around an MVME3100 single board computer and a CAEN VX1720 Flash ADC³. The ADC uses a sampling rate of 250 MHz

¹Micro Mesh Gaseous Structure

²Data acquisition

³Analog to Digital Converter

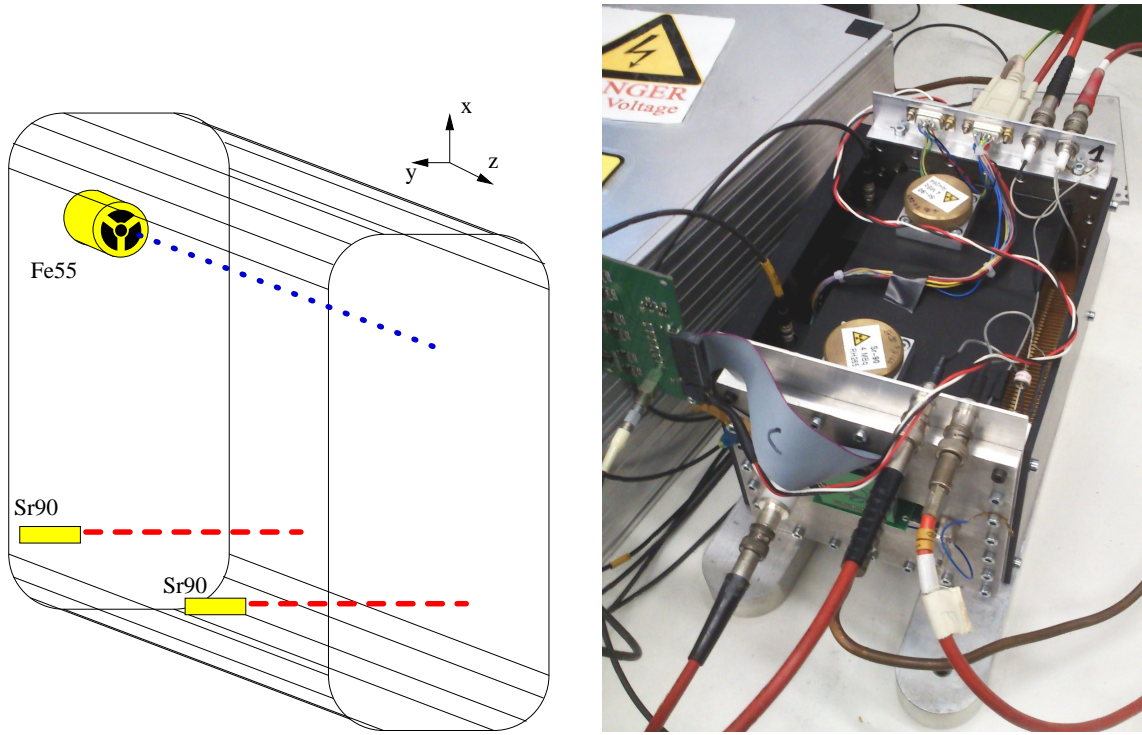


Figure 2.1.: Schematic view (left) [9] and picture (right) of one of the monitoring chambers. One can see the ^{90}Sr sources mounted on top of the chamber. An electric field is applied in the z -direction inside the chamber, perpendicular to the trajectory of the ionising electrons.

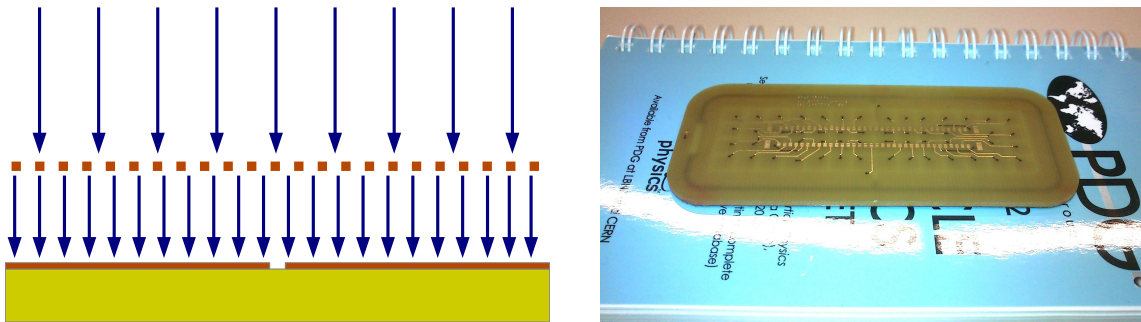


Figure 2.2.: Schematic view (left) and picture (right) of a MicroMeGaS as used in this study. The arrows symbolise the applied electric field. The picture shows the back side of the PCB with the connectors facing the camera. One can see the anode pads shining through the PCB.

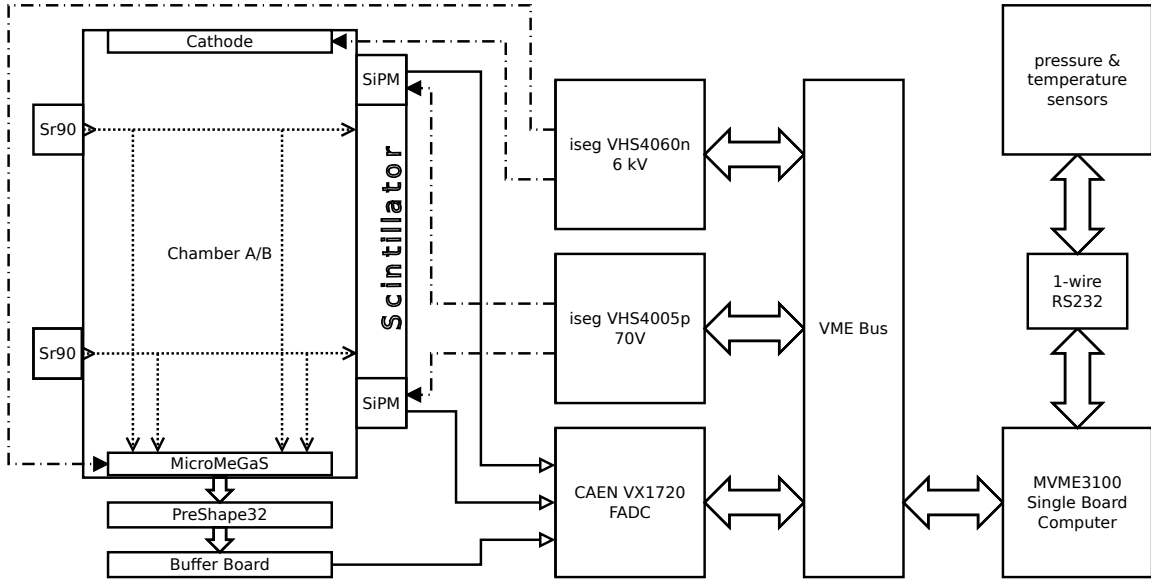


Figure 2.3.: DAQ setup

and is triggered by the coincidence of the signals of two SiPMs⁴ connected to a scintillating fibre. Using the coincidence signal of two SiPMs rather than just one, suppresses the noise always present at a single SiPM.

This setup cannot distinguish between the two z -positions. So to measure the drift velocity, a lot of time measurements are taken and the values are put into a histogram like the one shown in figure 2.4. The two different z -positions show themselves as two peaks in the t distribution. A fit to these peaks allows the determination of the mean values of t_1 and t_2 and thus Δt . About 2000 time measurements make up one v_d measurement. This takes about one minute, during which we can assume the temperature and the pressure of the drift gas to be stable.

Pressure and temperature are measured at multiple points in and around the chambers. All sensors are connected to a 1-wire network, as those measurements are not time critical. A programmable 6 kV power supply creates the drift and amplification fields. A second power supply feeds the SiPMs with about 70 V. A picture of the whole DAQ setup can be seen in figure 2.5.

2.3. Gas mixing

The gases analyzed in this work were mixed using the UGMA⁵ gas mixing station of III. Physikalisches Institut B at RWTH Aachen University. It was operated in partial pressure mode, which allows the mixing of up to two gas additives to one base gas, with volume fraction errors below 0.1 vol.-% [12].

⁴Silicon Photo Multiplier

⁵Universelle Gas-Misch-Anlage

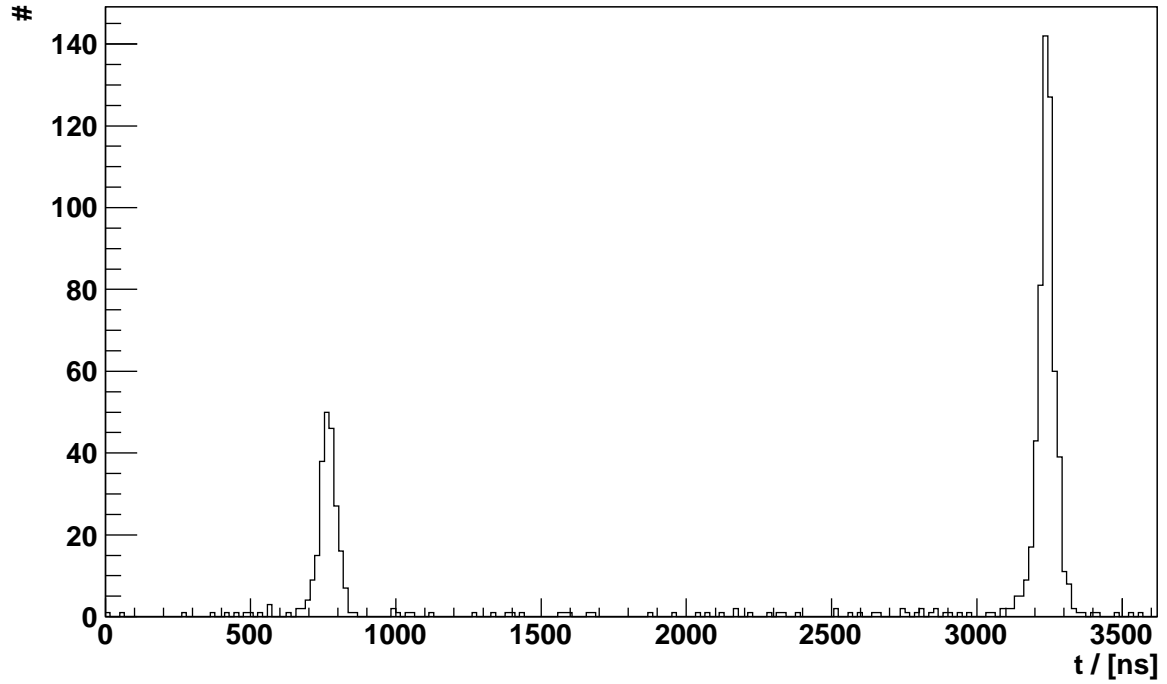


Figure 2.4.: Histogram of measured drift times. The two peaks correspond to the two z -positions of the tracks. The different peak heights can be explained by a difference of activity of the two ^{90}Sr sources or a slight misalignment of source, slits and scintillator for one of the sources.

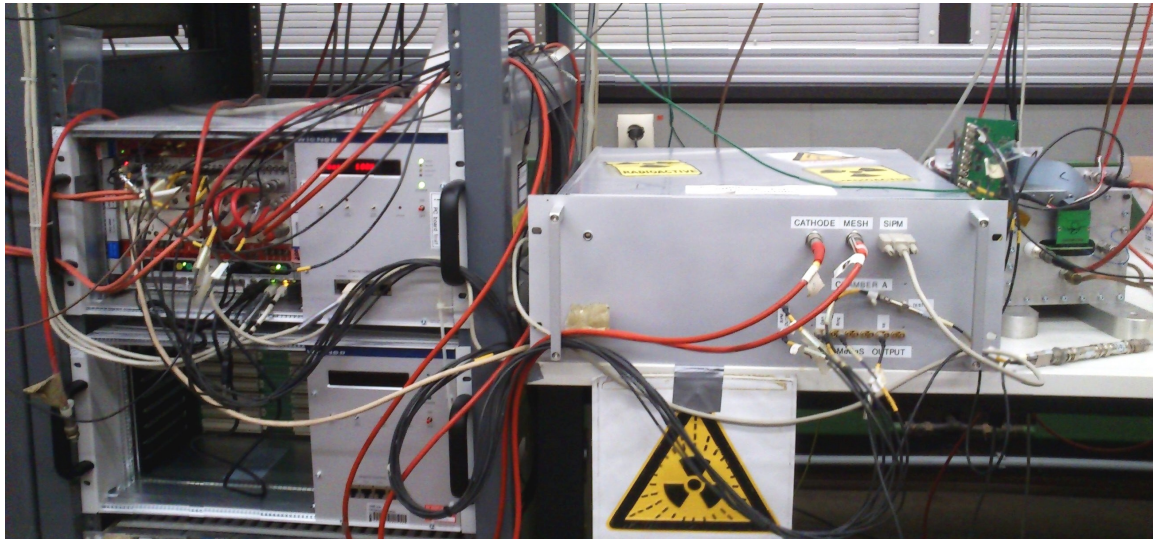


Figure 2.5.: Picture of the experimental setup

Gas mixtures are commonly quoted as volume fractions η_V , e.g. “Ar 95 % – CH₄ 5 %”. For ideal gases, these values unambiguously describe the mixtures since for ideal gas mixtures volume fractions, partial pressure fractions and mole fractions are equal at all temperatures and pressures:

$$\eta_V = \eta_p = \eta_n = \text{const}, \quad \forall T, p$$

For real gases this does not hold anymore. For a given mixture, e.g. in a pressure vessel, only the mole fraction stays constant over all temperatures and pressures, since we do not add or remove any molecules from the mix. The volume and pressure fraction of the constituents, on the other hand, become dependent of the temperature and pressure in the vessel:

$$\begin{aligned} \eta_n &= \text{const}, \quad \forall T, p \\ \eta_V &= \eta_V(T, p) \\ \eta_p &= \eta_p(T, p) \end{aligned}$$

This means that the given volume fraction of the mix is actually only valid for certain values of T and p . If one uses the gas mixture in other conditions, the mole fraction will stay the same, but the volume fractions will be different. In this work, we will quote gas mixtures as volume fractions at 1013.25 mbar and 0 °C, in accordance to DIN 1343 [13], which regulates the standard volumes used by gas distributors in Germany.

The UGMA is able to regulate both the gas flow and the pressure inside the drift chambers. We chose a supply flow of 5 l/h and a pressure of 1000 mbar. The flow ensures about five volume exchanges per hour and the slight overpressure is intended to keep the contamination with atmosphere to a minimum. This works very well and we achieve a water contamination of less than 5 ppm and oxygen levels below 1 ppm.

In cases where the atmospheric pressure surpasses 1000 mbar, the chambers are still operated at slight overpressure, since the gas flow creates a pressure gradient in the pipes leading from the chambers to the UGMA. This pressure drop is in the order of a few mbar and keeps the chamber pressure above the atmospheric pressure even if the pressure regulation in the UGMA is fully opened (as is the case when the nominal pressure is below atmospheric pressure). This is considered in the calculations, as the pressure measurements used for the v_d analysis happen directly at the chambers.

As a security feature, a maximum differential pressure of 20 mbar was established. When the ambient pressure falls below 980 mbar, the nominal chamber pressure is lowered accordingly to prevent damaging the chambers.

2.4. Simulation software

There exists no comprehensive analytical formula to predict the electron drift velocity in arbitrary gas mixtures. To get a theoretical prediction of the drift properties, we therefore use the numerical simulation program Magboltz⁶ embedded in the framework of Garfield++⁷.

⁶Version 9.0.1, <http://consult.cern.ch/writeup/magboltz/>

⁷Revision 309, <http://garfieldpp.web.cern.ch/garfieldpp/>

Garfield++ and Magboltz use mole fractions to describe the simulated gas mixtures. Since we use volume fractions to describe the gas mixtures, those have to be converted before the simulation. To do so, the molecular masses and densities at standard conditions (as given in appendix A) are used.

$$\eta_{n,i} = \frac{\eta_{V,i} \cdot \frac{\rho_{0,i}}{M_{mol,i}}}{\sum_j \eta_{V,j} \cdot \frac{\rho_{0,j}}{M_{mol,j}}}$$

The difference between mole and volume fractions is small for noble gases and small molecules, but can become important for large-molecule carbon hydrates. As an example, the molar fractions of Ar 93 % – CH₄ 5 % – CO₂ 2 % are

$$\begin{aligned}\eta_{n,\text{Ar}} &= 92.98 \%, \\ \eta_{n,\text{CH}_4} &= 5.01 \%, \\ \eta_{n,\text{CO}_2} &= 2.01 \%,\end{aligned}$$

while the fractions of Ar 95 % – CF₄ 3 % – iC₄H₁₀ 2 % are

$$\begin{aligned}\eta_{n,\text{Ar}} &= 94.92 \%, \\ \eta_{n,\text{CF}_4} &= 3.01 \%, \\ \eta_{n,\text{iC}_4\text{H}_{10}} &= 2.07 \%\end{aligned}$$

and show a much larger deviation from the volume fractions due to the isobutane admixture.

Magboltz can simulate the drift velocity and the three-dimensional diffusion along the track as well as the Townsend coefficient (excluding the Penning and Jesse effects) for arbitrary *E*- and *B*-fields. It is written in Fortran, but Garfield++ provides an easy to use C++ API. This API was used to build a program, called Magsim, that runs on our Condor⁸ computing cluster. It allows the automated and fast simulation of gas mixtures with up to 5 gas additives.

During the simulations we noticed that Magboltz overestimates the statistical errors on its data points. This has been fixed in the newest versions of Magboltz, which could not yet be included into Garfield++ and Magsim. But since this bug has no influence on the position of the data points themselves, it is irrelevant for the plots presented in this work.

2.5. Calibration and systematic errors

The drift velocity $v_d = \Delta z / \Delta t$ does not only depend on *E*, but also on the gas density *n* and thus the pressure *p* and the temperature *T*. Therefore, a handle on the systematic errors of all these variables is needed.

⁸<http://research.cs.wisc.edu/htcondor/>

2.5.1. Drift length

The drift length Δz is the distance between the two ^{90}Sr electron tracks. The position of these tracks is given by slits in the casing of the chambers and the z -distance between those slits (centre to centre) is nominally 120.4 mm. The main uncertainty of the drift length stems from the width of the slits, which is 1.2 mm.

$$\frac{\sigma_{\Delta z}}{\Delta z} = \frac{2 \cdot 0.6 \text{ mm} / \sqrt{12}}{120.4 \text{ mm}} \lesssim 3 \text{ ‰}$$

2.5.2. Timing

The drift time Δt is the difference between the drift time measurements of the two ^{90}Sr electron tracks. To check the accuracy of those time measurements, a digital signal generator was connected to the inputs of the Flash ADC. The DAQ setup was then fed with pulses of defined intervals and the output of the setup was compared with the settings of the signal generator. This way the whole hardware and software chain that produces our final time measurement could be tested.

$$\frac{\sigma_{\Delta t}}{\Delta t} \lesssim 2 \text{ ‰}$$

2.5.3. Electric field

The electric field is created by a voltage U_f which is applied over an electric field cage of length l_f . The electric field and its error are thus:

$$E = \frac{U_f}{l_f}$$

$$\frac{\sigma_E}{E} = \sqrt{\left(\frac{\sigma_{U_f}}{U_f}\right)^2 + \left(\frac{\sigma_{l_f}}{l_f}\right)^2}$$

Since the actual field cage dimensions cannot be measured in its assembled state, the distance between the centres of the first and the last field strip of an unassembled field cage were measured (figure 2.6).

$$l_f = (148.0 \pm 0.5) \text{ mm}$$

$$\frac{\sigma_{l_f}}{l_f} \lesssim 3 \text{ ‰}$$

The accuracy of the voltage measurements was estimated by measuring the applied voltages with a Keithley source meter and comparing these values to the setpoints and measurements of the programmable power supply. The values were found to be in very good agreement with each other.

$$\frac{\sigma_{U_f}}{U_f} \lesssim 0.5 \text{ ‰}$$

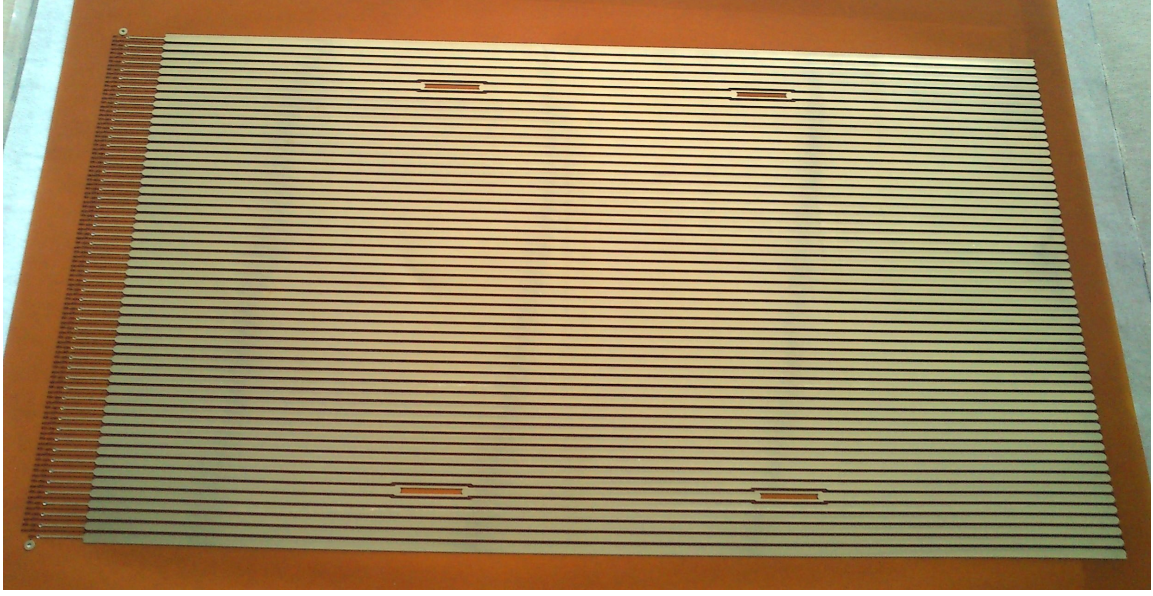


Figure 2.6.: Field strips of unassembled field cage

2.5.4. Temperature

The temperature logging uses DS18S20 digital temperature sensors in the gas flow right before and after the drift chambers, as well as outside the chambers for ambient measurements. These sensors have a guaranteed precision of 0.5 K [14]. To verify this, one of the sensors was frozen in water and the temperature curve during the melting process recorded. Due to latent heat, one expects a plateau at 0°C. Figure 2.7 shows such a plateau at around -0.2°C , which is well within the specified limits. Since all our measurements are done at room temperature, a temperature of 25°C or 298 K can be used for a simple estimate of the relative error of the temperature measurements.

$$\frac{\sigma_T}{T} = \frac{0.5 \text{ K}}{298 \text{ K}} \lesssim 2 \text{ ‰}$$

2.5.5. Pressure

The pressure in the chambers is measured with pressure transmitters manufactured by WIKA, which are read out by DS2450 ADCs. These sensors show a linear relation between pressure and signal. For the calibration of the sensors, they were put on atmospheric pressure and their signals were compared with the measurements of a calibrated Baratron manometer next door in the same building. This was done at two different days with ambient pressures of 1006.5 mbar and 975.55 mbar respectively. From these two data points a linear calibration for the pressure sensors was calculated. The pressure distribution at the calibration points after the calibration can be seen in figure 2.8.

Due to missing codes in the used ADCs, the pressure sensors show jumps in their signals at 1022 mbar and 1016 mbar respectively (figure 2.9). One can compensate for this behaviour

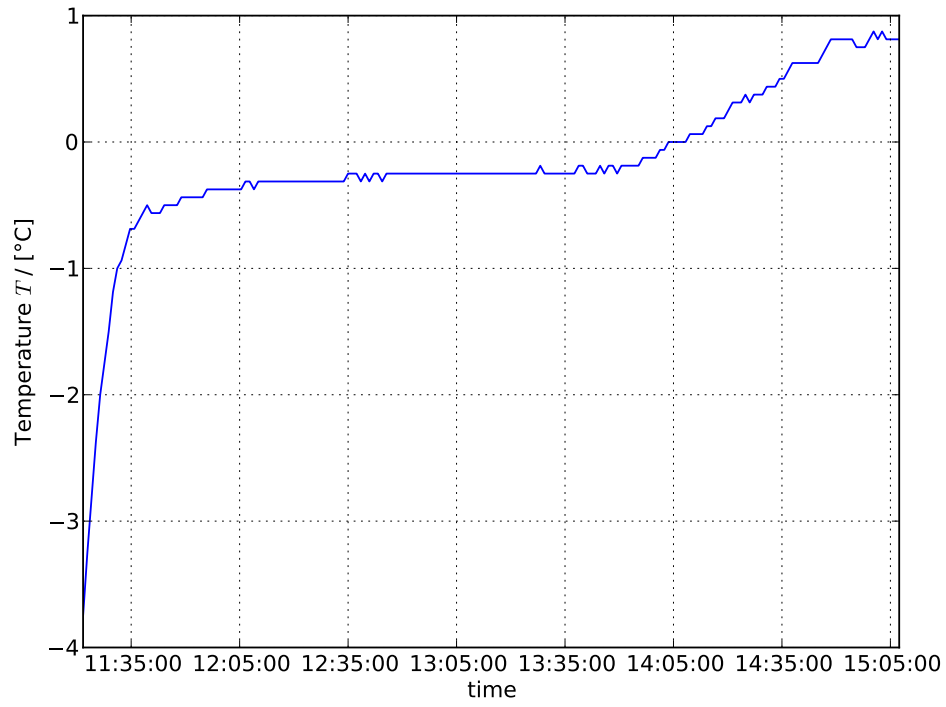


Figure 2.7.: Temperature curve of a DS18S20 temperature sensor in melting ice

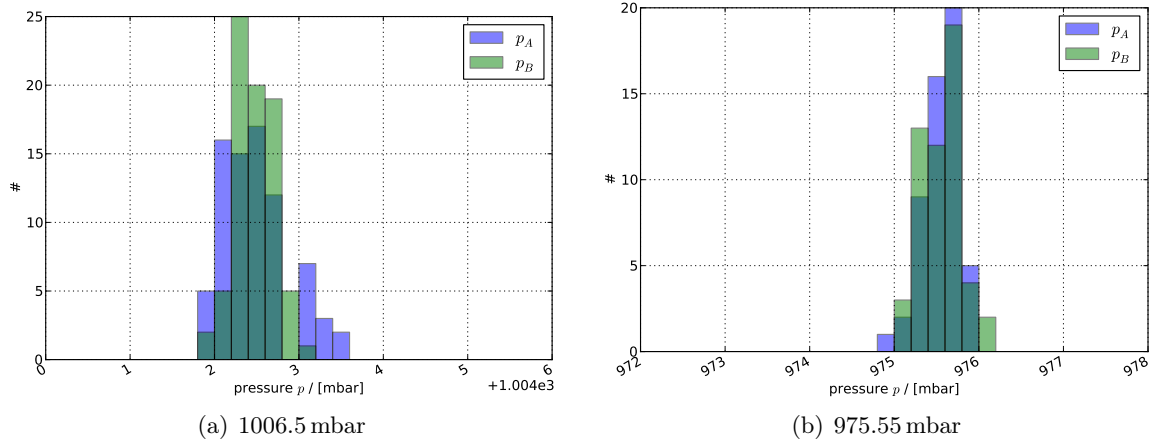


Figure 2.8.: Pressure distribution at calibration points

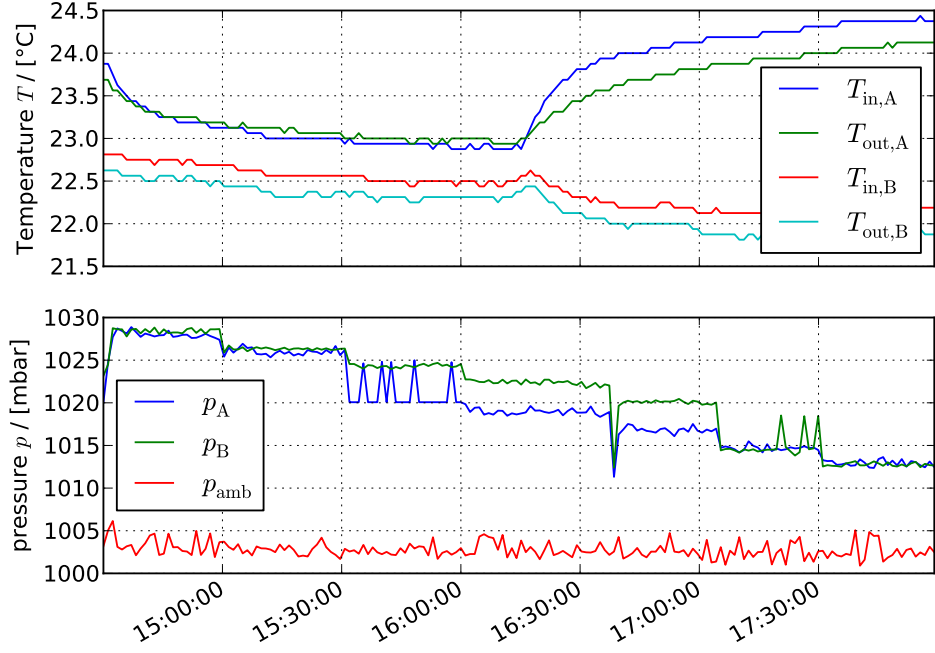


Figure 2.9.: Jump in pressure signals due to missing codes in the ADCs. The Temperatures were measured at the in- and outlets of the two chambers.

by shifting all pressure values above the jumps (as the calibration happened below) down. Since these jumps occur at different pressures for the two sensors, the proper values for the offsets can be deduced by employing cross correlation between the signals. Figure 2.10 shows the correlation between the signals for different offsets. We chose an offset of -2.8 mbar for sensor A and -3.4 mbar for sensor B. Figure 2.11 shows the histograms of the measurements in figure 2.9 before and after the ADC correction. The discontinuity has been reduced considerably, but it is still visible. For most measurements presented in this work, this is not a problem though, since the pressure in the chambers is regulated and set to a value below the pressure where the discontinuity appears.

Altogether the systematics of the pressure measurements are expected to be not larger than 1 mbar. The nominal pressure in the chambers is set to 1000 mbar, so the estimated relative error is

$$\frac{\sigma_p}{p} \lesssim \frac{1 \text{ mbar}}{1000 \text{ mbar}} = 1 \text{ ‰}$$

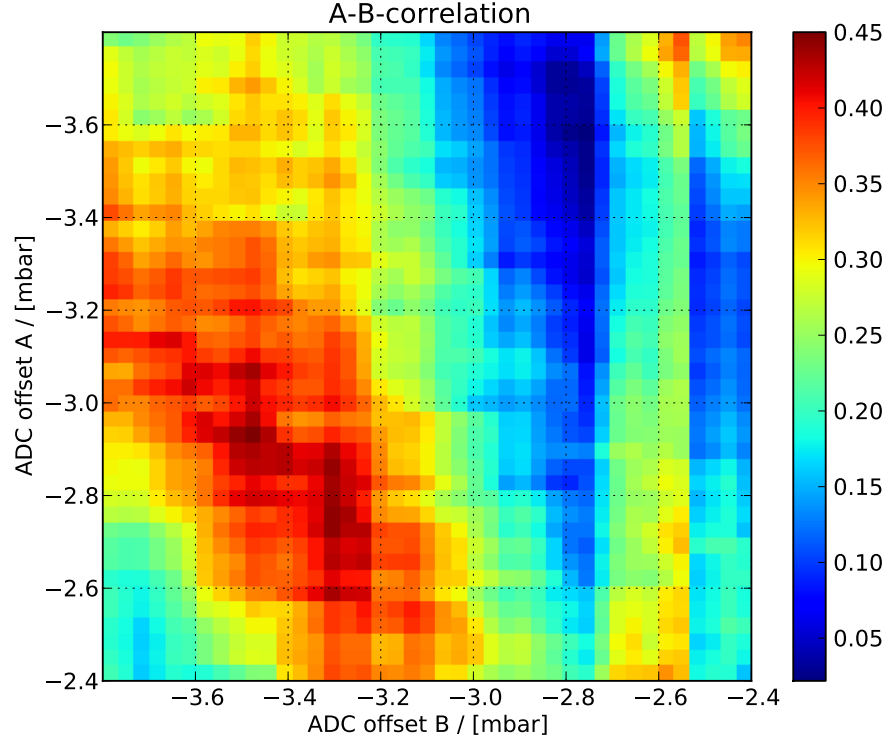


Figure 2.10.: Correlation between pressure signals for different offset corrections

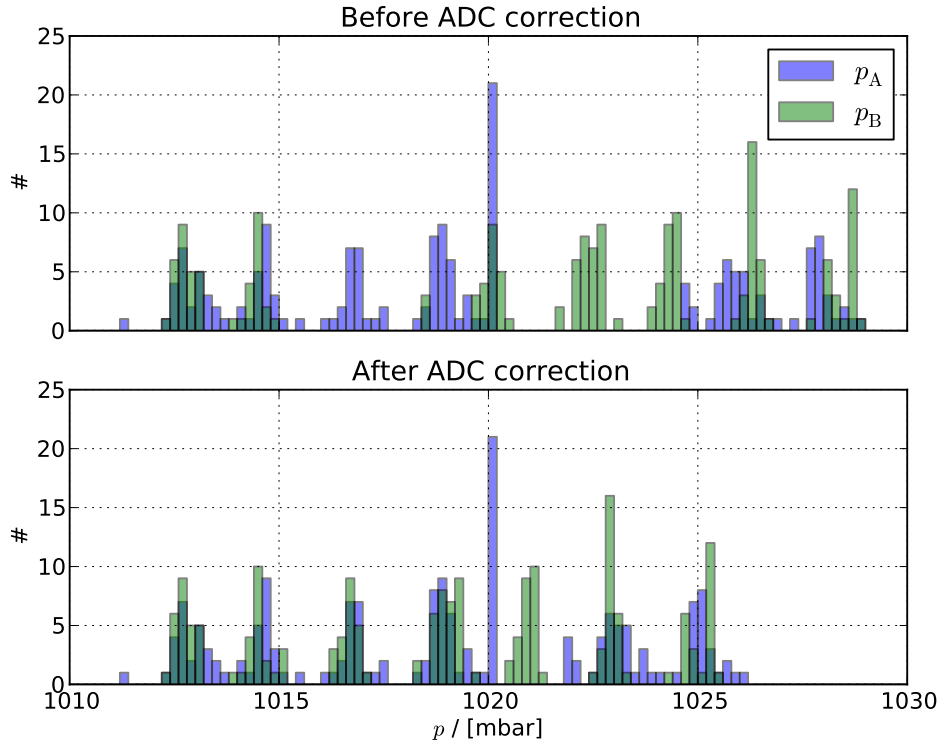


Figure 2.11.: Histogram of pressures before and after ADC correction

2.6. Putting it all together

Combining the errors of all the variables yields the systematic uncertainties

$$\left(\frac{\sigma_{v_d}}{v_d}\right)_{sys} = \sqrt{\left(\frac{\sigma_{\Delta z}}{\Delta z}\right)^2 + \left(\frac{\sigma_{\Delta t}}{\Delta t}\right)^2} \lesssim 4\text{‰},$$

and

$$\left(\frac{\sigma_{E^{T/p}}}{E^{T/p}}\right)_{sys} = \sqrt{\left(\frac{\sigma_{U_f}}{U_f}\right)^2 + \left(\frac{\sigma_{l_f}}{l_f}\right)^2 + \left(\frac{\sigma_T}{T}\right)^2 + \left(\frac{\sigma_p}{p}\right)^2} \lesssim 4\text{‰}.$$

These errors proved to be reasonable as we used two chambers to cross check for chamber specific systematics. No differences outside the expected errors were found.

3. Results

The drift velocity of electrons in a gas mixture depends not only on the electric field strength E , but also on the gas molecule density n . So if one wanted to characterise a gas mixture in its entirety, one would have to do so at a wide range of environments. Conversely, if one wants to measure the drift velocity at a certain E -field, one would have to regulate the temperature and pressure of the gas precisely, which can be hard to achieve.

Fortunately the dependence on E and n only appears in the form of E/n . So instead of interpreting v_d as a function of E with additional parameters T and p , it can be seen as a function of E/n , or as a function of $E^{T/p}$ if we assume an ideal gas. Since we have no direct way to measure n , we use $E^{T/p}$ as argument for the drift velocity functions:

$$v_d = v_d(E^{T/p})$$

All data presented in this work can also be accessed via the gasDB at <http://web.physik.rwth-aachen.de/gasDB/>. Every v_d data point actually consists of multiple measurements at the same electric field that have been combined into one mean point $\overline{v_d}$ and the statistical error $\sigma_{v_d,stat}$ is just the error of that mean. The same is of course true for $E^{T/p}$.

An example of a set of measured drift velocities at different electric fields can be seen in figure 3.1. Each cluster of points is reduced to one single data point in figure 3.2. Clusters with an $\text{RMS}(v_d)$ of $2 \mu\text{m}/\text{ns}$ and above are ignored, as such high RMS values are usually the result of a v_d above or below the accessible v_d range of the experimental setup (though this was not necessary in this example). Also, all points outside a $3 \cdot \text{RMS}(v_d)$ range of the cluster are removed and the mean and RMS are recalculated. This automatically removes implausible outliers and is only done once per cluster. For most data points this has little to no effect on the final mean and RMS value.

From now on, unless explicitly stated otherwise, $\overline{v_d}$ will be written simply as v_d and $\overline{E^{T/p}}$ as $E^{T/p}$. All v_d plots in this work include the statistical error on v_d as well as $E^{T/p}$, but since they are in the order of $0.01 \mu\text{m}/\text{ns}$ and $0.01 \text{ V}/\text{cm K}/\text{mbar}$ respectively, they often cannot be seen clearly. In general, the statistical errors are in the order of 1 % or better.

3.1. Ar-CH₄-CO₂ mixtures

Ar-CH₄ mixtures are classical drift gases that have been used, and continue to be used, in many gas based detectors. They are often named PX, where X is the percentage of CH₄ in the mix, e.g. P5 for Ar 95 % – CH₄ 5 % or P20 for Ar 80 % – CH₄ 20 %.

Figure 3.3 shows our measurements for P5, P10, P15, P20 and P25. They all show similar deviations from the simulated drift velocities. These deviations cannot be attributed to

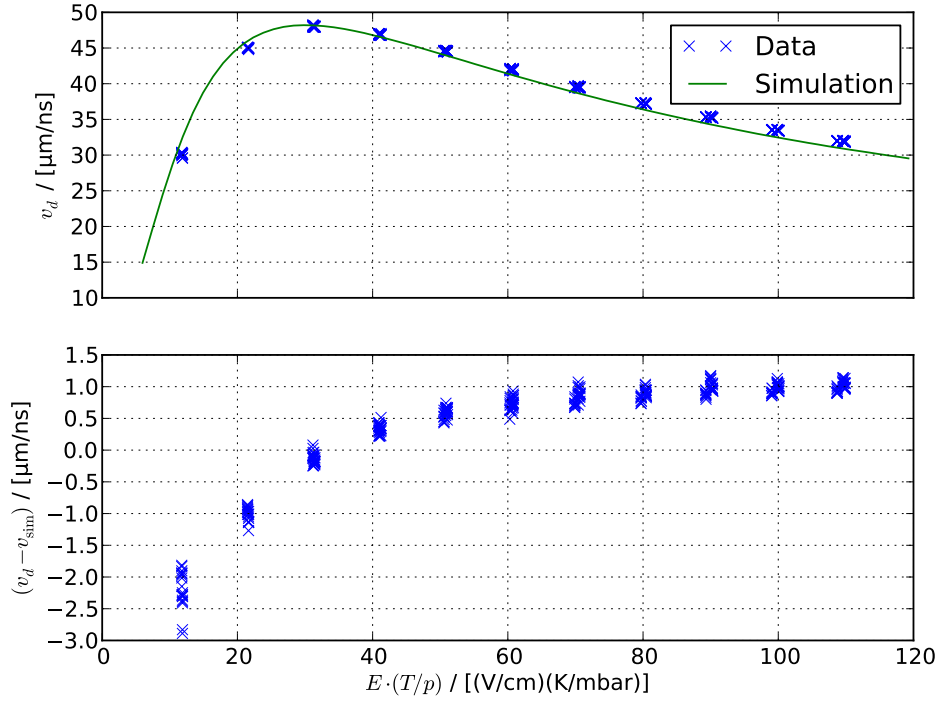


Figure 3.1.: Example of raw v_d measurements with Ar 93 % – CH₄ 7 %

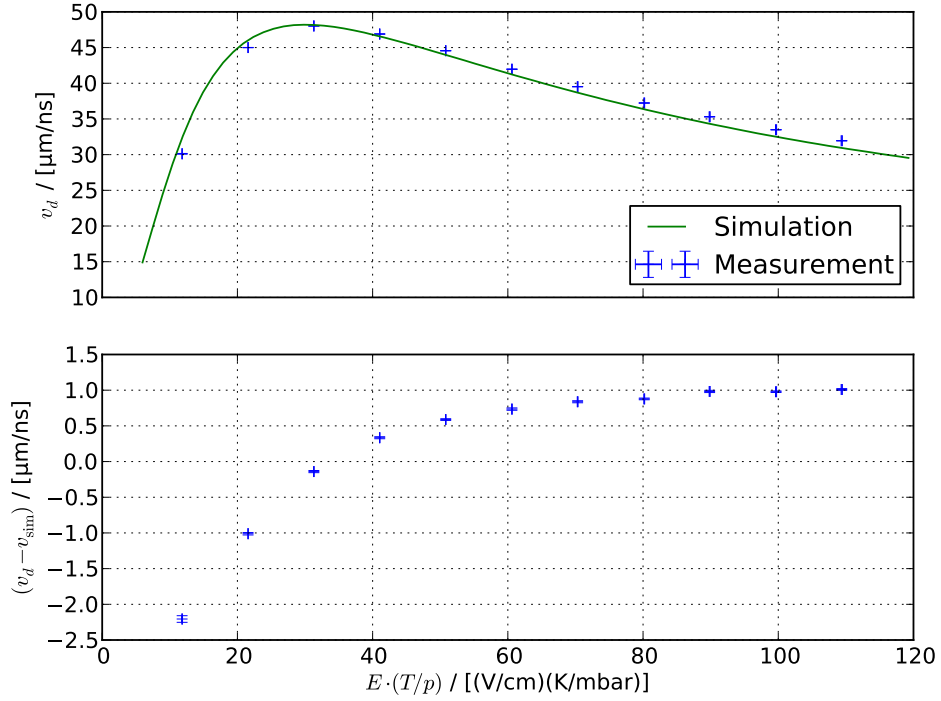


Figure 3.2.: Example “condensed” v_d measurements with Ar 93 % – CH₄ 7 %. Please note that the statistical errors are too small to be seen for most points in this plot.

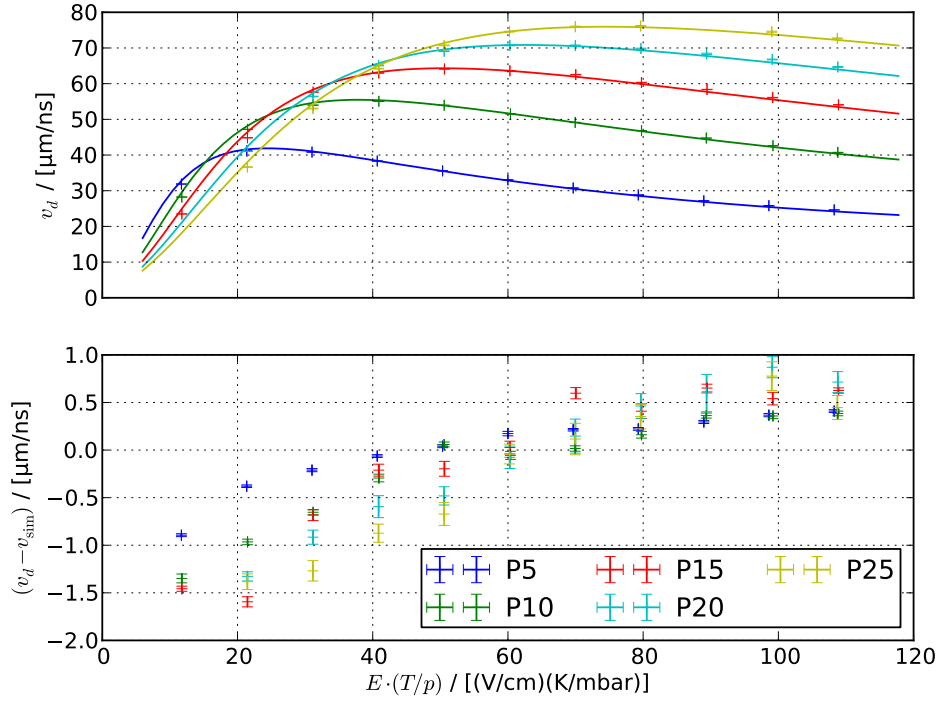


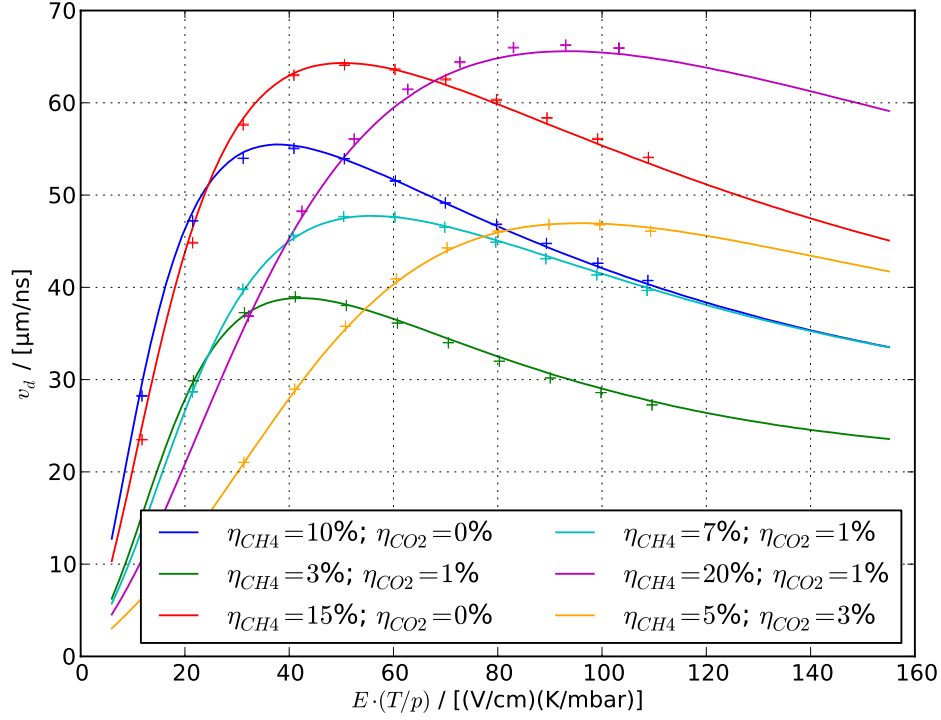
Figure 3.3.: v_d measurements and simulations of P5, P10, P15, P20 and P25

gas mixing errors alone. Varying the CH₄ fraction for the simulation does not affect the drift velocities at low electric fields as much as it does at high electric fields. And it is not possible to tweak the simulated gas fraction in a way as to create a perfect fit to the data. The deviations are therefore either an inaccuracy in the Magboltz simulations, effects of impurities of the mixed raw gases or not understood systematics in our experimental setup, or a combination of all three.

Drawing multiple v_d curves into one plot is feasible as long as one only varies one gas fraction. Adding a third gas (in this case CO₂) and varying its fraction as well would render such a plot cluttered and unreadable. We therefore chose a different approach to visualise the impact of the different additives. Most v_d curves show the same behaviour: The drift velocity increases with an increasing $E T/p$ until it reaches a maximum. It then falls off again, and the curvature around the maximum is higher if the maximum appears at low $E T/p$ values (see figure 3.4).

Knowing the position of the maximum thus already gives a rather good impression of the features of the curve. Furthermore, ideally one would like to operate a detector at the maximum of the curve since there the dependence of $E T/p$ is minimal and fluctuations in temperature, pressure and electric field have the smallest effect on the drift velocity and thus on the reconstruction of the original particle track. Since every v_d curve is reduced to this single working point, the effects of two gas additives can be comfortably visualised in a 2D plot.

Both the measured and simulated working points are determined by fitting a function to the simulated or measured data points and calculating the position of the maximum from the

Figure 3.4.: v_d curve shape examples

best fit parameters.

$$f_{\text{fit}}(E T/p) = (a + b \cdot E T/p) \exp(-d \cdot E T/p) + c$$

$$E T/p|_{\text{WP}} = \frac{ad - b}{-bd}$$

$$v_d|_{\text{WP}} = f_{\text{fit}}(E T/p|_{\text{WP}})$$

Figure 3.5 shows an example of such a fit. Although there is no theoretical motivation for the chosen function, it fits the data around the v_d maxima very well. This holds true even for extremely wide maxima, as will be shown in section 3.3.

Due to limitations of the experimental setup, we can only measure $E T/p$ values up to about 110 V/cm K/mbar and determine working points up to 100 V/cm K/mbar. The position of the simulated working points is only limited by the chosen simulated electric field range.

The effect of varying CH_4 and CO_2 fractions on the position of the working point is shown in figure 3.6. The intersections of the solid lines were determined from simulated data, while the coloured marks show measured data. Points with the same marker shape have the same CH_4 fraction, while same colour indicates a shared CO_2 fraction. Additionally to the position of the maximum, the horizontal lines show the width of the peak, defined as the $E T/p$ range where

$$\frac{\Delta v_d}{v_d|_{\text{WP}}} = \frac{v_d|_{\text{WP}} - v_d}{v_d|_{\text{WP}}} < 1\%.$$

One can also plot the values of $v_d|_{\text{WP}}$ and $E T/p|_{\text{WP}}$ directly in dependence of the gas fractions as seen in figure 3.7. These contour plots were created with exactly the same data as

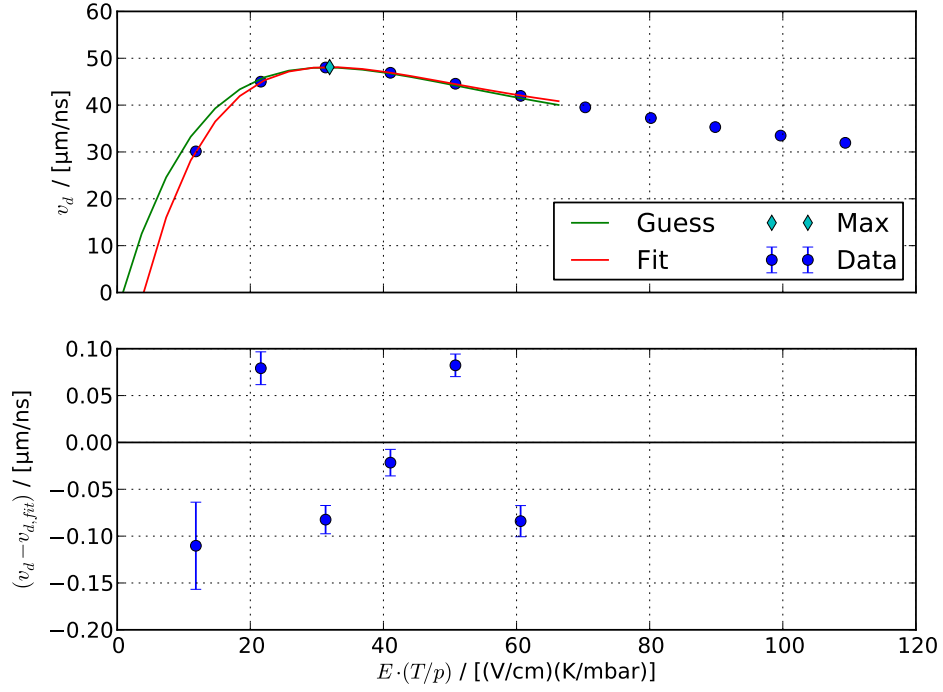


Figure 3.5.: Example working point fit for Ar 93 % – CH₄ 7 %. The curve labeled as “guess” shows the seed parameters for the fit algorithm.

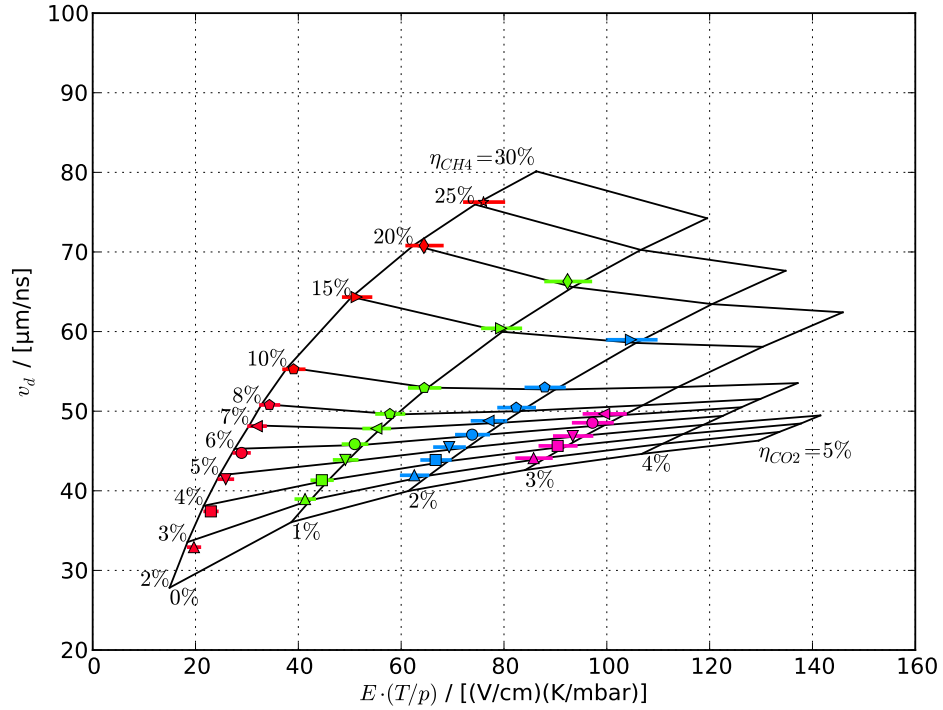


Figure 3.6.: Working points for Ar-CH₄-CO₂ mixtures. The horizontal lines mark the $E \cdot T/p$ range where $\Delta v_d / v_d|_{\text{WP}} < 1 \text{‰}$.

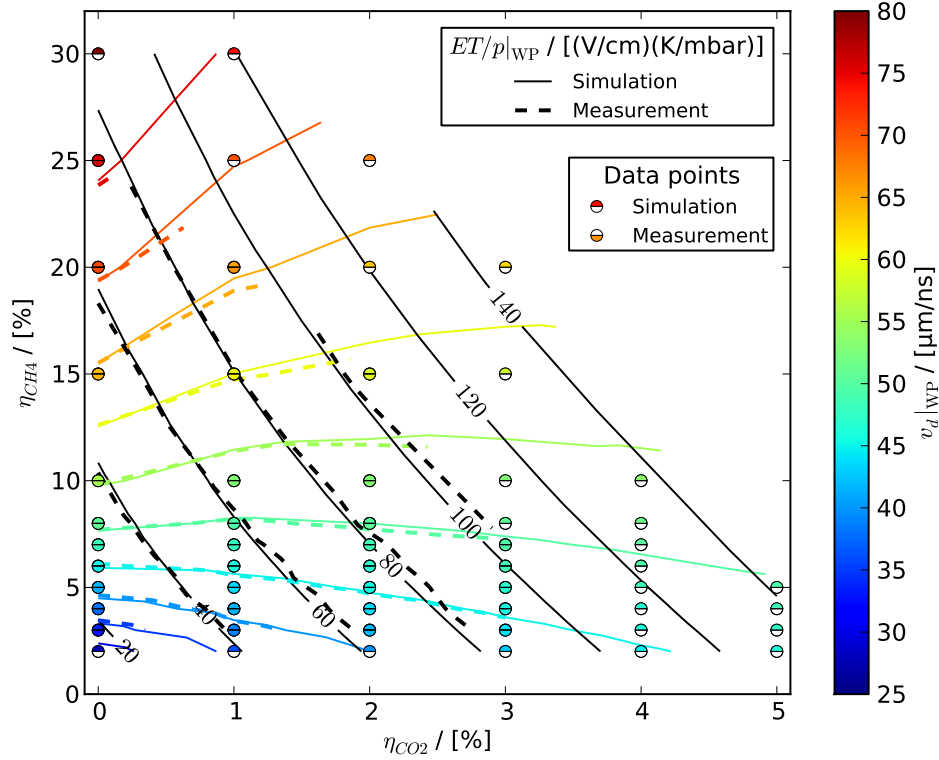


Figure 3.7.: Working points for Ar-CH₄-CO₂ mixtures in dependence of η

the spider web plot in figure 3.6 and the space in-between the data points is interpolated. The solid lines are interpolated from the simulated data and the dashed lines show the interpolation of the measured data. The black lines show mixtures with a constant $E^T/p|_{WP}$ and the coloured lines represent a constant $v_d|_{WP}$. The colours of the data points also indicate the $v_d|_{WP}$ value of those mixtures.

3.2. Ar-CF₄-iC₄H₁₀ mixtures

Ar 95 % – CF₄ 3 % – iC₄H₁₀ 2 % is also known as T2K-gas since it is being used in the ND280 near detector of the T2K neutrino experiment. Its v_d curve can be seen in figure 3.8. Ar-CF₄-iC₄H₁₀ mixtures' v_d curves have a shape that is very similar to those of Ar-CH₄-CO₂ mixtures. One can therefore use the same visualization technique to show the effects of varying volume fractions of the additives.

This is shown in figures 3.9 and 3.10. CF₄ and CH₄ have a very similar influence on the working point position, but one needs far less CF₄ to achieve the same effect as with CH₄. It is the other way around for iC₄H₁₀ and CO₂: iC₄H₁₀ has a similar, but smaller influence on the drift velocity compared to CO₂.

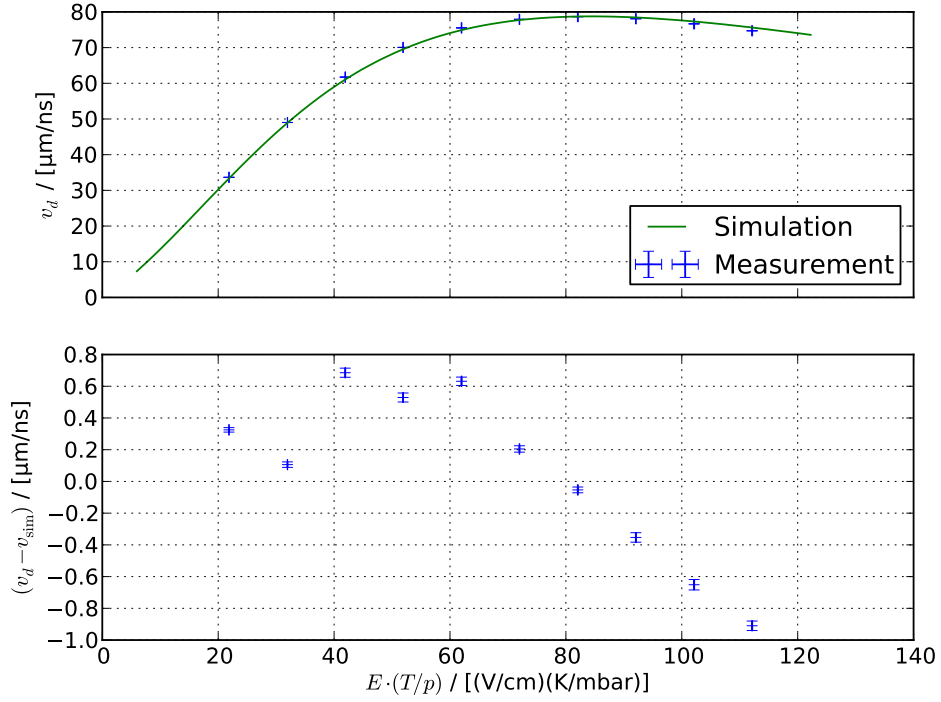


Figure 3.8.: v_d curve of Ar 95 % – CF₄ 3 % – iC₄H₁₀ 2 %, also known as T2K-gas

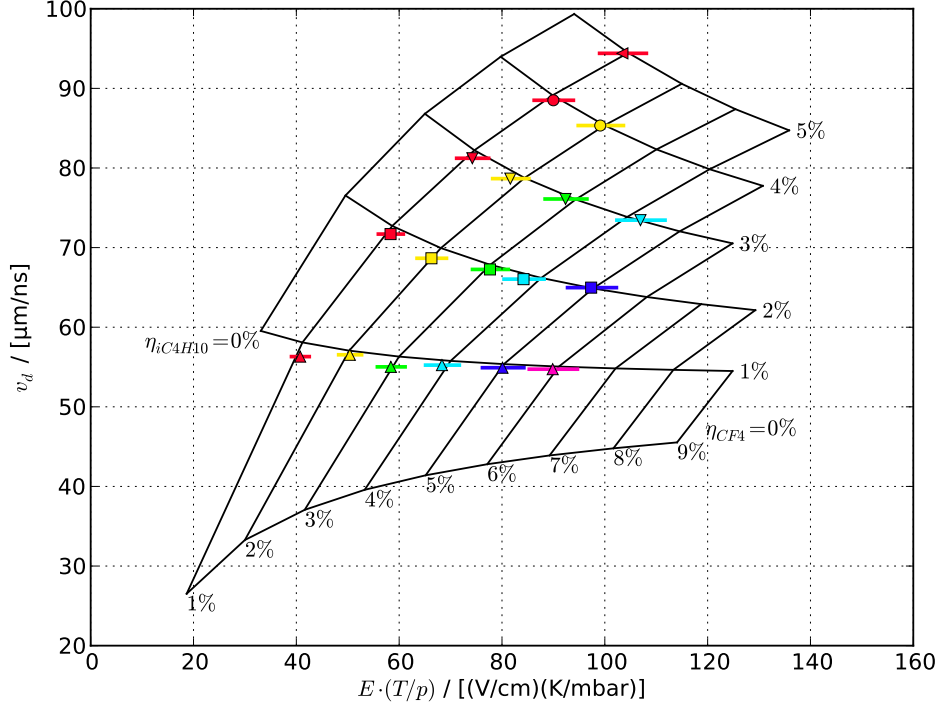


Figure 3.9.: Working points for Ar-CF₄-iC₄H₁₀ mixtures. The horizontal lines mark the $E \cdot T/p$ range where $\Delta v_d / v_d|_{WP} < 1 \%$.

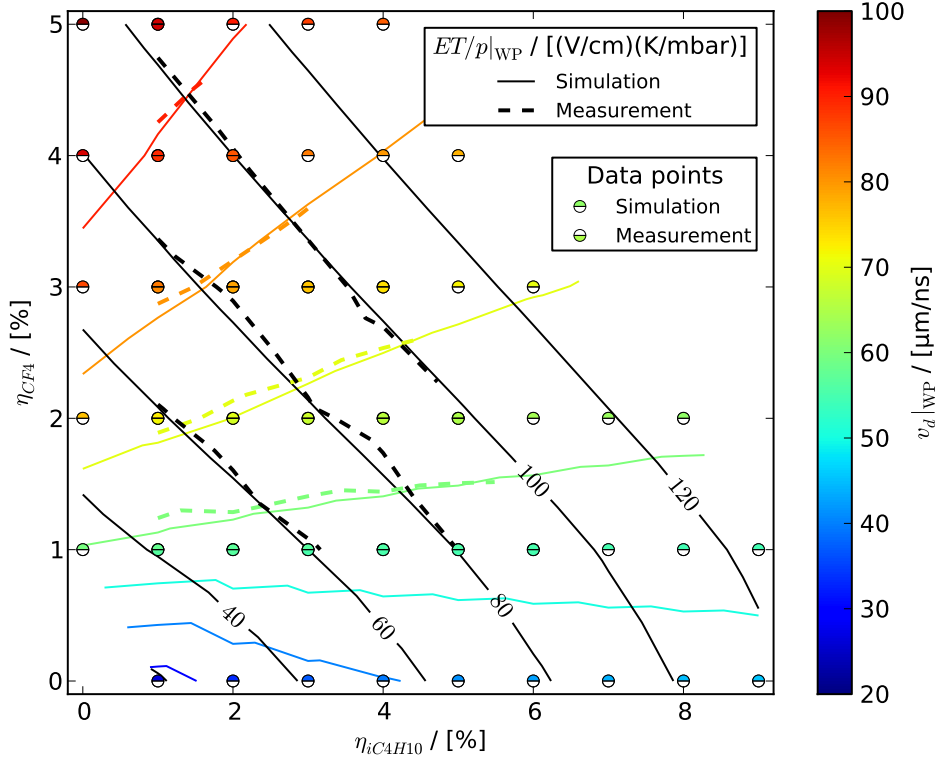


Figure 3.10.: Working points for Ar- CF_4 - iC_4H_{10} mixtures in dependence of η

3.3. Ar- CH_4 - H_2 mixtures

The influence of H_2 is quite different from CO_2 and iC_4H_{10} . All three pull the working point to higher ET/p values. But while CO_2 and iC_4H_{10} pull it towards v_d values of about $50 \mu\text{m/ns}$, H_2 always pulls it down (see figures 3.11 and 3.12). Mixtures with H_2 are thus comparatively slow drift gases. Another difference is the width of the working points: Adding H_2 to the mixture increases the width much more than the other additives.

The measured $ET/p|_{\text{WP}}$ values of mixtures with $\eta_{\text{H}_2} > \eta_{\text{CH}_4}$ do not match the simulated values very well. This is due to the fact that the v_d curves of those mixtures are very flat, which makes the ET/p position of the maximum very sensitive to changes in the gas composition as well as statistical fluctuations of the measurements. Despite this, the chosen fit function fits the data points even at very wide maxima, as shown in figure 3.13.

For high H_2 fractions ($\eta_{\text{H}_2} \gtrsim \eta_{\text{CH}_4}$) the v_d curves show an interesting behaviour: Instead of reaching a maximum and then falling off again, they approach a point of minimal slope and keep rising with higher ET/p values (figure 3.14). In mixtures with tuned CH_4 and H_2 fractions the v_d curves show a wide plateau (figure 3.15), which, for some mixtures, simulations show to be (more or less) stable up to ET/p values of 1400 V/cm K/mbar (figure 3.16). This makes these mixtures interesting for applications with very inhomogeneous fields. Unfortunately, at the moment we cannot measure the drift velocities at such high fields due to limitations in our experimental setup.

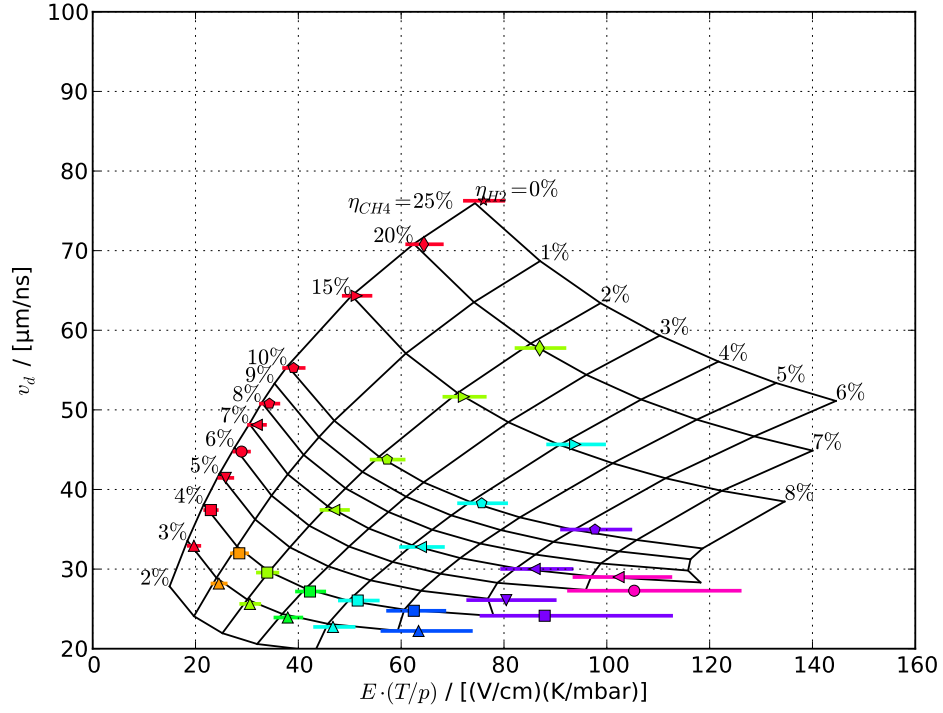


Figure 3.11.: Working points for Ar-CH₄-H₂ mixtures. The horizontal lines mark the $E T/p$ range where $\Delta v_d/v_d|_{WP} < 1\%$.

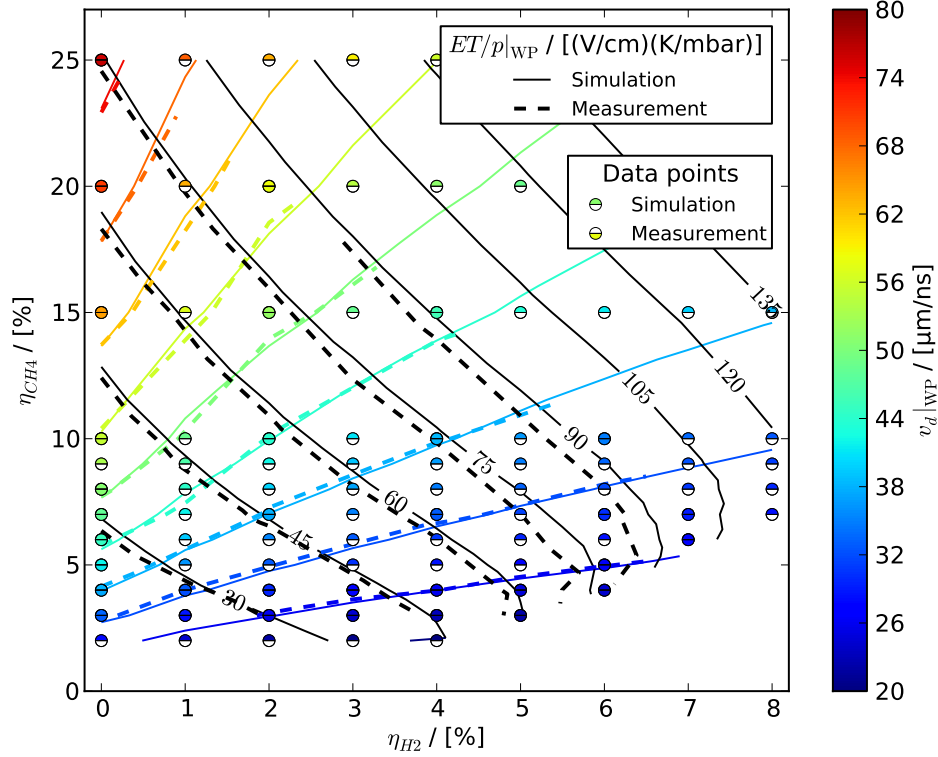


Figure 3.12.: Working points for Ar-CH₄-H₂ mixtures in dependence of η

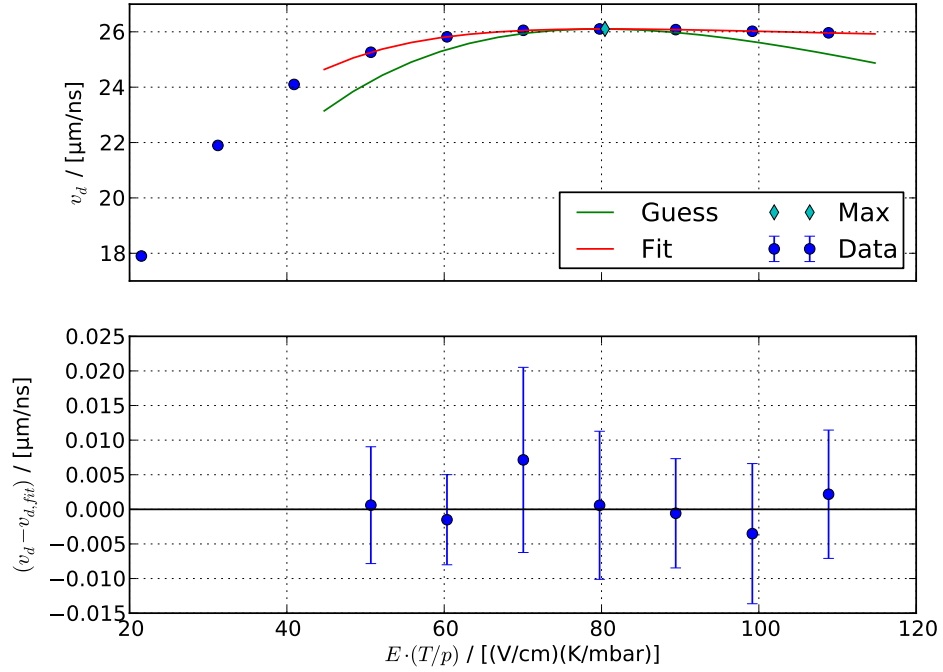


Figure 3.13.: Fit to very wide maximum of Ar 89 % – CH₄ 5 % – H₂ 6 %. The curve labeled as “guess” shows the seed parameters for the fit algorithm.

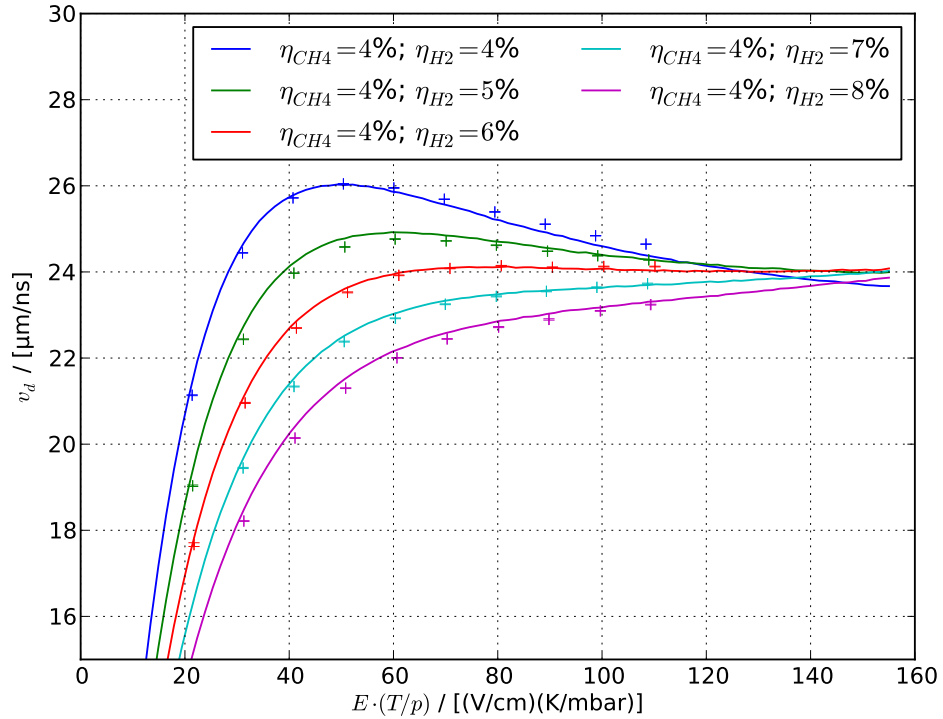
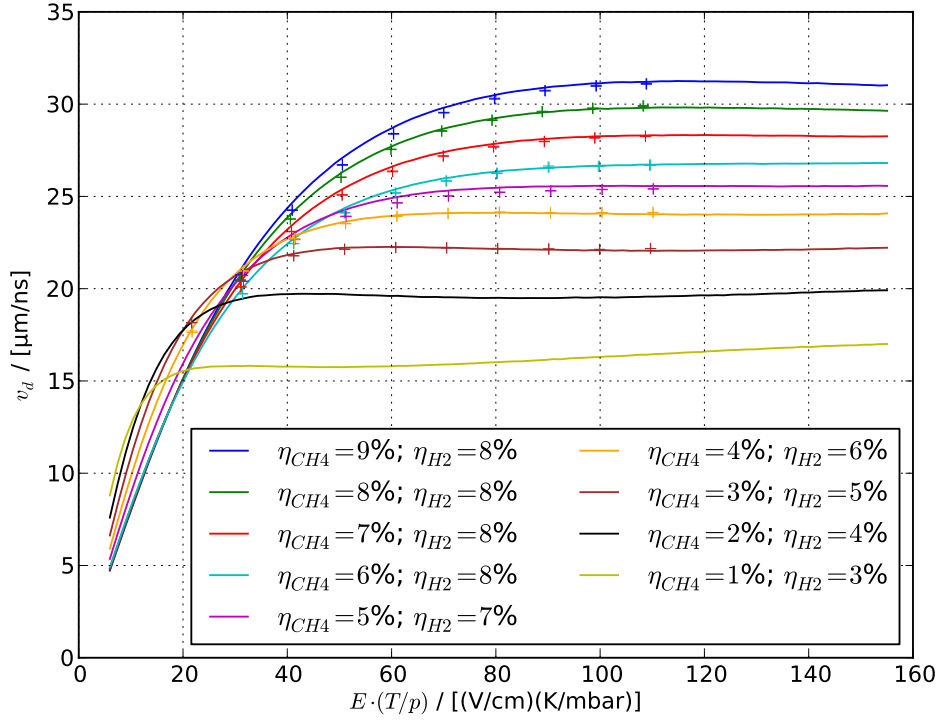
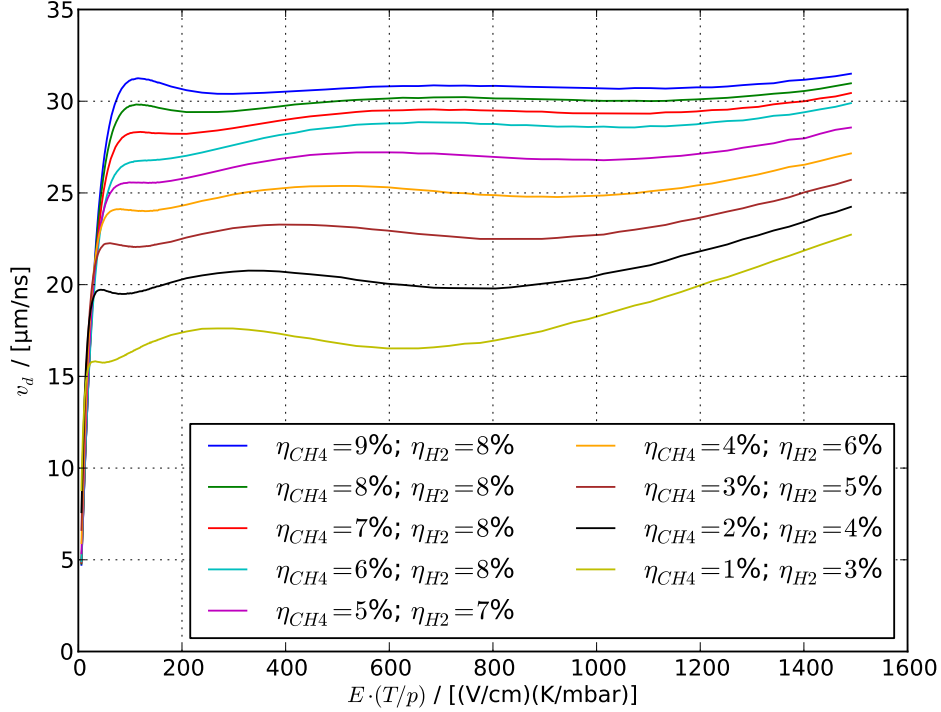


Figure 3.14.: Influence of the H₂ fraction on Ar-CH₄-H₂ mixtures with 4 % CH₄

Figure 3.15.: Ar-CH₄-H₂ mixtures that show a wide v_d plateauFigure 3.16.: Behaviour of Ar-CH₄-H₂ plateau mixtures (see fig. 3.15) up to very high E -fields (simulations only)

3. Results

For security reasons we did not use pure H_2 gas, but pre-mixed Ar 90 % – H_2 10 % that was mixed with pure Ar and CH_4 to get the desired gas fractions. The gas distributor guarantees a mix accuracy within 10 % relative to the specified fractions [15], so the pre-mixed Ar 90 % – H_2 10 % has a Hydrogen fraction between 9 % and 11 %. This uncertainty must be added to the mixing uncertainties from the UGMA. In fact, the pre-mix error dominates for mixtures with $\eta_{\text{H}_2} > 1$ %.

$$\sigma_{\eta_{\text{H}_2}} = \eta_{\text{H}_2} \cdot 0.1$$

4. Measuring the first Townsend coefficient

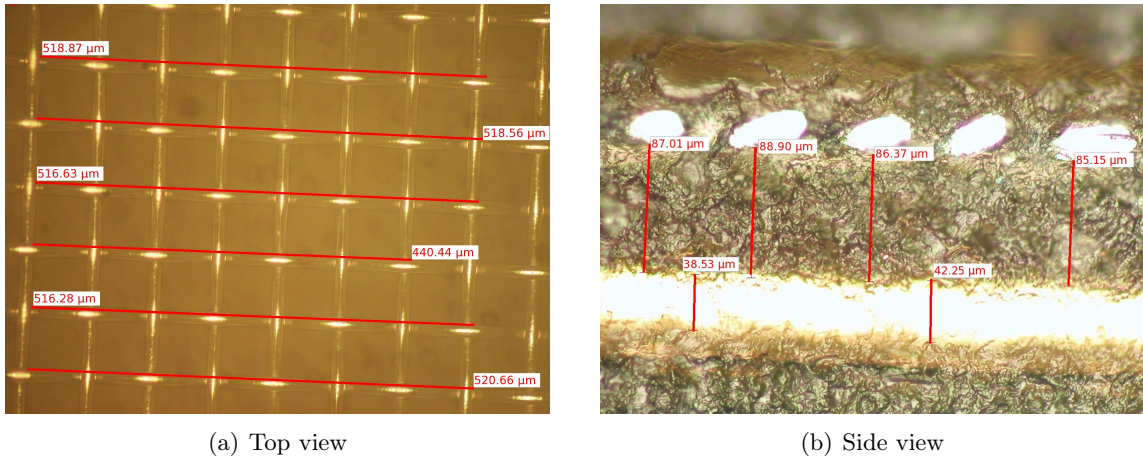


Figure 4.1.: Measurements of the MicroMeGaS geometry

As it was said in section 1.1.5, it is not possible to calculate the first Townsend coefficient α_T , because we do not know the probability of Penning and Jesse transfers. Therefore it is necessary to measure it directly.

The monitoring chambers include a slot for ^{55}Fe gamma sources, which can be used to measure the gain of the MicroMeGaS. Trying to use this to measure α_T proved to be futile, since the shape of the electric field in the amplification region is non-trivial and very inhomogeneous. Figure 4.1 shows some geometry measurements that were done with a microscope and table 4.1 shows the measurements in comparison with the nominal values taken from reference [7].

The values differ considerably, which is probably caused by the manufacturing process. The mesh is held in place by two layers of solder resist below, and one layer above it. The nominal layer width is $64\text{ }\mu\text{m}$, but the mesh is being pressed into the bottom layers during

Table 4.1.: Comparison of nominal MicroMeGaS geometry with measurements

MicroMeGaS parameter	nominal	measured
wire diameter / [μm]	18.0	14.1 ± 0.7
grating constant / [μm]	63.0	73.3 ± 0.6
mesh to pad distance / [μm]	128.0	87.7 ± 4.8

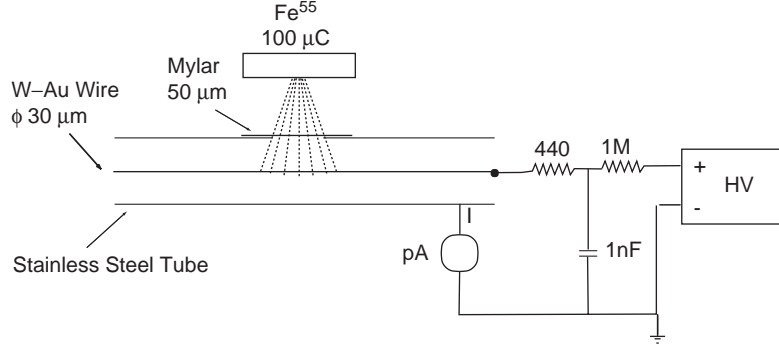


Figure 4.2.: Experimental setup by Auriemma et al. [16]

the lamination process of the top layer. This does *not* hinder the normal operation of the MicroMeGaS, since the exact distance between mesh and pad is not important as long as it (and thus the gain) is constant across the whole MicroMeGaS.

The reason for the difficulties with the α_T measurement is the fact that the mesh's grating constant is in the same order of magnitude as the distance between mesh and anode pads. This means one cannot approximate the electric field to be homogeneous like that of a plate capacitor. This is true for both the nominal and the measured geometries.

Auriemma et al. proposed a method of measuring α_T using a current measurement at a cylindrical wire chamber [16]. Their experimental setup can be seen in figure 4.2. The principle is simple: A radioactive source continuously ionises the gas in the wire chamber and the electrons drift towards the anode wire, where the gas amplification takes place. This creates a current which is proportional to the gain G and can be measured. By varying the anode voltage one can directly measure $\alpha_T(E)$ as follows.

4.1. Theory

The electric field in the gas volume is given by the anode wire radius r_A , the inner radius of the wire chamber r_C and the voltage U applied between the two.

$$E(r) = \underbrace{\frac{1}{\ln(r_C/r_A)}}_{:=a} \frac{U}{r} \quad (4.1)$$

The gain due to gas amplification depends on the integrated Townsend coefficient along the drift path.

$$\ln G = - \int_{r_0}^{r_A} \alpha_T(E(r)) dr = - \int_{E(r_0)}^{E(r_A)} \alpha_T(E) \underbrace{\frac{dr}{dE}}_{-a \frac{U}{E^2}} dE \quad (4.2)$$

The minus sign is due to the fact that $r_0 > r_A$. If the voltage is varied, the gain varies accordingly.

$$\begin{aligned}
 \frac{d \ln G}{dU} &= -\frac{d}{dU} \int_{r_0}^{r_A} \alpha_T(E(r)) dr = -\int_{r_0}^{r_A} \frac{d\alpha_T}{dE} \underbrace{\frac{dE}{dU}}_{=\frac{a}{r}=\frac{E}{U}} dr \\
 &= -\int_{E(r_0)}^{E(r_A)} \frac{d\alpha_T}{dE} \frac{E}{U} \underbrace{\frac{dr}{dE}}_{=-a\frac{U}{E^2}} dE = \int_{E(r_0)}^{E(r_A)} \frac{d\alpha_T}{dE} \frac{a}{E} dE \\
 &= \left[\alpha_T(E) \frac{a}{E} \right]_{E(r_0)}^{E(r_A)} + \underbrace{\int_{E(r_0)}^{E(r_A)} \alpha_T(E) \frac{a}{E^2} dE}_{\stackrel{(4.2)}{=} \frac{\ln G}{U}}
 \end{aligned}$$

Since gas amplification starts at very high electric fields, one can assume that the amplification at the beginning of the drift path is 0 for most electrons.

$$\begin{aligned}
 \alpha_T(E(r_0)) &= 0 \\
 \frac{d \ln G}{dU} &= \alpha_T(E(r_A)) \frac{a}{E(r_A)} + \frac{\ln G}{U}
 \end{aligned}$$

One can now solve for α_T and thus measure it directly by varying the voltage.

$$\alpha_T(E(r_A)) = \left(\frac{d \ln G}{dU} - \frac{\ln G}{U} \right) \frac{E(r_A)}{a} \stackrel{(4.1)}{=} \left(\frac{d \ln G}{d \ln U} - \ln G \right) \frac{1}{r_A}$$

The gain strongly depends on U , so it is always $d \ln G / d \ln U \gg \ln G$ [16]. This means that one can measure α_T even if the value of G is not known, but only a proportional value like the current I .

$$\begin{aligned}
 G &= \frac{I}{I_0} \\
 \alpha_T(E(r_A)) &= \left(\frac{d \ln I / I_0}{d \ln U} - \ln I / I_0 \right) \frac{1}{r_A} \\
 &= \left(\frac{d \ln I}{d \ln U} - \ln I / I_0 \right) \frac{1}{r_A} \\
 &\approx \left(\frac{d \ln I}{d \ln U} \right) \frac{1}{r_A}
 \end{aligned}$$

4.2. Modifications

The most difficult part with this experimental setup is the current measurement, since the currents involved are very small (\sim pA). We therefore modified the setup to increase the primary (unamplified) current I_0 and thus I . The new setup can be seen in figure 4.3. The radioactive source was replaced with a hot cathode that emits electrons due to their thermal

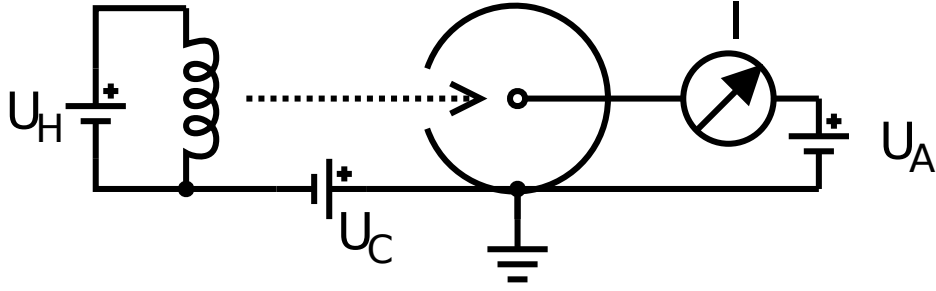


Figure 4.3.: Modified setup for the α_T measurement. We use an anode wire with a diameter of $50\mu\text{m}$ and a cathode cylinder with an inner diameter of about 1 cm .

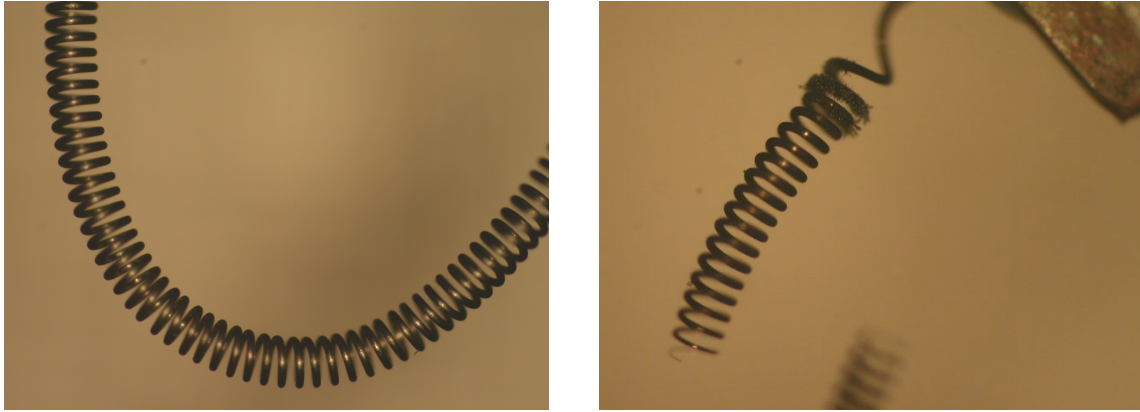


Figure 4.4.: Typical light bulb filament before (left) and after (right) the use as hot cathode in gas

energy. These electrons are transported to the amplification region by an electric drift field. The currents achievable with this method are orders of magnitude higher than the ones created by (reasonably dimensioned) radioactive sources.

The wire chamber is not exactly cylindrical, since it needs an opening for the electrons. This deviation from the ideal cylindrical field will skew the results for α_T somewhat and should be eliminated for high precision measurements (see section 4.3). Since we are only trying to demonstrate the feasibility of the measurement, these effects will not be discussed here.

The hot cathode is a simple bicycle light bulb of which the glass body was removed. Unfortunately the filament degrades as soon as one applies a voltage to it. The life time of the lamp depends on the applied voltage as well as the gas mixture in which it is operated. Especially CO_2 proved to be a hazard for the filament. We assume that the CO_2 in the gas mix dissociates at the hot cathode and then oxidises the filament. Figure 4.4 shows a typical filament before and after its use.

Since the filament “suffers” during operation, the primary current I_0 will also change with time. To be able to correct for this, one can choose a U_A profile that inserts a predefined reference voltage in between the voltage ramp steps. The current can then be normalised to that of the reference points. One also has to consider the temperature and pressure

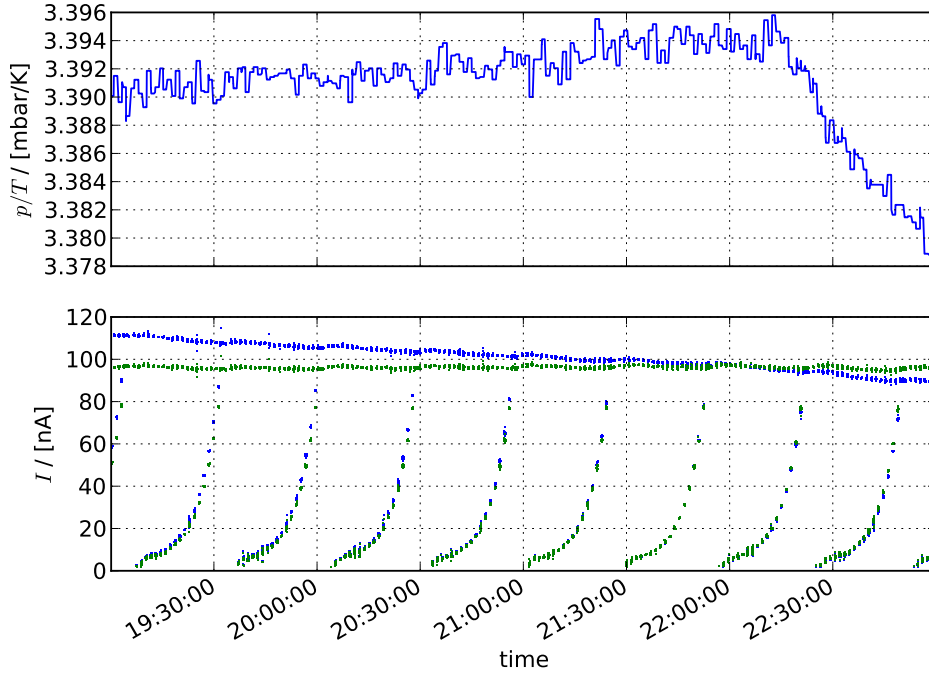


Figure 4.5.: Measured (blue) and corrected (green) anode current of P5

dependencies and correct for those influences on the current. The Townsend coefficient can be expressed as a function of $E^{T/p}$ and a factor p/T , so one gets

$$\begin{aligned}
 G = \frac{I}{I_0} &= \exp \left(\int \alpha_T(E^{T/p}(r), T/p) dr \right) = \exp \left(\int f(E^{T/p}(r)) \frac{p}{T} dr \right) \\
 &= \left(\exp \left(\int f(E^{T/p}(r)) dr \right) \right)^{\frac{p}{T}} = \underbrace{\left(\exp \left(\int f(E^{T/p}(r)) \frac{p_0}{T_0} dr \right) \right)^{\frac{T_0 p}{p_0 T}}}_{:= G' = I'/I_0} \\
 I &= I' \frac{T_0 p}{p_0 T} \\
 I' &= I \frac{p_0 T}{T_0 p}.
 \end{aligned}$$

Figures 4.5 and 4.6 show the measured and corrected current for the α_T measurements of P5 (Ar 95% – CH₄ 5%).

Figures 4.7 and 4.8 show the simulated and measured Townsend coefficients of P5 and P7. As one can see, the measurements are somewhat off in comparison with the simulations. One has to consider, though, that the simulations do not take Penning and Jesse effects into account, so the measured α_T is expected to be higher than the simulation. Also there has been no thorough check for systematic influences from the skewed electric field or the possible influence of the voltages on the number of electrons that make it from the drift field into the cathode tube.

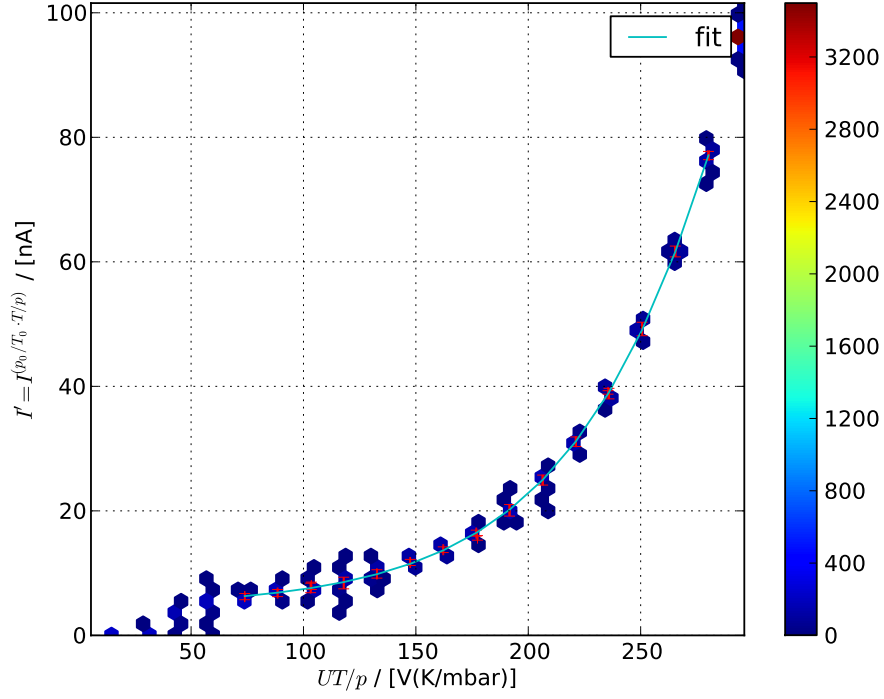


Figure 4.6.: Anode current vs voltage of P5. The fit is a function of the form $c + \exp(a_0 + a_1x + a_2x^2 + a_3x^3)$.

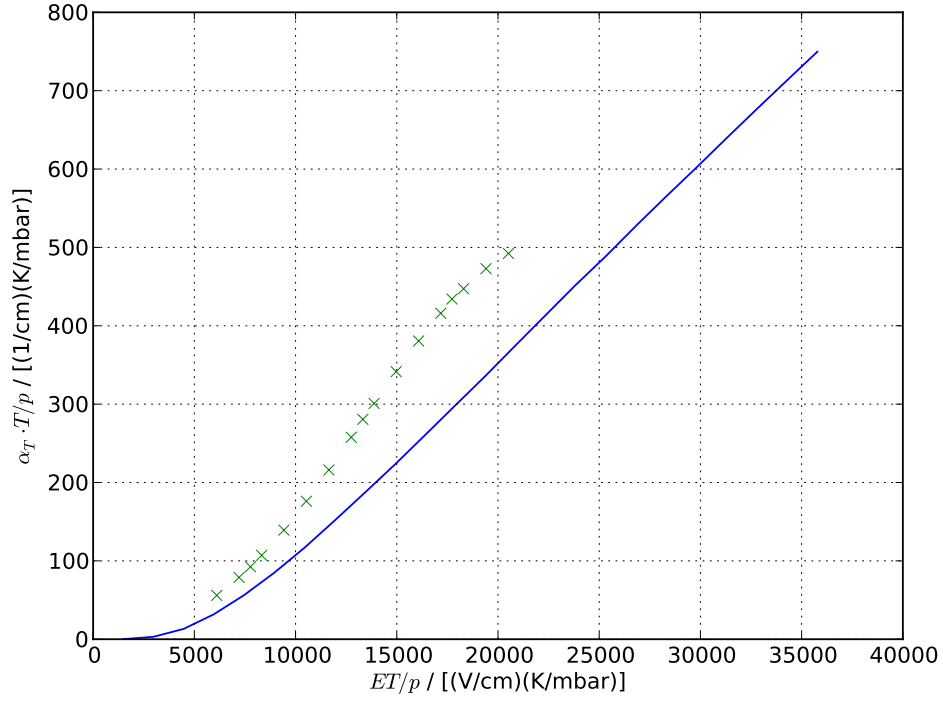
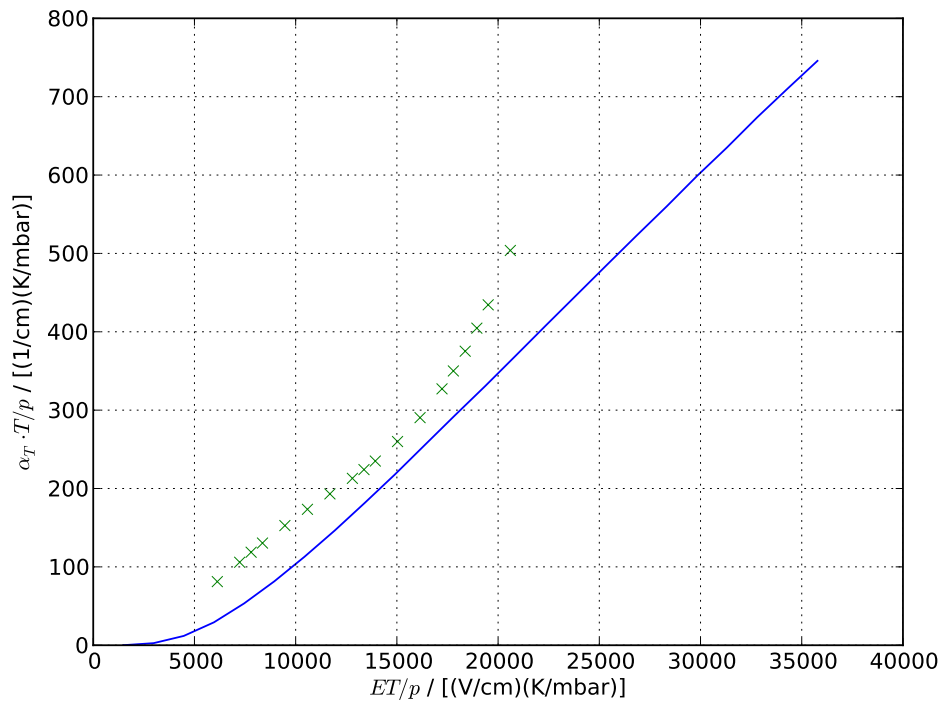


Figure 4.7.: Measured and simulated α_T of P5

Figure 4.8.: Measured and simulated α_T of P7

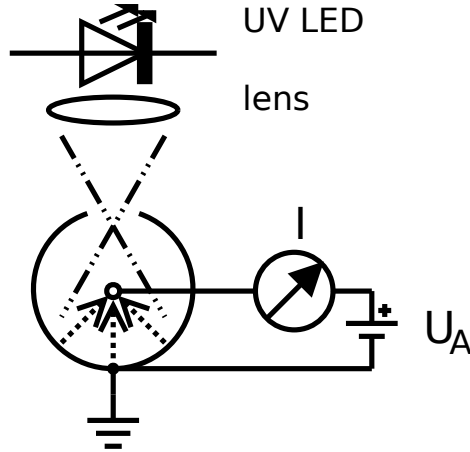


Figure 4.9.: Proposed upgrade of the α_T measurement setup

4.3. Future improvements

The modified method of α_T measurement proved to be feasible and first measurements show promise for future improvements. The current setup mainly suffers from the degradation of the hot cathode as well as the field distortions due to the necessary opening in the cathode tube. To improve the setup in those regards, we suggest an alternative setup as seen in figure 4.9.

A UV-LED could create free electrons directly inside the cathode tube utilising the photo-electric effect. Not only would the LED allow for continuous stable operation, but it would also reduce the impact of the skewed electric field. Since we could make the necessary hole in the cathode tube comparatively small and the electrons traverse the electric field on the far side of the tube, the effects due to field distortion can be expected to be minimal.

A possible disadvantage of this setup might be that the UV-LED excites the deployed quenchers in the gas and thus interferes with the gas electron interaction. This has to be investigated.

5. Conclusion

The T2K/ND280 monitoring chambers were successfully used for the precision measurement of electron drift velocities at low electric fields ($< 400 \text{ V/cm}$). The systematic errors were estimated to be not larger than 4 ‰, while the statistical errors are in the order of 1 ‰ or better. The general shape of the simulations is well reproduced by the measurements, though deviations that cannot be attributed to the mixing uncertainties remain. It was shown that one can visualise the influence of different additive fractions by reducing the drift curve to its working point, the v_d maximum. This is not true for all mixtures as was seen at the example of some Ar-CH₄-H₂ mixtures, which show a plateau or region of weak E^T/p -dependence instead of a maximum.

A simplified depiction of the different influences of the additives on the working points can be seen in figure 5.1. Both CF₄ and CH₄ generally increase the drift velocity, but one needs much less CF₄ than CH₄ to achieve the same effect. Conversely, to prevent v_d deviations, one would have to control the CF₄ fraction to a higher precision than an equivalent CH₄ fraction. This “sensitivity” of CF₄ mixtures is amplified by the fact that their working point widths are smaller than those of CH₄ mixtures. CO₂ and iC₄H₁₀ pull the working point drift velocity to a value around 50 $\mu\text{m/ns}$ and H₂ always pulls the working points down. Compared to the other additives, H₂ causes a much stronger widening of the drift velocity maxima,

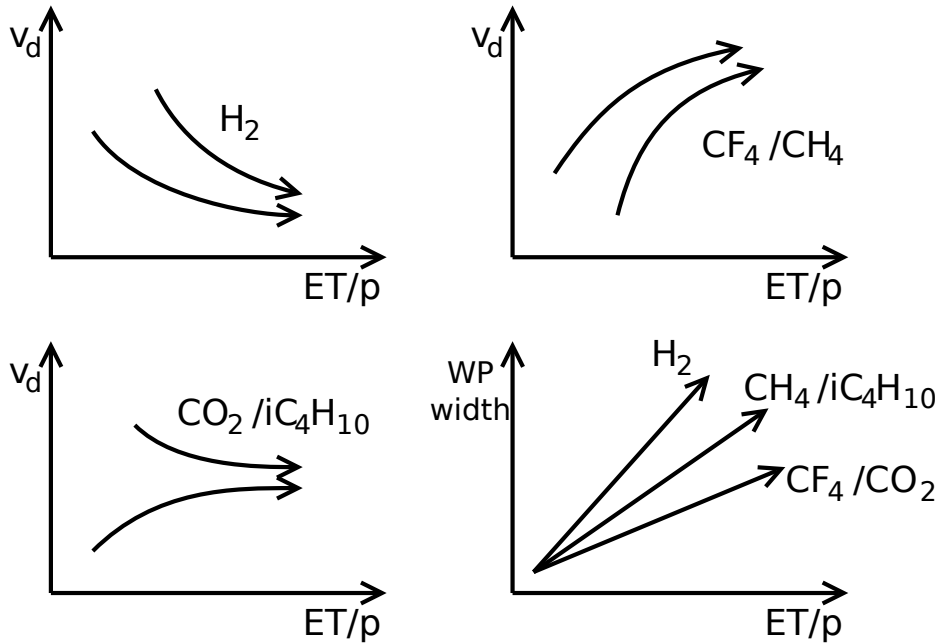


Figure 5.1.: Simplified influences of the additives on the working points

5. Conclusion

which leads to the formation of the aforementioned plateaus. Mixtures with H_2 are thus less susceptible to changes in E^T/p .

A modified version of the α_T measurement method introduced by Auriemma et al. [16] was shown to be a feasible alternative for future measurements. Further modifications that might mitigate the problems with the hot cathode and skewed electric field were suggested and should be investigated.

6. Acknowledgements

I want to thank the T2K group under Stefan Roth at III. Physikalisches Institut B for supporting me during the work on my thesis. Thanks also go to Johannes Hellmund, Fabian Schneider and Jochen Steinmann for proofreading this thesis and I especially want to thank Jochen Steinmann for his tireless work at the UGMA and his help with the monitoring chambers. I also want to thank Stephen Biagi and Heinrich Schindler for their e-mail correspondence and support in regards to Magboltz and Garfield++ as well as all my colleagues at Halle Physik for providing an enjoyable working atmosphere and occasionally cake.

References

- [1] K. Aamodt et. al. Rapidity and transverse momentum dependence of inclusive J/ψ production in pp collisions at $\sqrt{s} = 7$ TeV. *Physics Letters B*, 704(5):442 – 455, 2011. ISSN 0370-2693. doi: <http://dx.doi.org/10.1016/j.physletb.2011.09.054>. URL <http://www.sciencedirect.com/science/article/pii/S0370269311011270>.
- [2] W. Blum, W. Riegler, and L. Rolandi. *Particle Detection with Drift Chambers*. Particle Acceleration and Detection. Springer, 2008. ISBN 9783540766834. URL <http://books.google.de/books?id=RgxU1AXv0RAC>.
- [3] J. Beringer et al., editor. *Particle Physics Booklet*. Particle Data Group, 2012.
- [4] Steven Biagi. Cross sections used by Magboltz 7.1, July 2013. URL <http://rjd.web.cern.ch/rjd/cgi-bin/cross>.
- [5] H. Reithler. private communication. III. Physikalisches Institut A, RWTH Aachen, 2010.
- [6] O. Schäfer. LCTPC website, 2013. URL <http://www.lctpc.org>.
- [7] D. Karlen et al. Time projection chambers for the T2K near detectors. *Nuclear Instruments and Methods in Physics Research Section A: Accelerators, Spectrometers, Detectors and Associated Equipment*, 637(1):25 – 46, 2011. ISSN 0168-9002. doi: 10.1016/j.nima.2011.02.036. URL <http://www.sciencedirect.com/science/article/pii/S0168900211003421>.
- [8] T2K Collaboration. T2K website, 2013. URL <http://www.t2k.org>.
- [9] Dennis Terhorst. Entwicklung einer Monitorkammer zur Überwachung des Driftkammergases der T2K-TPC. Diplomarbeit, III. Physikalisches Institut B, RWTH Aachen, November 2008.
- [10] Jochen Steinmann. Inbetriebnahme der Monitorkammern für die TPC des T2K-Experiments. Diplomarbeit, III. Physikalisches Institut B, RWTH Aachen, Januar 2010.
- [11] Teja Wrobel. Systematische Messungen der Driftgeschwindigkeit und der Gasverstärkung mithilfe einer Gasmonitorkammer für das T2K-Experiment. Diplomarbeit, III. Physikalisches Institut B, RWTH Aachen, Mai 2011.
- [12] Jochen Steinmann. *Design, construction and commissioning of a universal and mobile gas-mixing-system*. Doktorarbeit, III. Physikalisches Institut B, RWTH Aachen, 2013.
- [13] DIN 1343: Referenzzustand, Normzustand, Normvolumen. Deutsche Norm, Deutsches Institut für Normung e.V., 1990.
- [14] DS18S20 high-precision 1-wire digital thermometer. Datasheet, Maxim Integrated, 2010.

REFERENCES

- [15] DIN EN ISO 14175: Schweißzusätze – Gase und Mischgase für das Lichtbogenschweißen und verwandte Prozesse. Deutsche Norm, Deutsches Institut für Normung e.V., 2008.
- [16] G. Auriemma, D. Fidanza, G. Pirozzi, and C. Satriano. Experimental determination of the Townsend coefficient for Argon-CO₂ gas mixtures at high fields. *Nuclear Instruments and Methods in Physics Research A*, 2003.
- [17] P.J. Linstrom and W.G. Mallard, editors. *NIST Chemistry WebBook, NIST Standard Reference Database Number 69*. National Institute of Standards and Technology, Gaithersburg MD, 20899, July 2013. URL <http://webbook.nist.gov/chemistry/>.

A. Gas properties

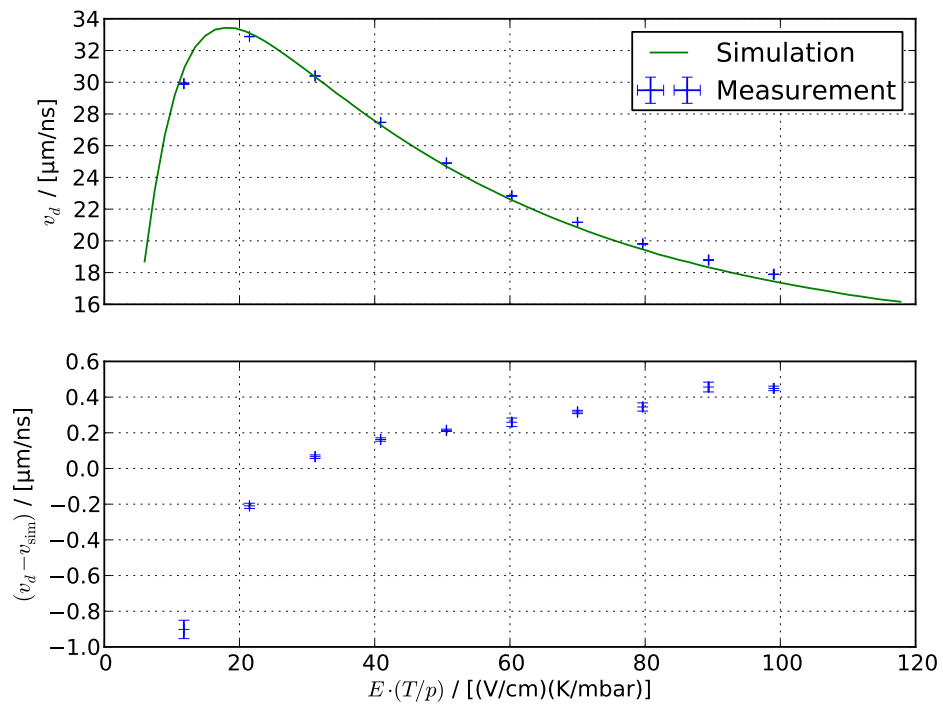
Gas	$\rho_0/[\text{g/l}]$	$M_{mol}/[\text{g/mol}]$	$W_\alpha/[\text{eV}]$	$W_\beta/[\text{eV}]$
H ₂	0.089885	2.01588	36.4	36.3
He	0.178488	4.002602	46.0	42.3
N ₂	1.250386	28.0134	—	—
O ₂	1.429033	31.9988	—	—
Ar	1.783956	39.948	26.4	26.3
Xe	5.898003	131.293	21.7	21.9
CO	1.250501	28.0101	—	—
CO ₂	1.976813	44.0095	34.3	32.8
CH ₄	0.717459	16.0425	29.1	27.1
CF ₄	3.946447	88.0043	—	—
C ₂ H ₄	1.261111	28.0532	—	—
C ₂ H ₆	1.355125	30.069	26.6	24.4
C ₃ H ₈	2.010037	44.0956	—	—
iC ₄ H ₁₀	2.688009	58.1222	—	—
C ₄ H ₁₀	2.688697	58.1222	—	—
F ₆ S	6.615833	146.055	—	—

ρ_0 at $T = 0^\circ\text{C}$, $p = 1013.25 \text{ mbar}$
 ρ_0 and M_{mol} taken from [17], $W_{\alpha/\beta}$ from [2]

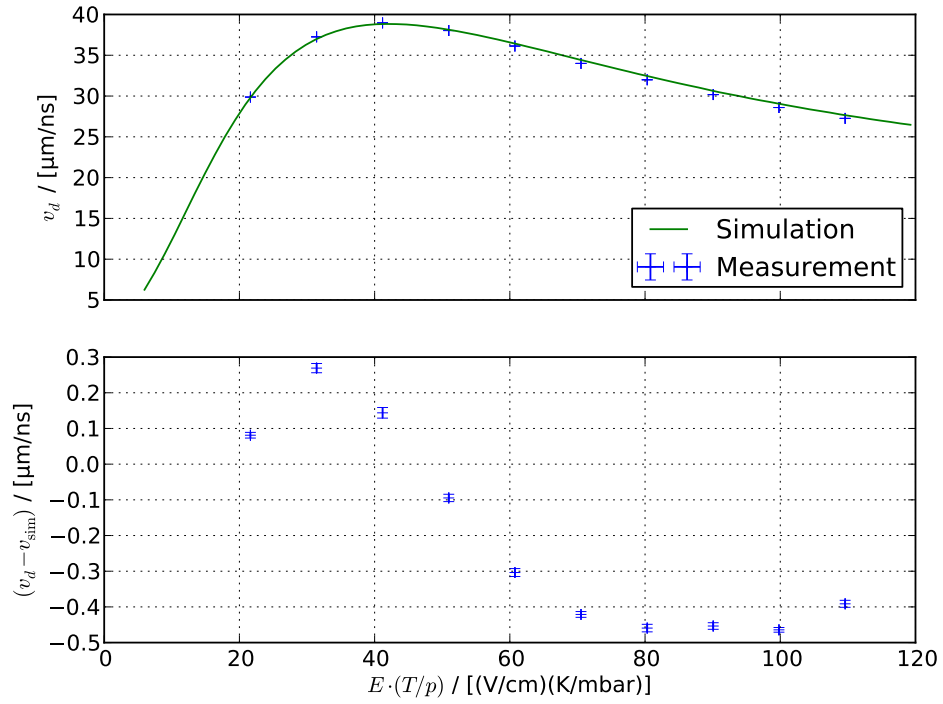
B. Measurements

B.1. Ar-CH₄-CO₂ mixtures

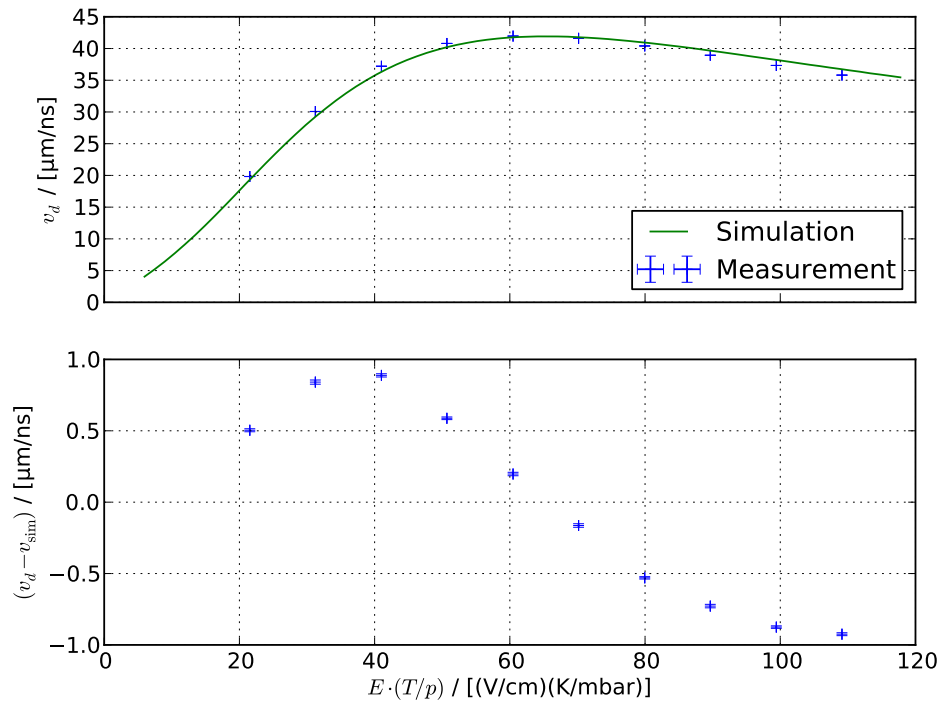
Ar 97 % – CH₄ 3 % – CO₂ 0 %



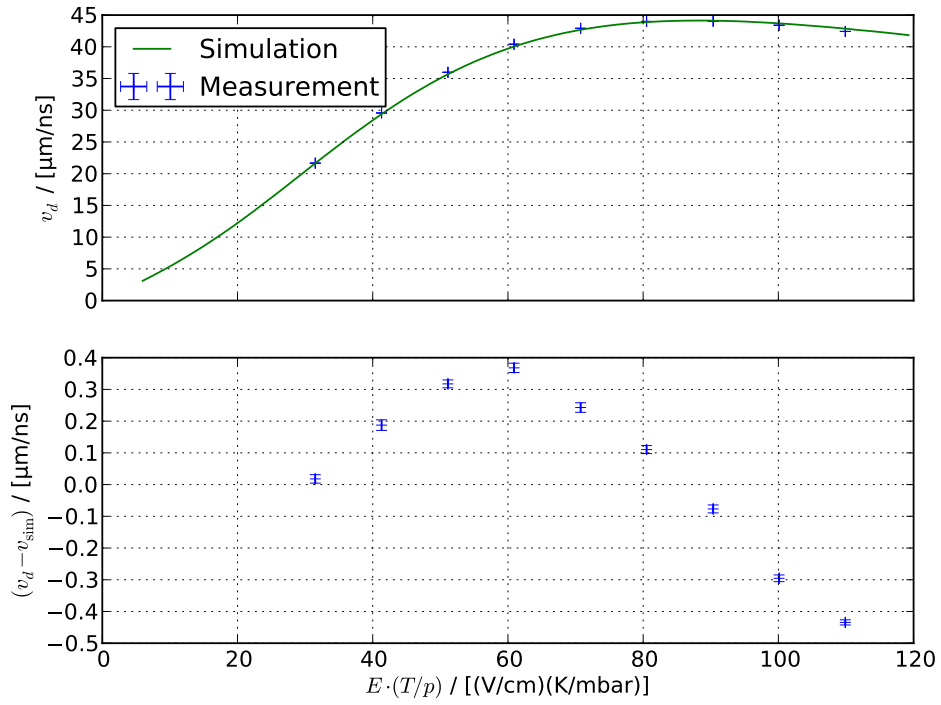
Ar 96 % – CH₄ 3 % – CO₂ 1 %



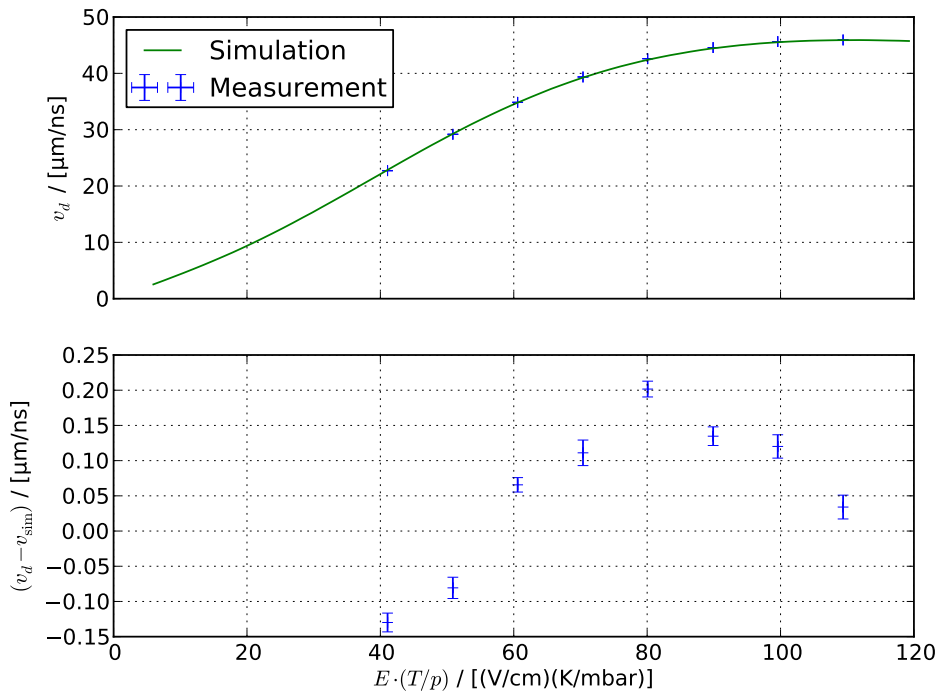
Ar 95 % – CH₄ 3 % – CO₂ 2 %



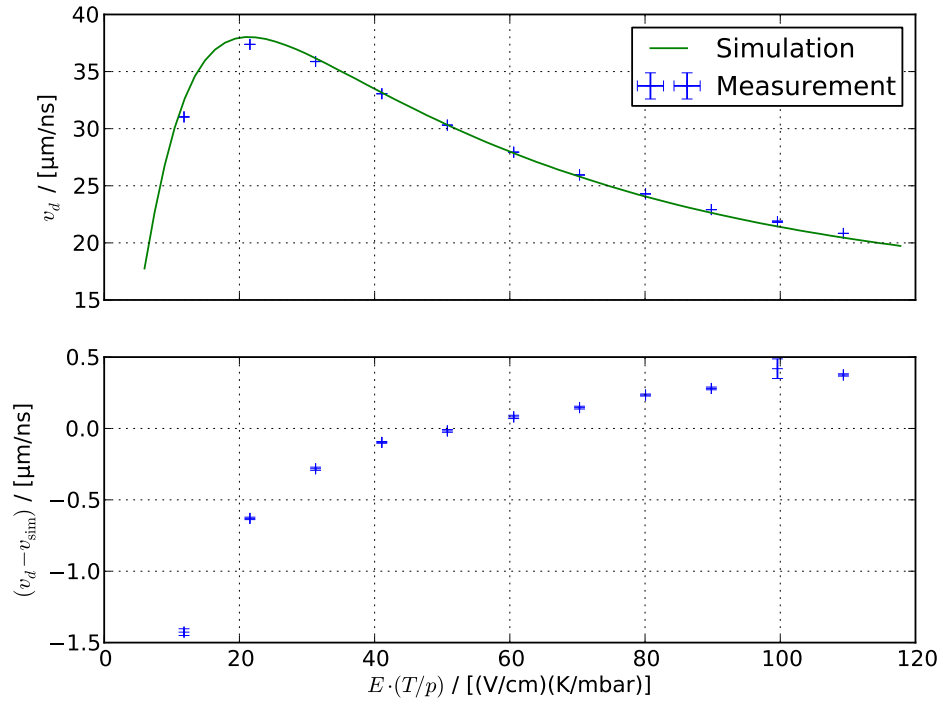
Ar 94 % – CH₄ 3 % – CO₂ 3 %



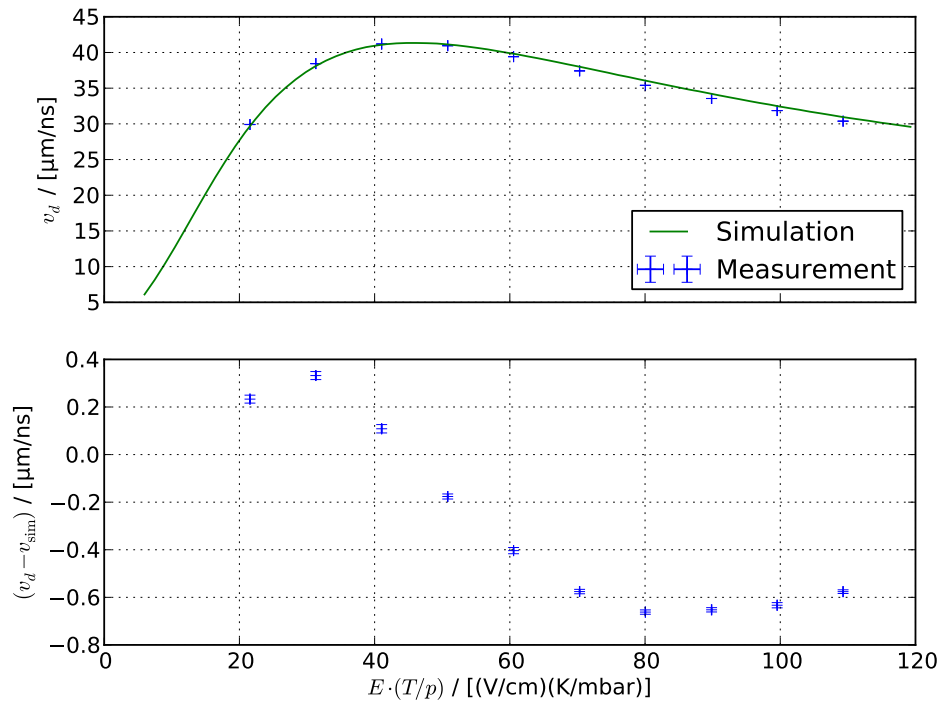
Ar 93 % – CH₄ 3 % – CO₂ 4 %



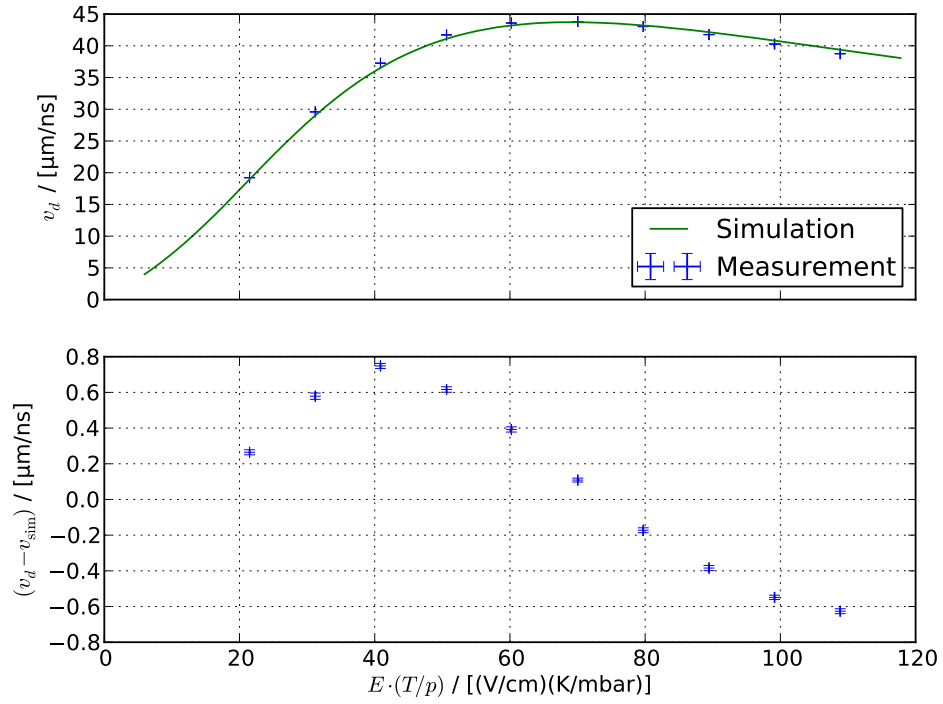
Ar 96 % – CH₄ 4 % – CO₂ 0 %



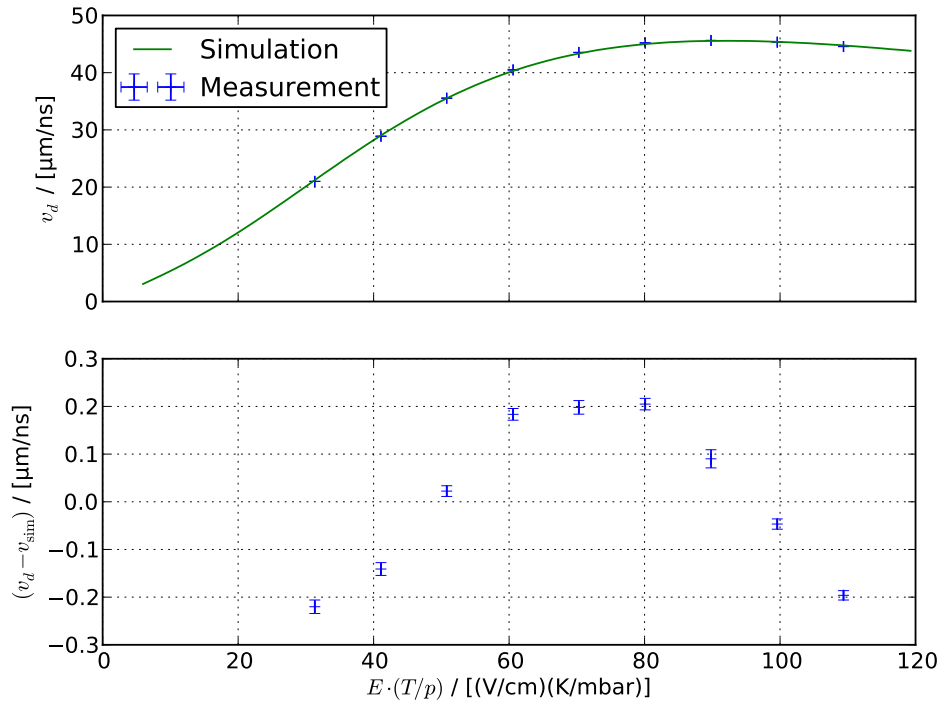
Ar 95 % – CH₄ 4 % – CO₂ 1 %



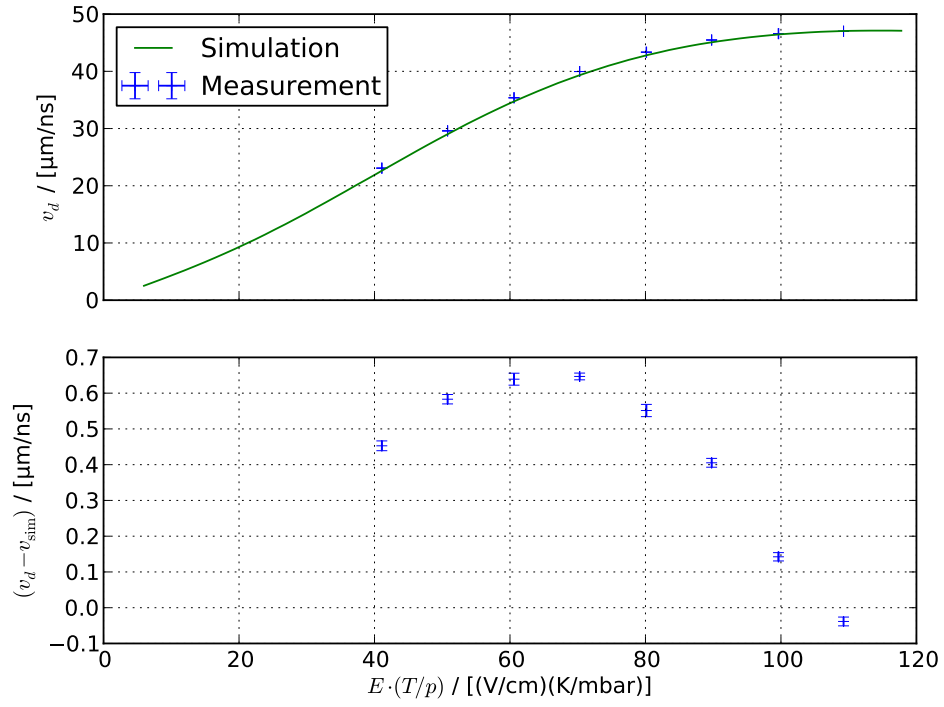
Ar 94 % – CH₄ 4 % – CO₂ 2 %



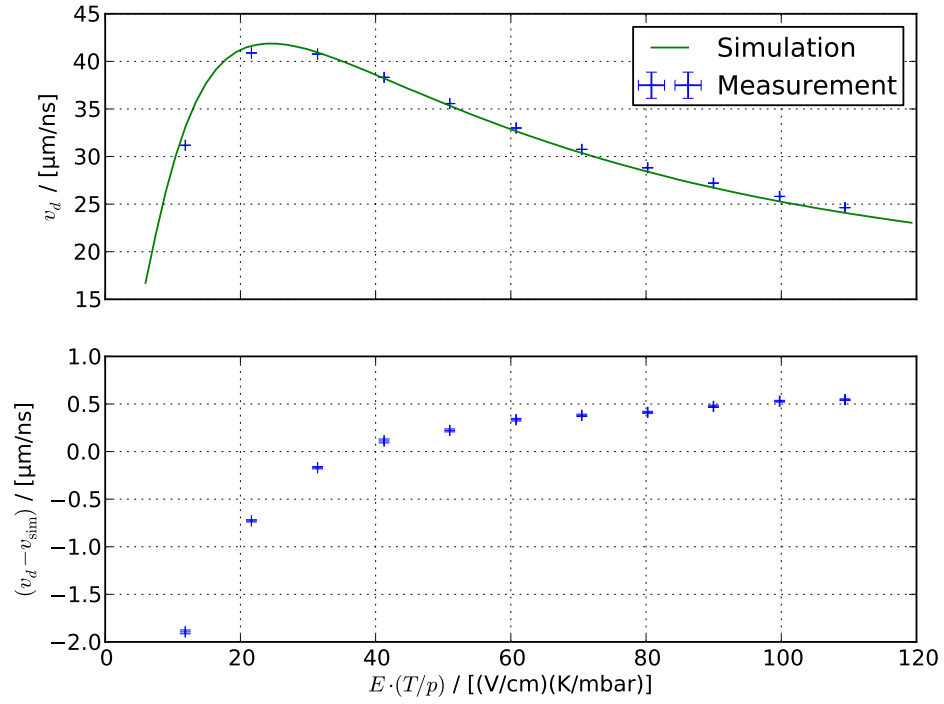
Ar 93 % – CH₄ 4 % – CO₂ 3 %



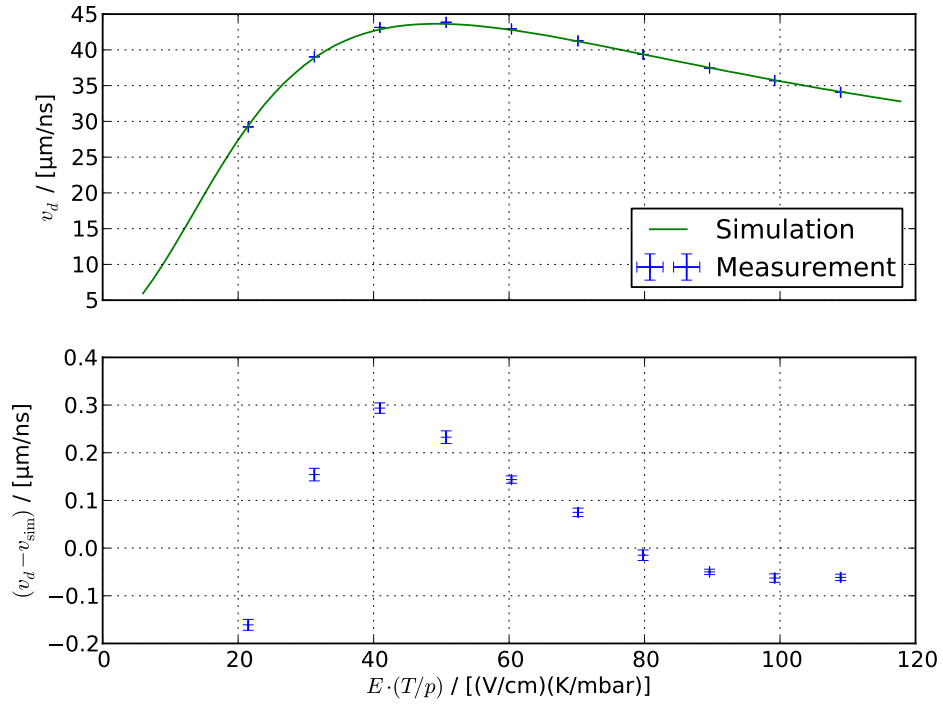
Ar 92 % – CH₄ 4 % – CO₂ 4 %



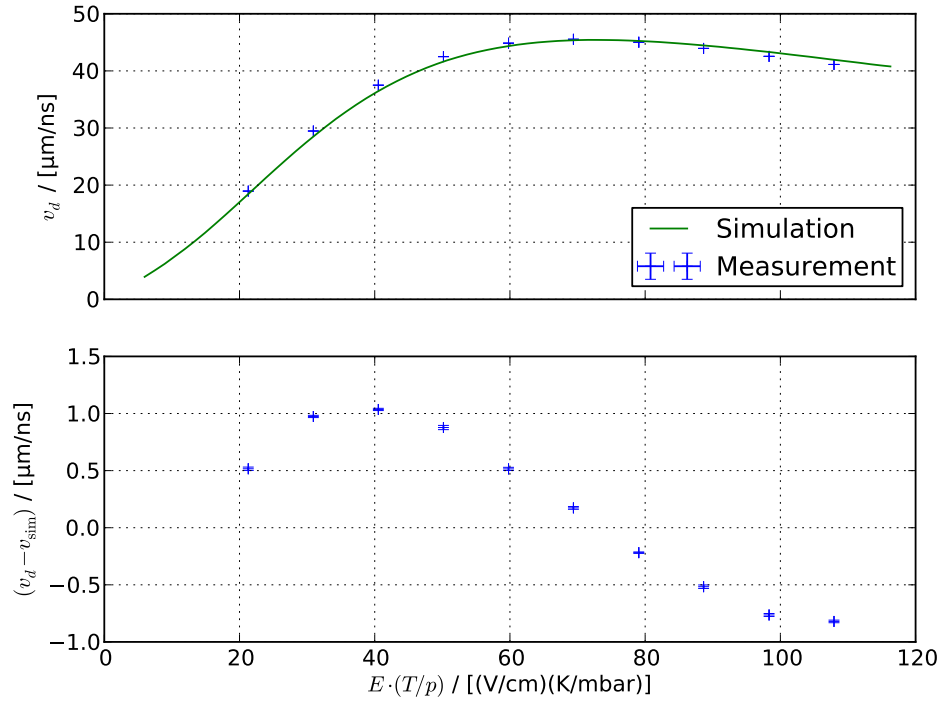
Ar 95 % – CH₄ 5 % – CO₂ 0 %



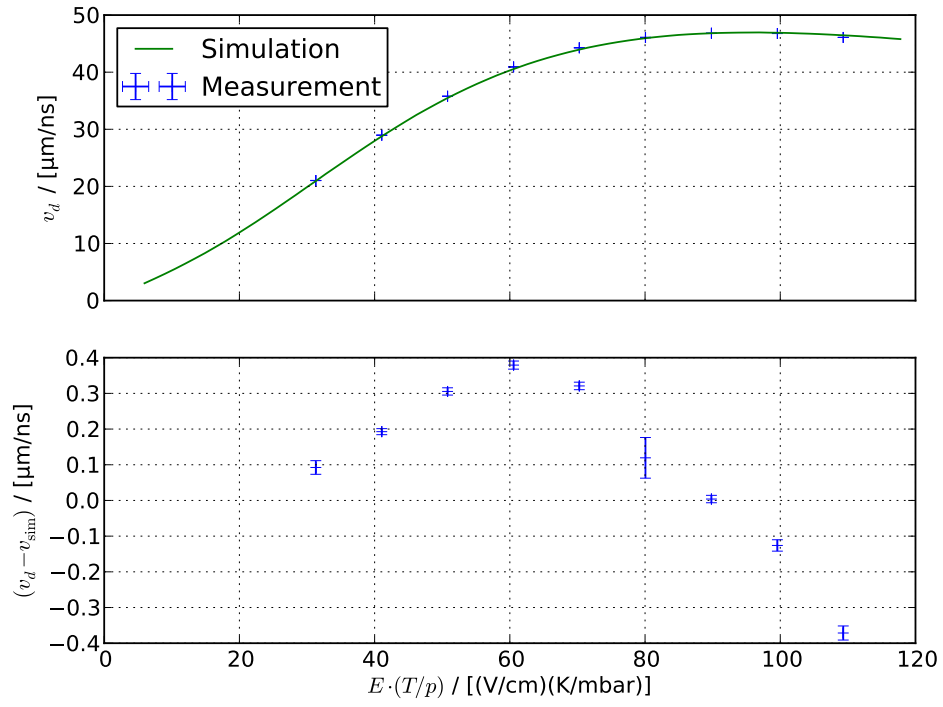
Ar 94 % – CH₄ 5 % – CO₂ 1 %



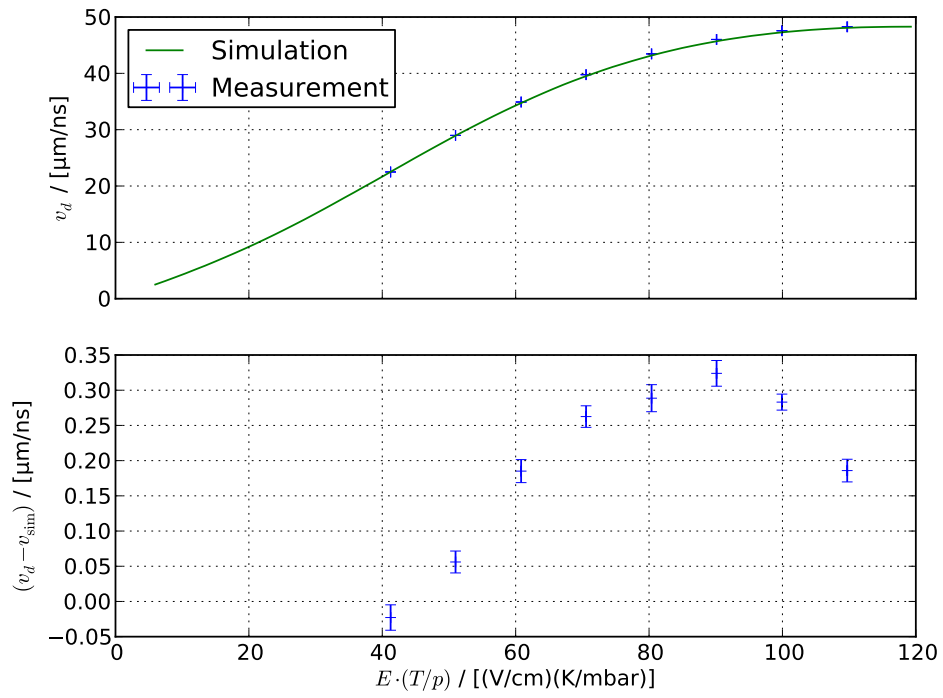
Ar 93 % – CH₄ 5 % – CO₂ 2 %

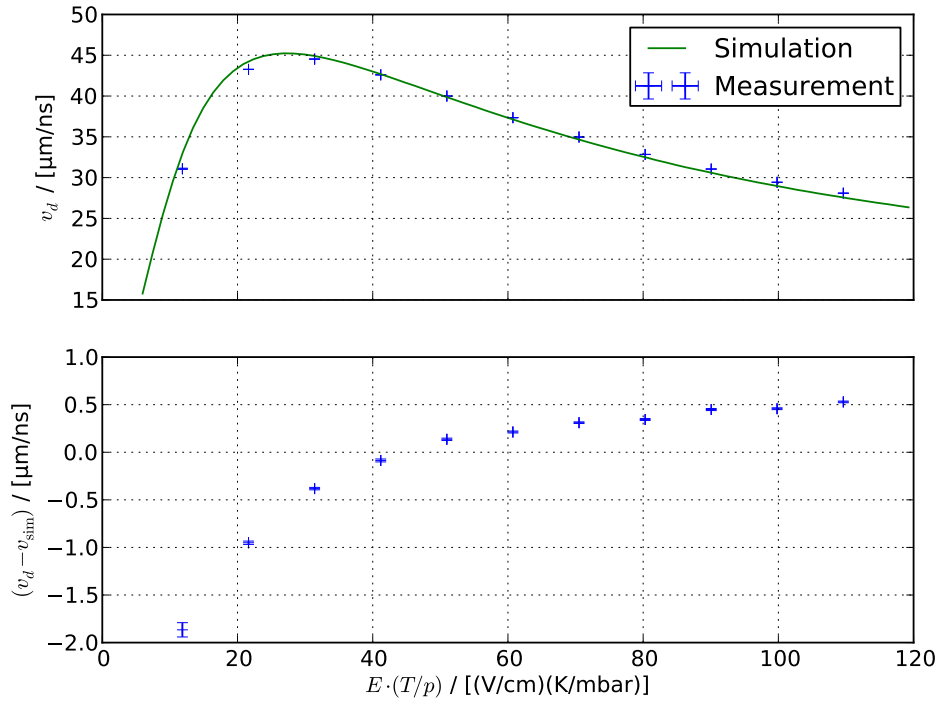
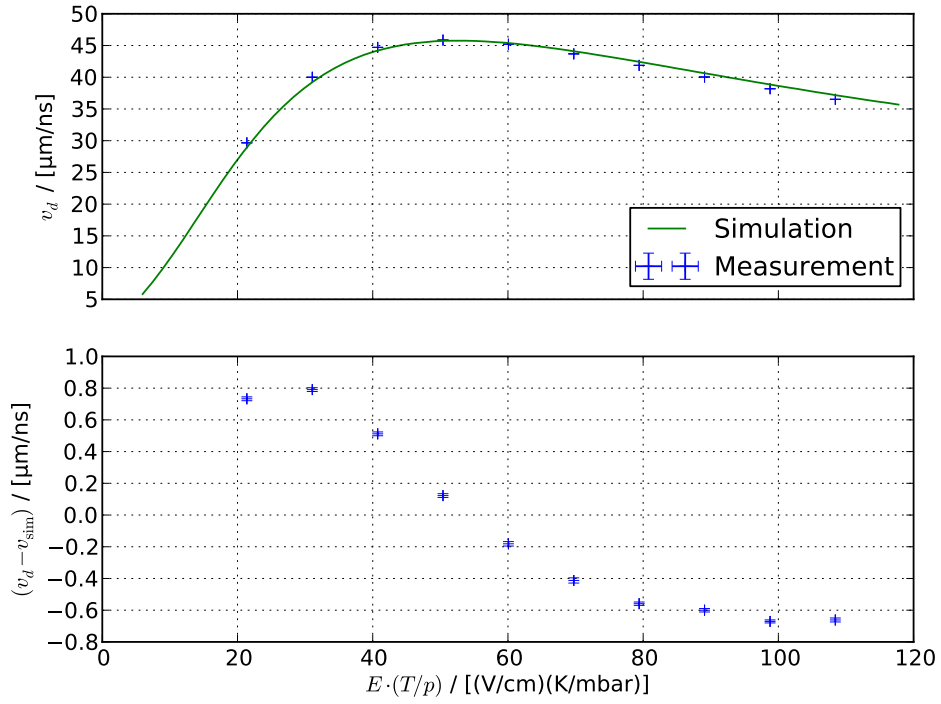


Ar 92 % – CH₄ 5 % – CO₂ 3 %

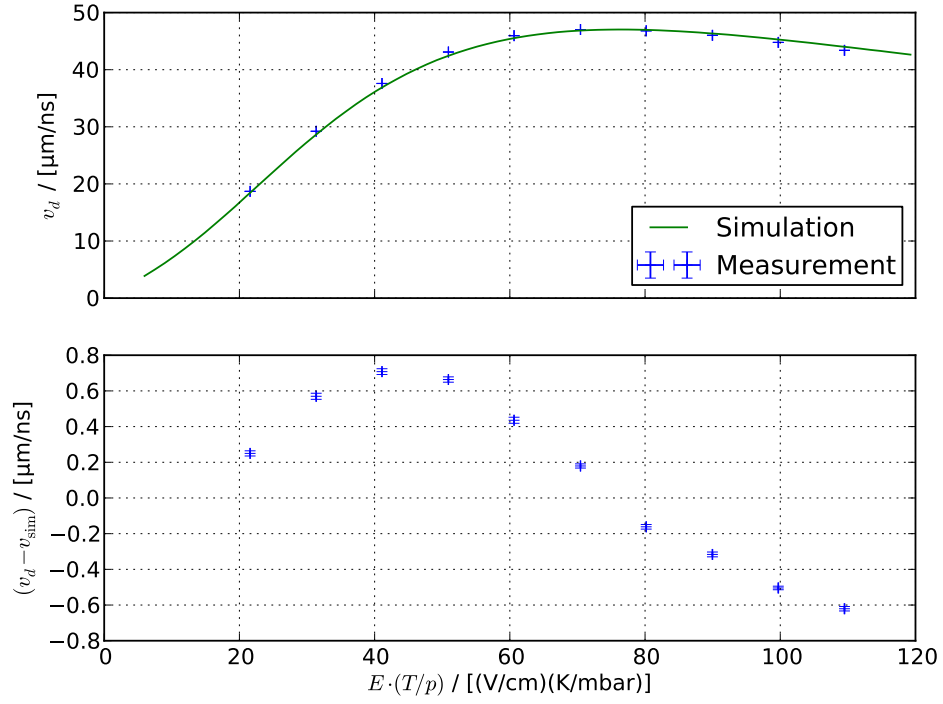


Ar 91 % – CH₄ 5 % – CO₂ 4 %

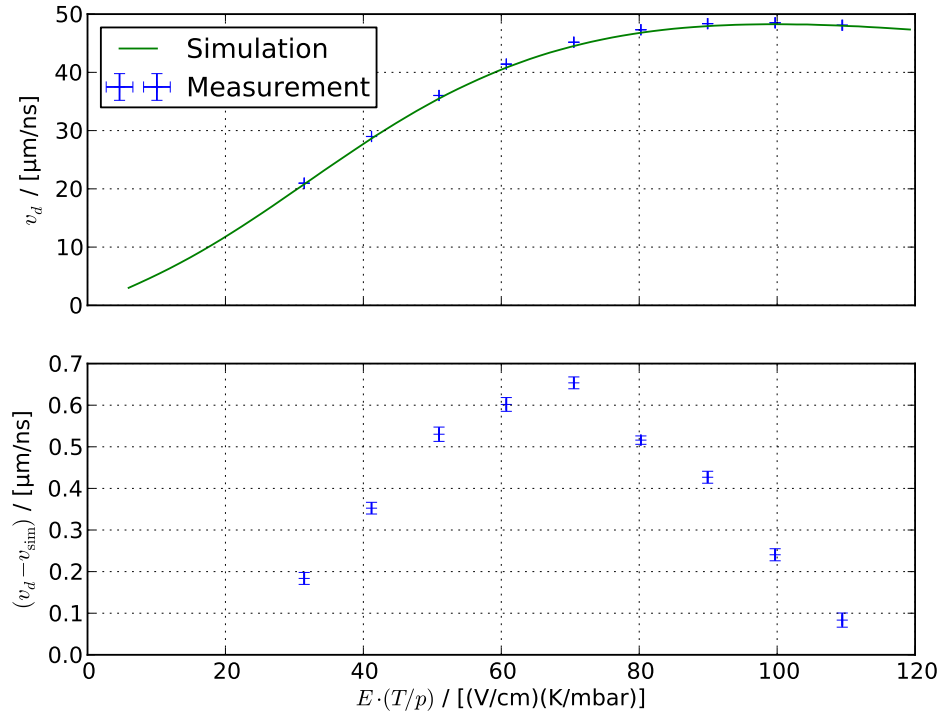


Ar 94 % – CH₄ 6 % – CO₂ 0 %Ar 93 % – CH₄ 6 % – CO₂ 1 %

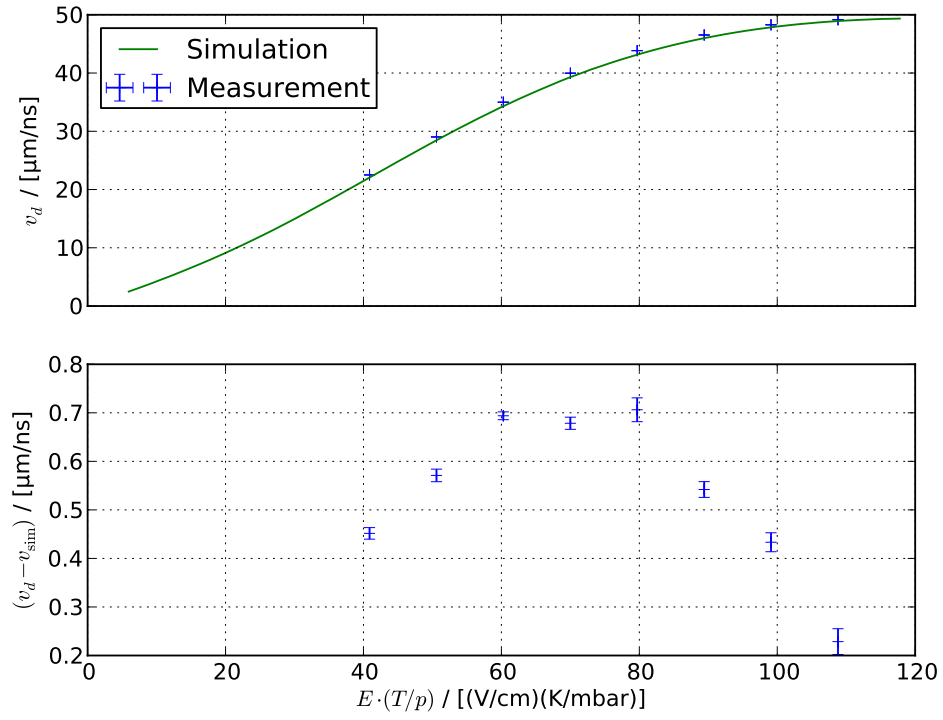
Ar 92 % – CH₄ 6 % – CO₂ 2 %



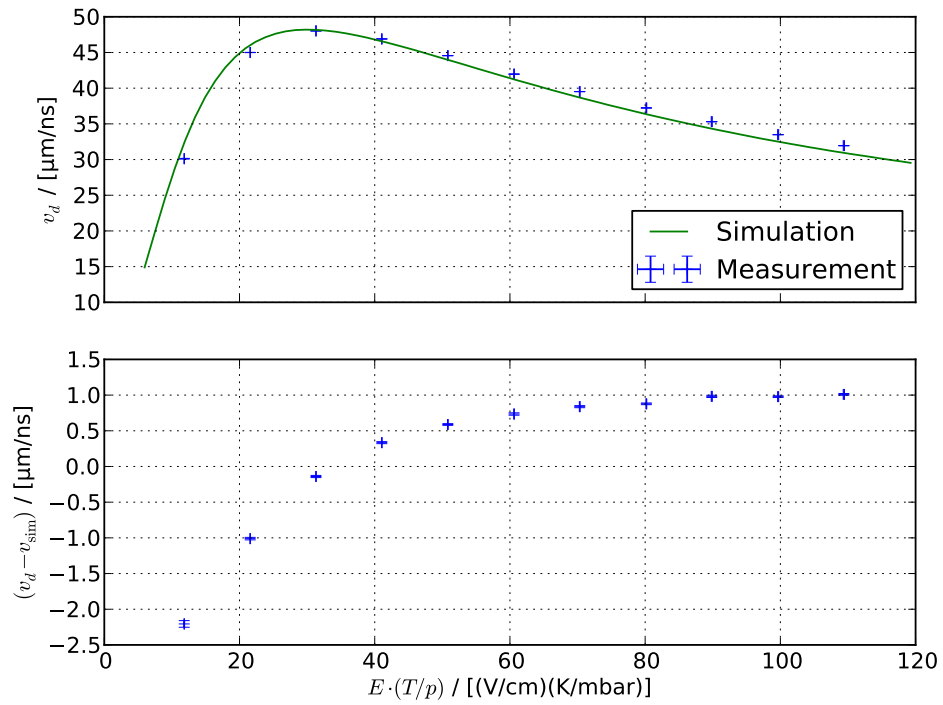
Ar 91 % – CH₄ 6 % – CO₂ 3 %



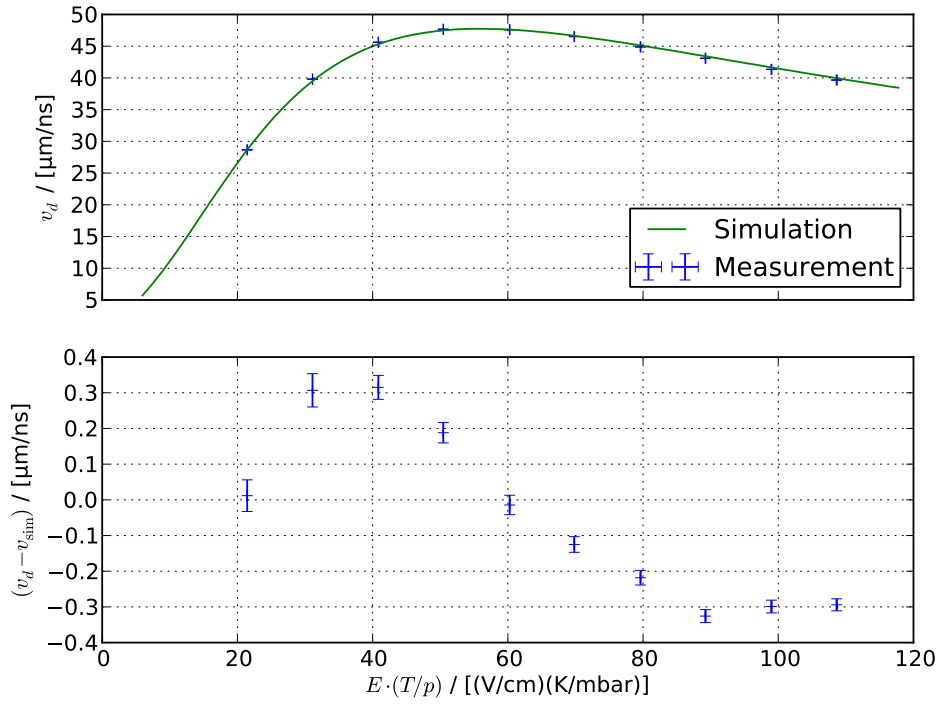
Ar 90 % – CH₄ 6 % – CO₂ 4 %



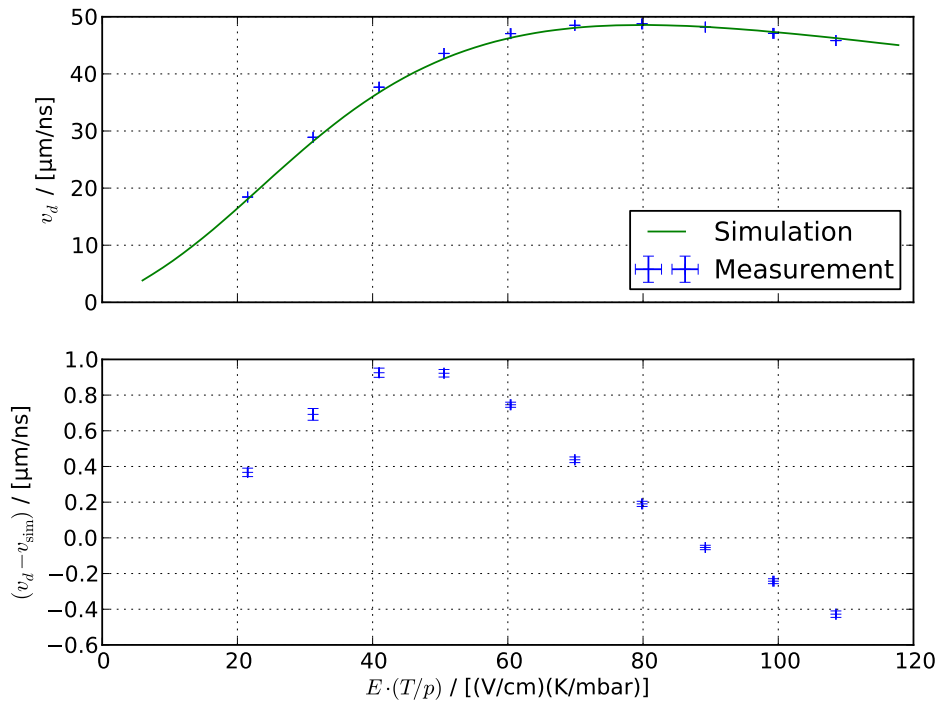
Ar 93 % – CH₄ 7 % – CO₂ 0 %



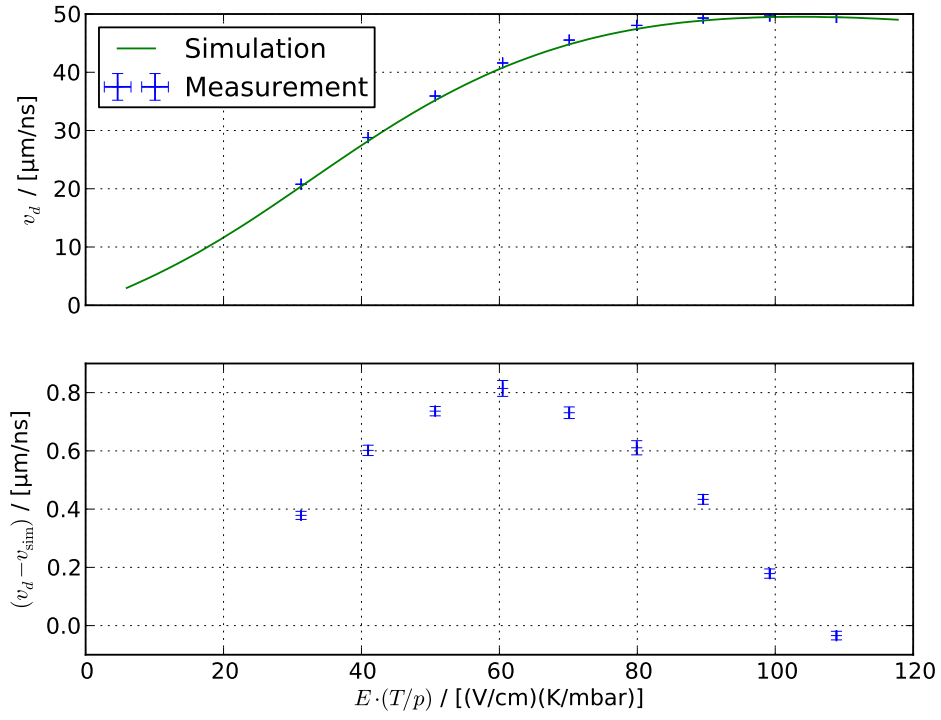
Ar 92 % – CH₄ 7 % – CO₂ 1 %



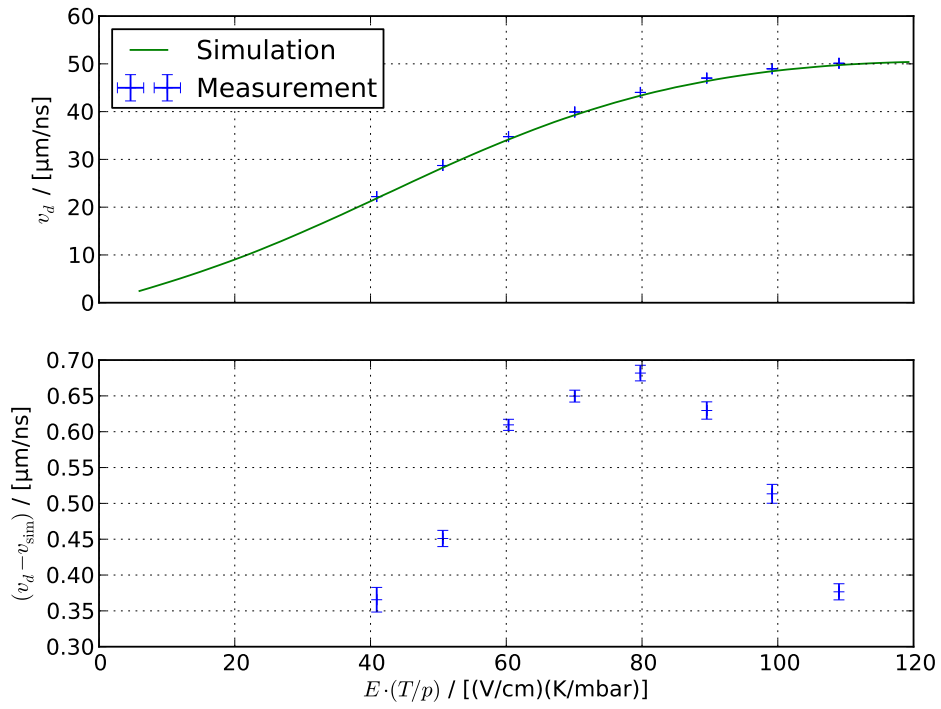
Ar 91 % – CH₄ 7 % – CO₂ 2 %



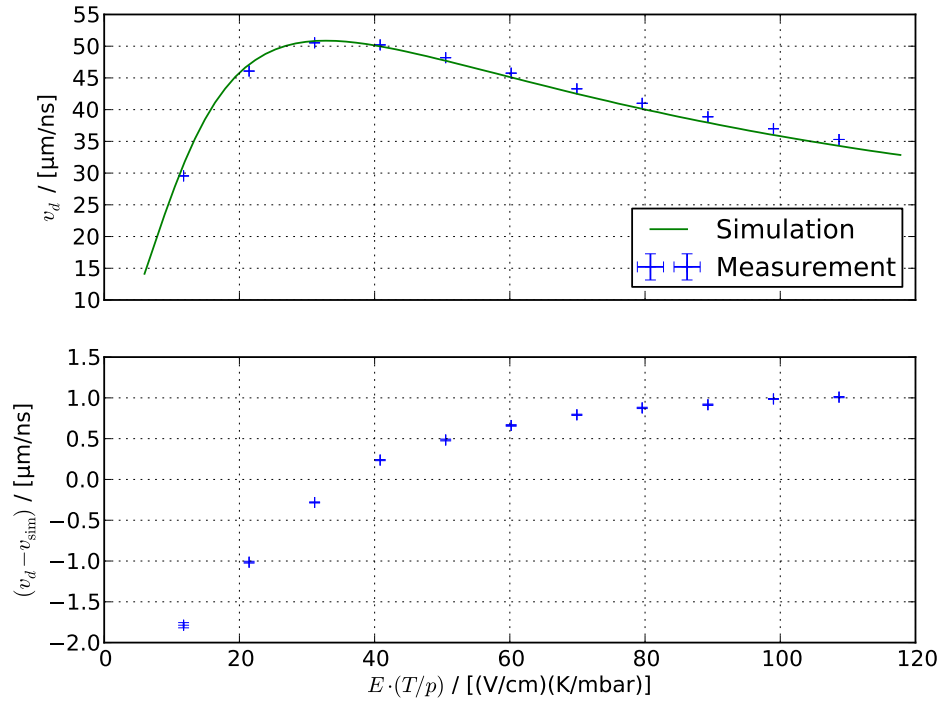
Ar 90 % – CH₄ 7 % – CO₂ 3 %



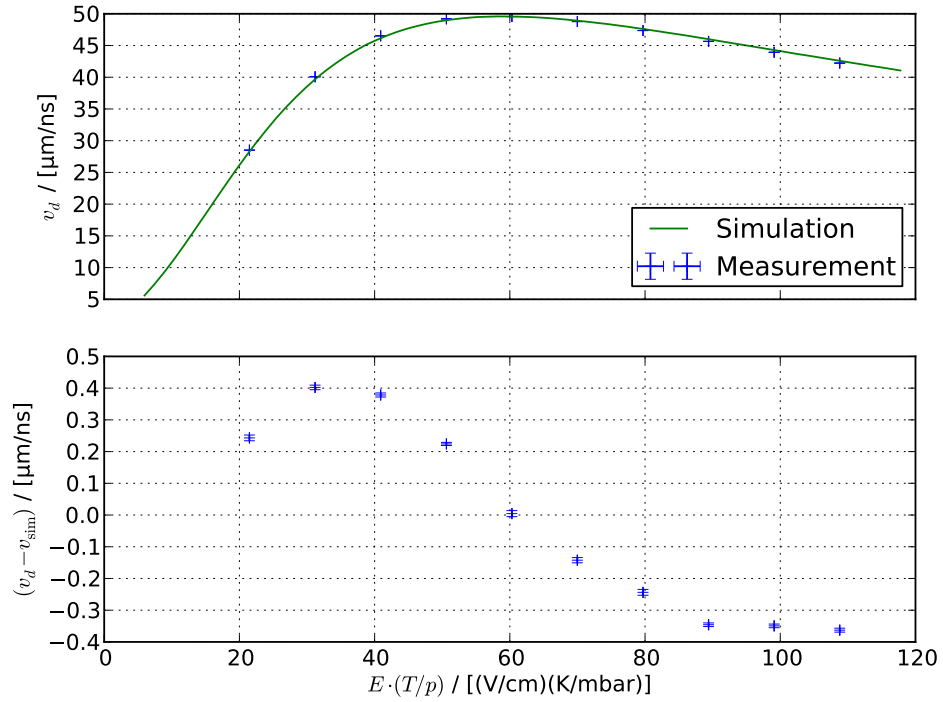
Ar 89 % – CH₄ 7 % – CO₂ 4 %



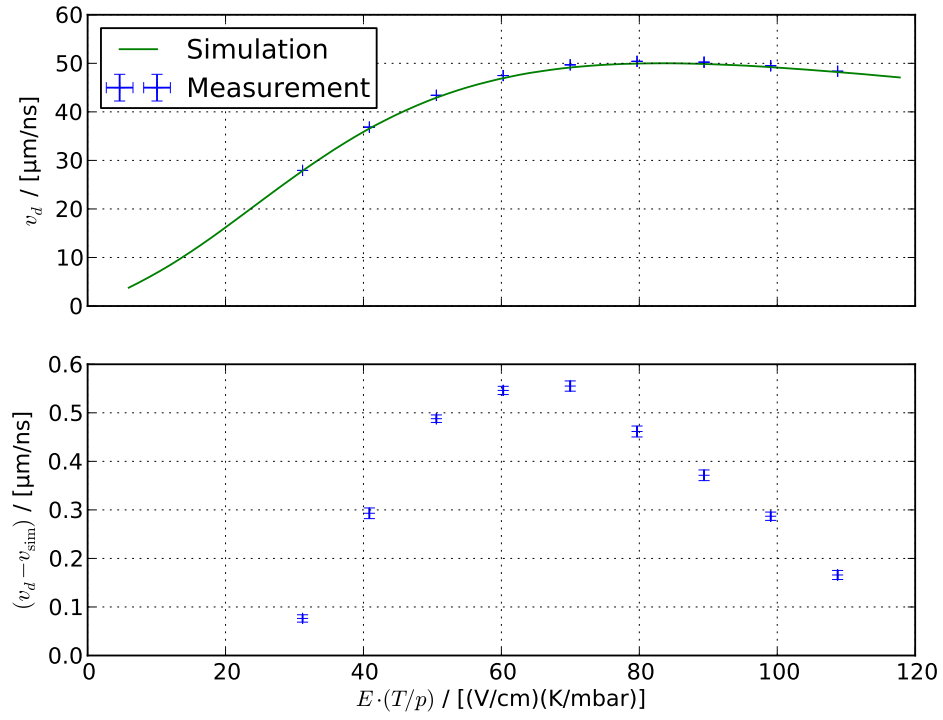
Ar 92 % – CH₄ 8 % – CO₂ 0 %



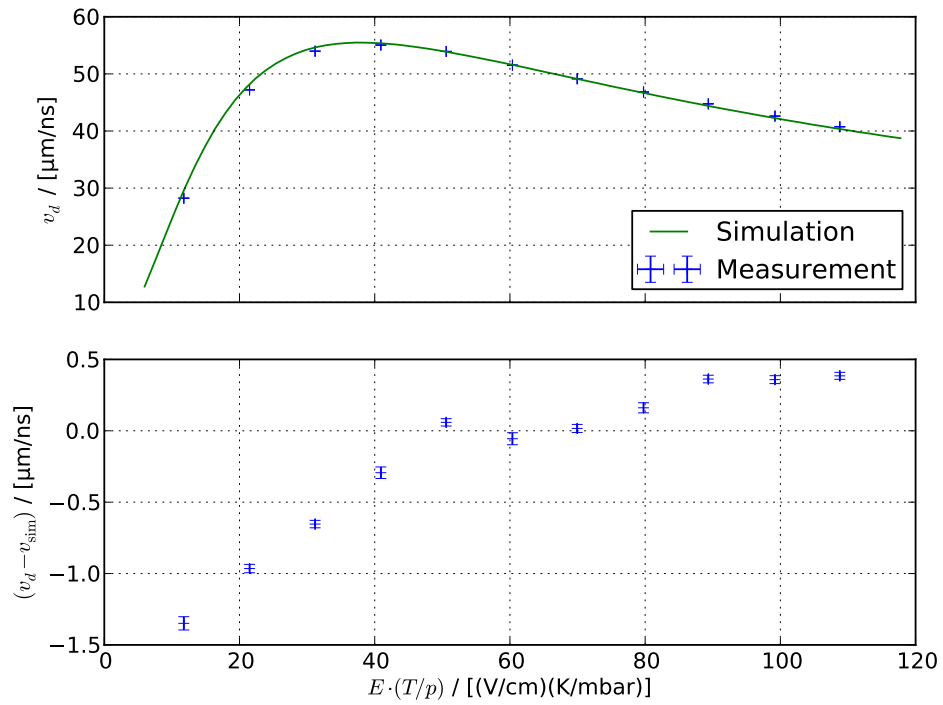
Ar 91 % – CH₄ 8 % – CO₂ 1 %



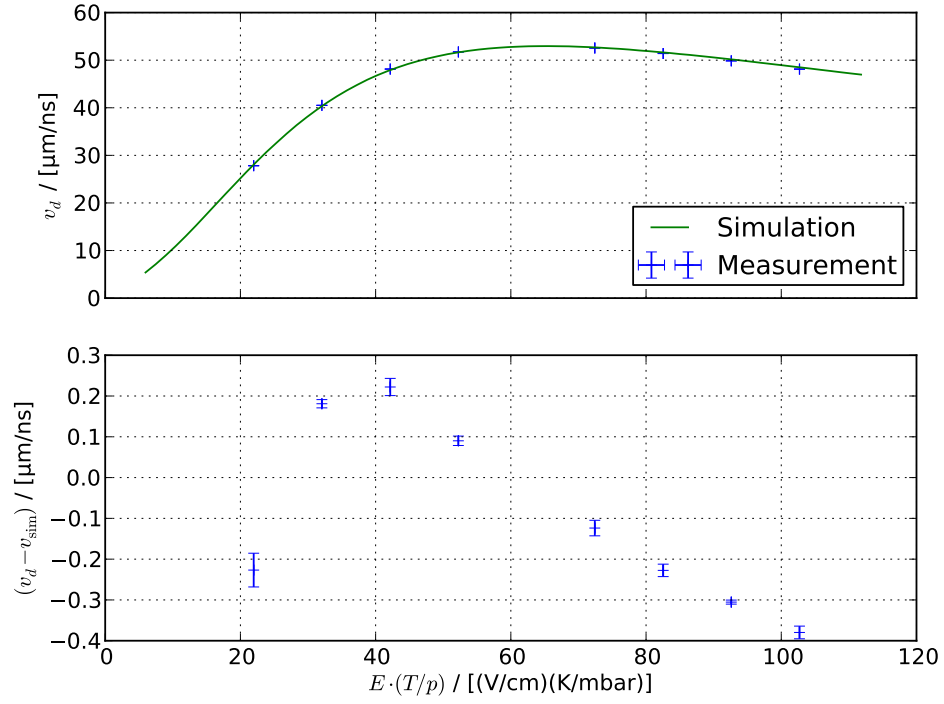
Ar 90 % – CH₄ 8 % – CO₂ 2 %



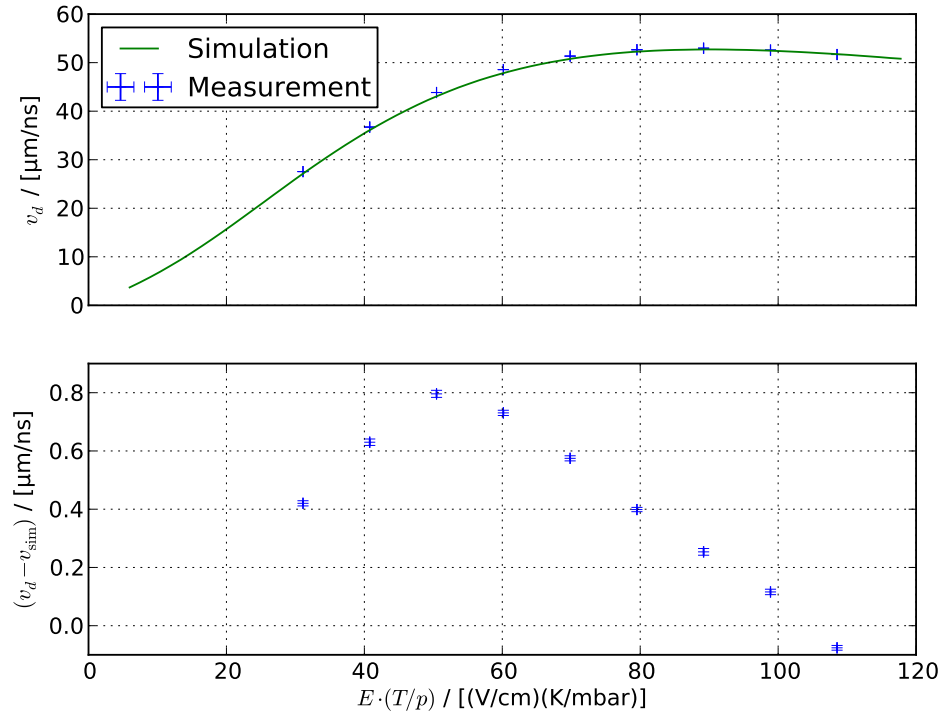
Ar 90 % – CH₄ 10 % – CO₂ 0 %

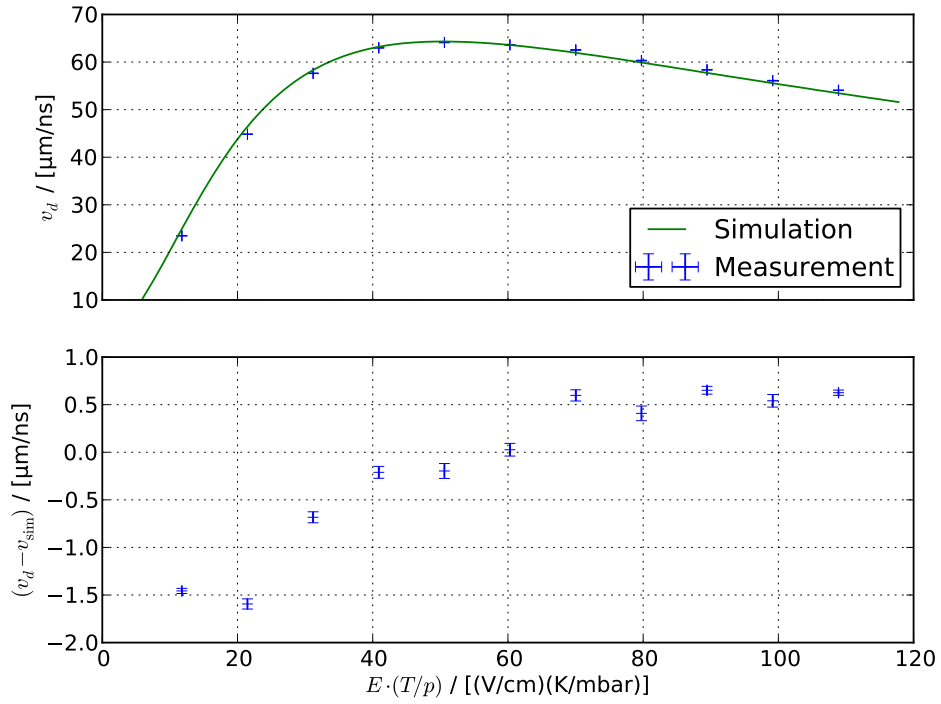
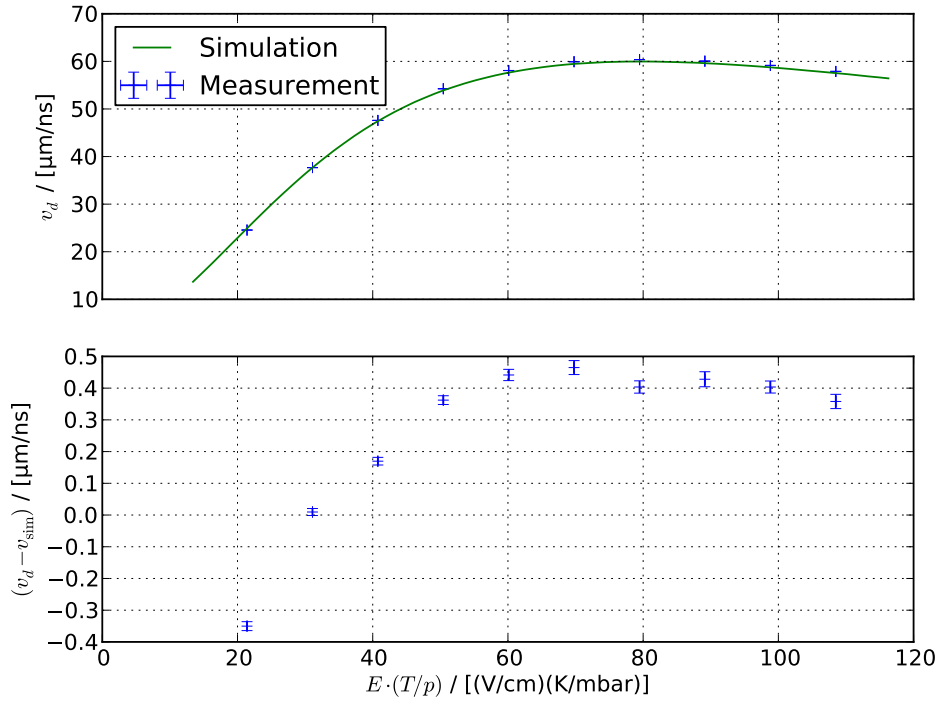


Ar 89 % – CH₄ 10 % – CO₂ 1 %

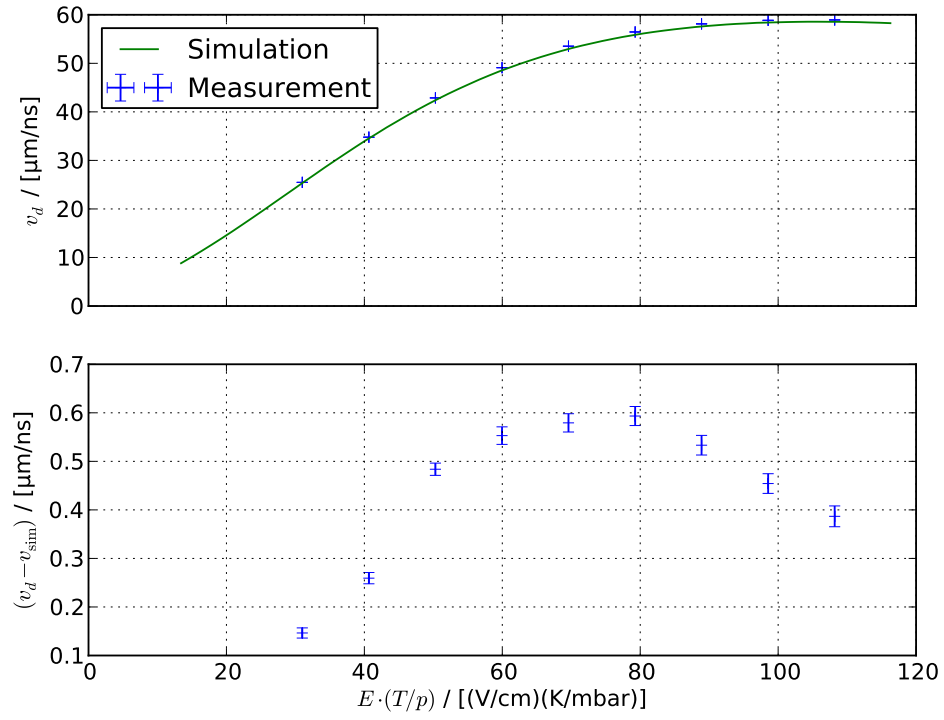


Ar 88 % – CH₄ 10 % – CO₂ 2 %

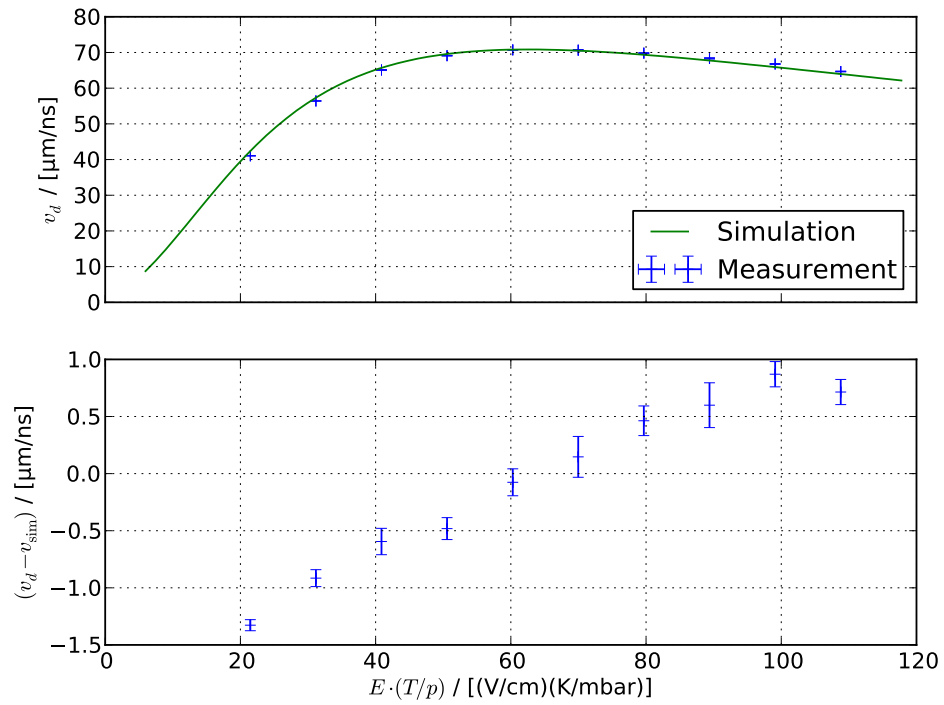


Ar 85 % – CH₄ 15 % – CO₂ 0 %Ar 84 % – CH₄ 15 % – CO₂ 1 %

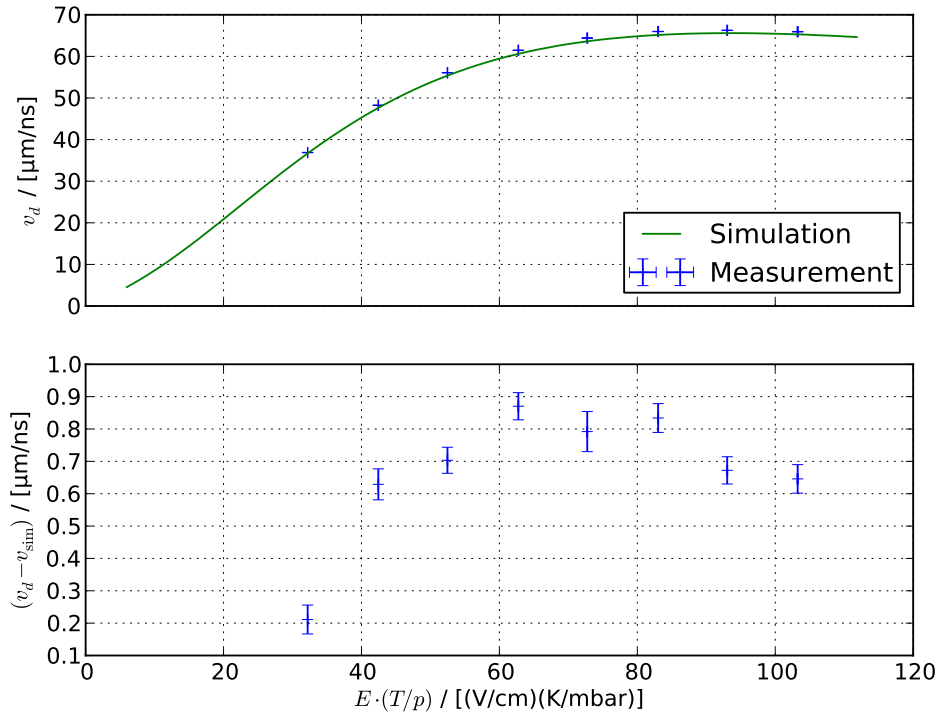
Ar 83 % – CH₄ 15 % – CO₂ 2 %



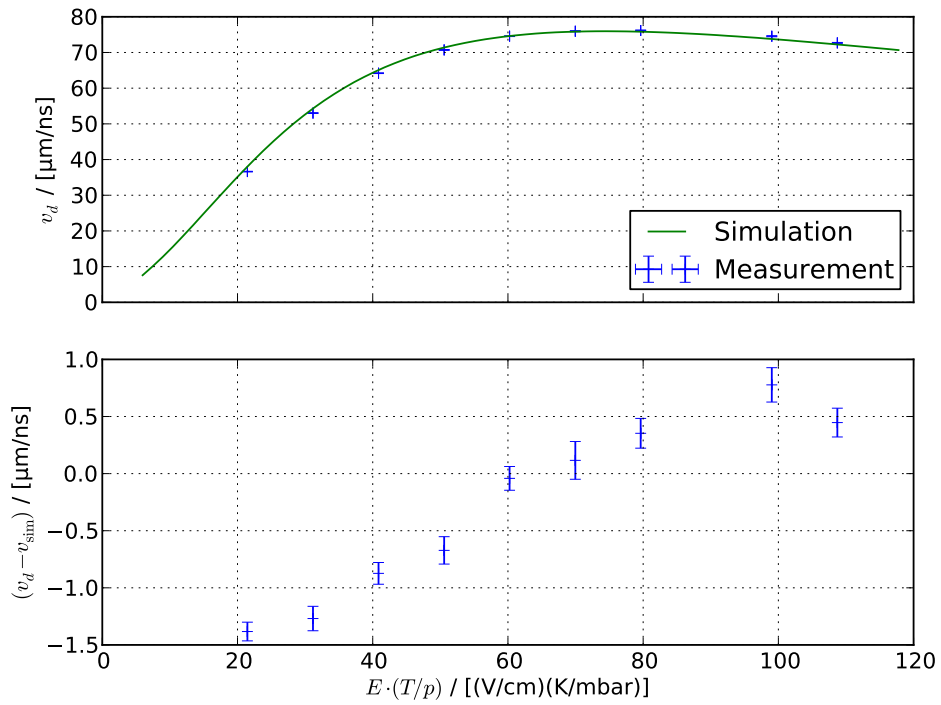
Ar 80 % – CH₄ 20 % – CO₂ 0 %



Ar 79 % – CH₄ 20 % – CO₂ 1 %

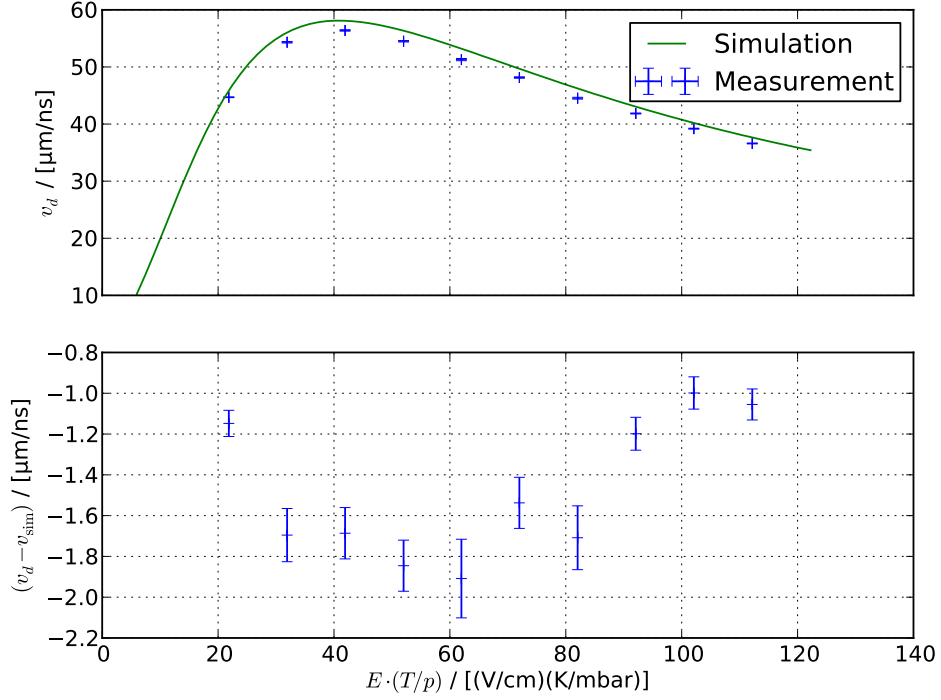


Ar 75 % – CH₄ 25 % – CO₂ 0 %

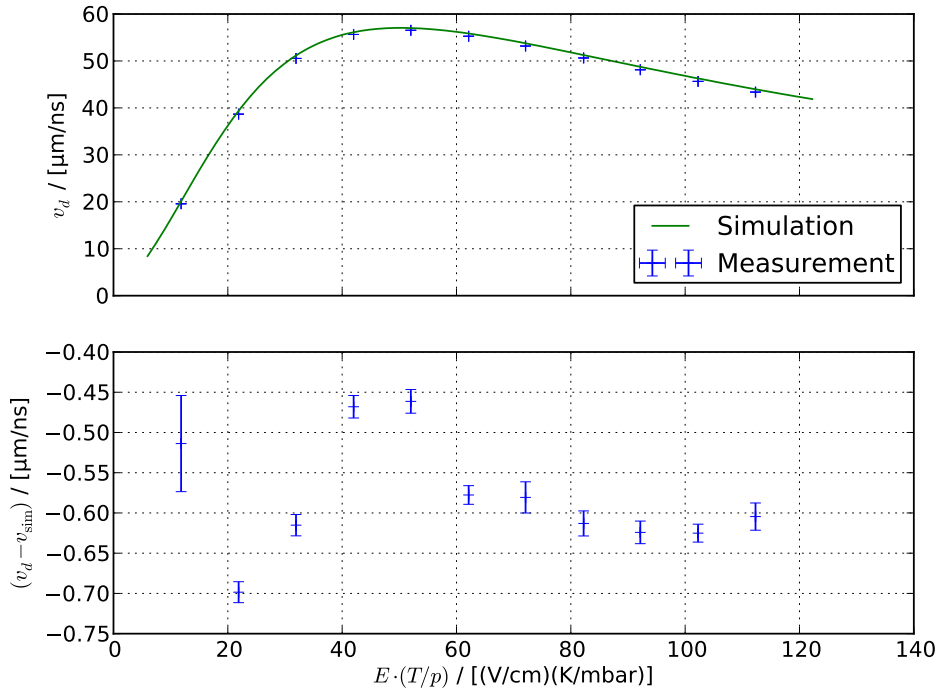


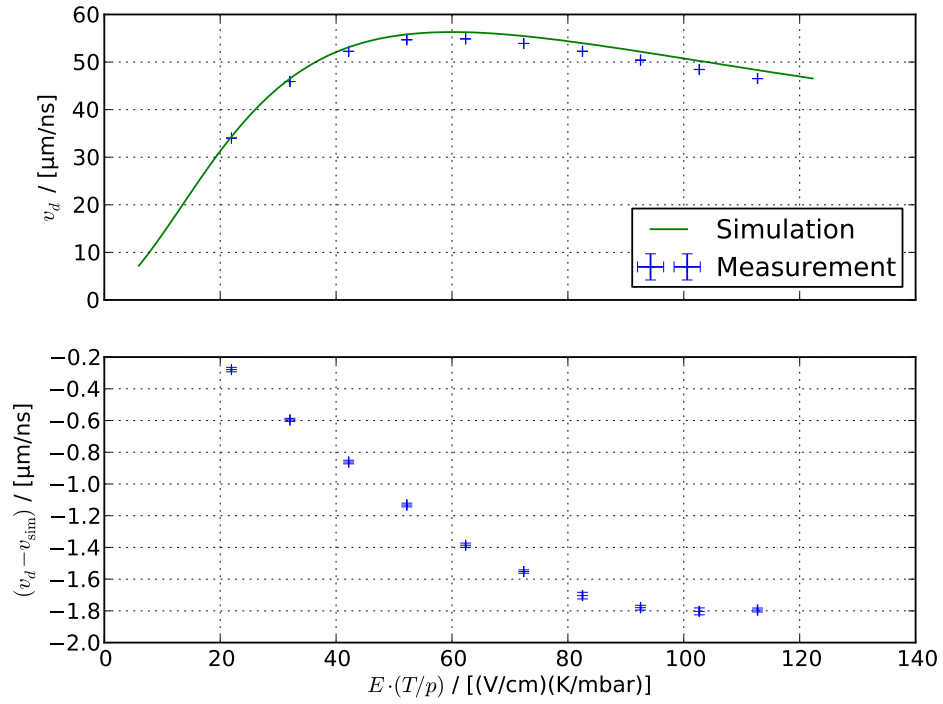
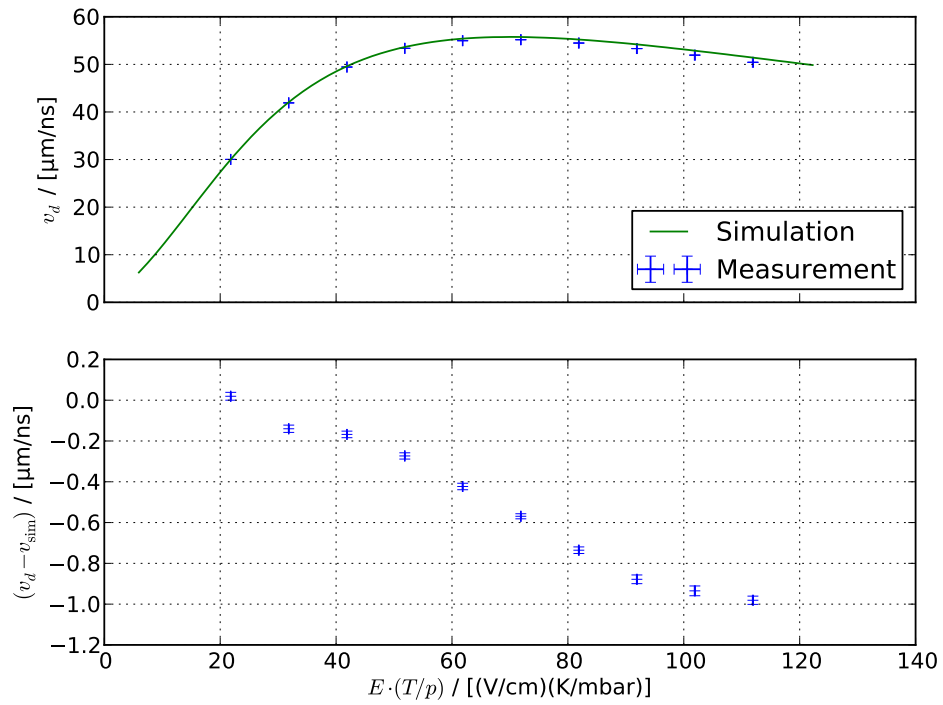
B.2. Ar-CF₄-iC₄H₁₀ mixtures

Ar 98 % – CF₄ 1 % – iC₄H₁₀ 1 %

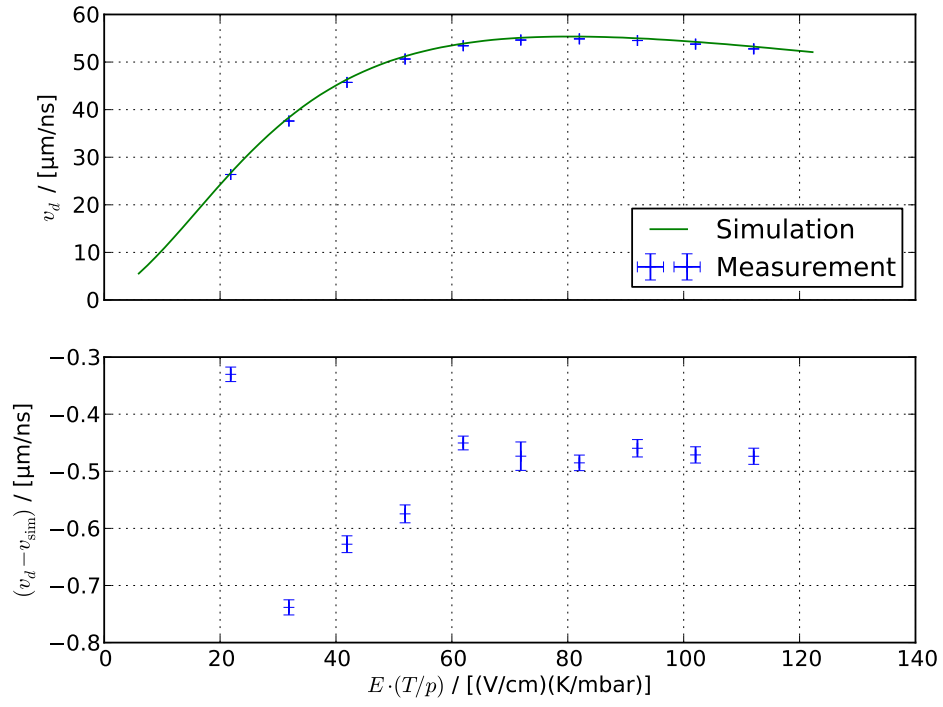


Ar 97 % – CF₄ 1 % – iC₄H₁₀ 2 %

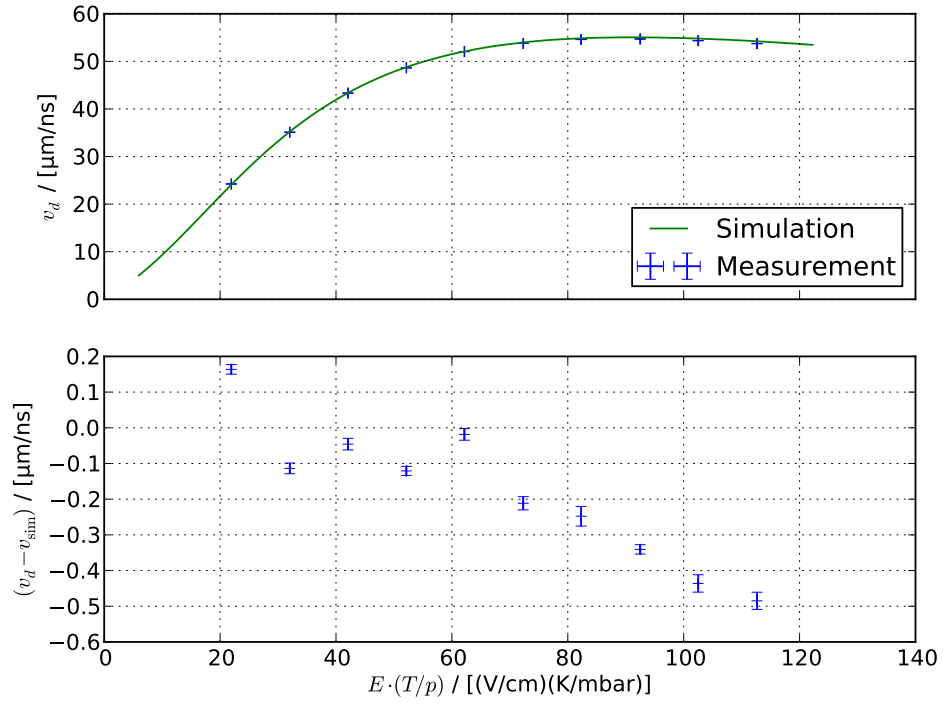


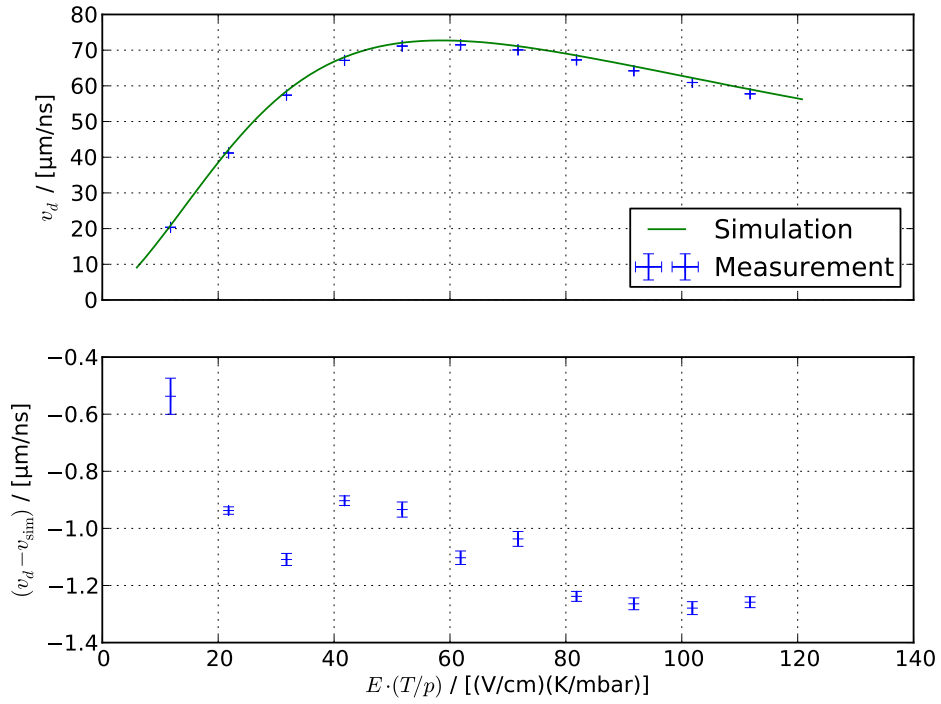
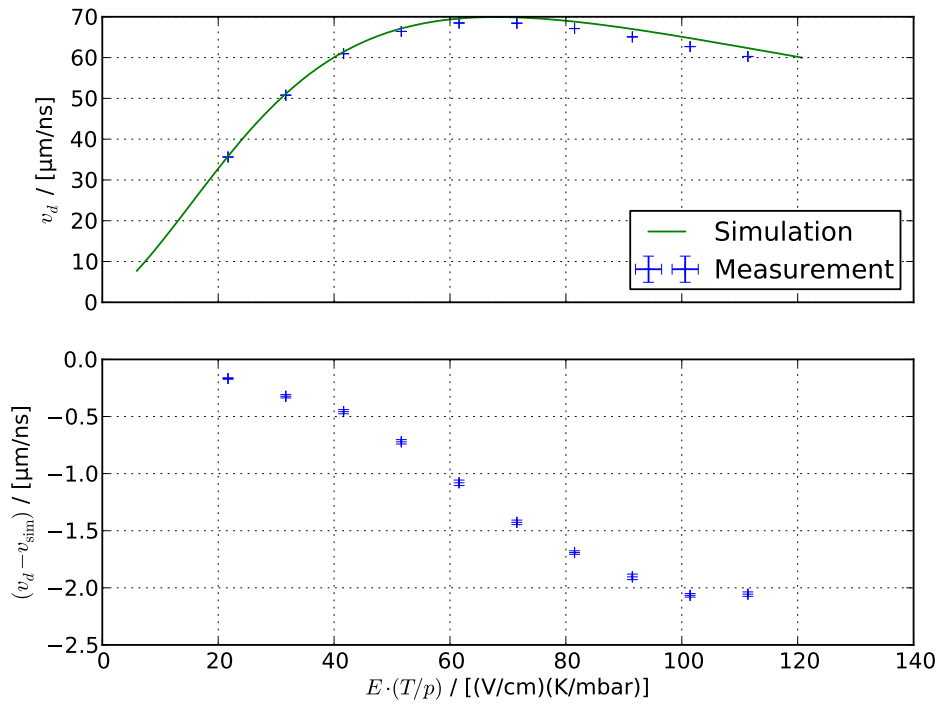
Ar 96 % – CF₄ 1 % – iC₄H₁₀ 3 %Ar 95 % – CF₄ 1 % – iC₄H₁₀ 4 %

Ar 94 % – CF₄ 1 % – iC₄H₁₀ 5 %

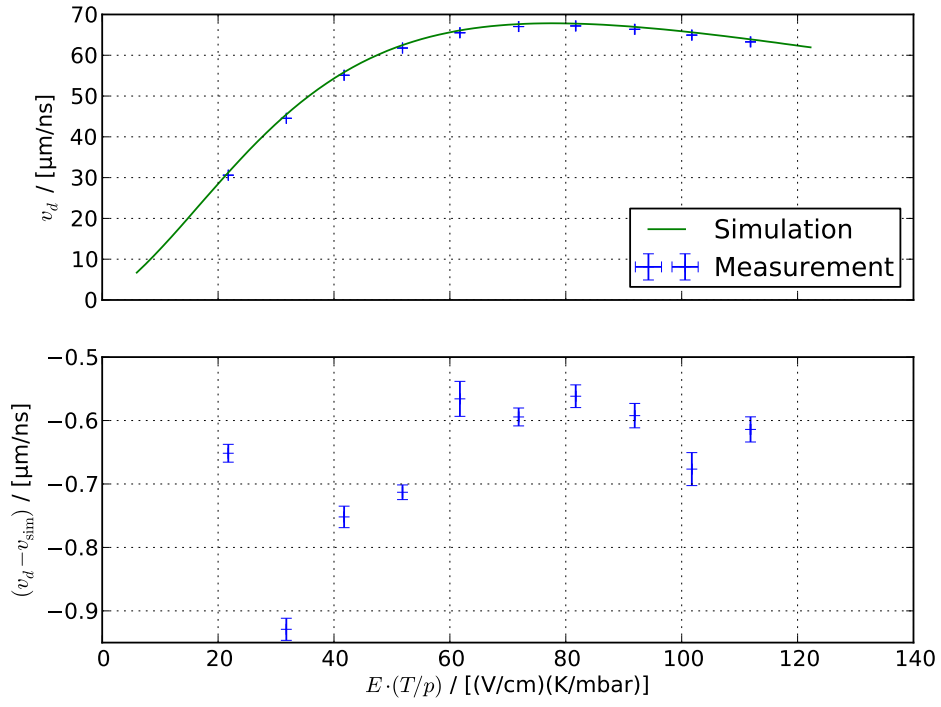


Ar 93 % – CF₄ 1 % – iC₄H₁₀ 6 %

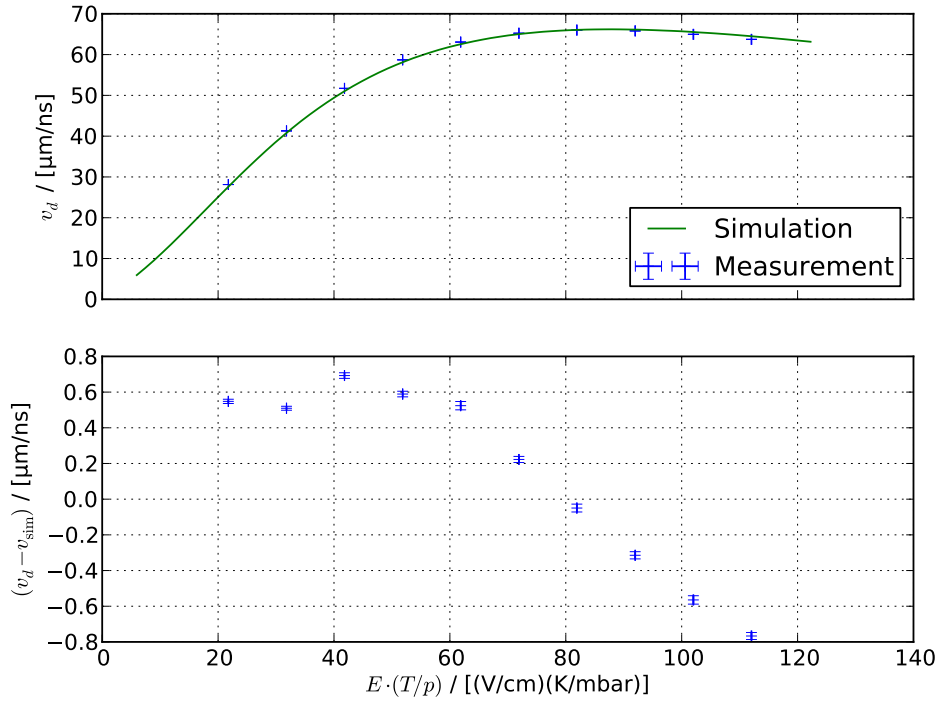


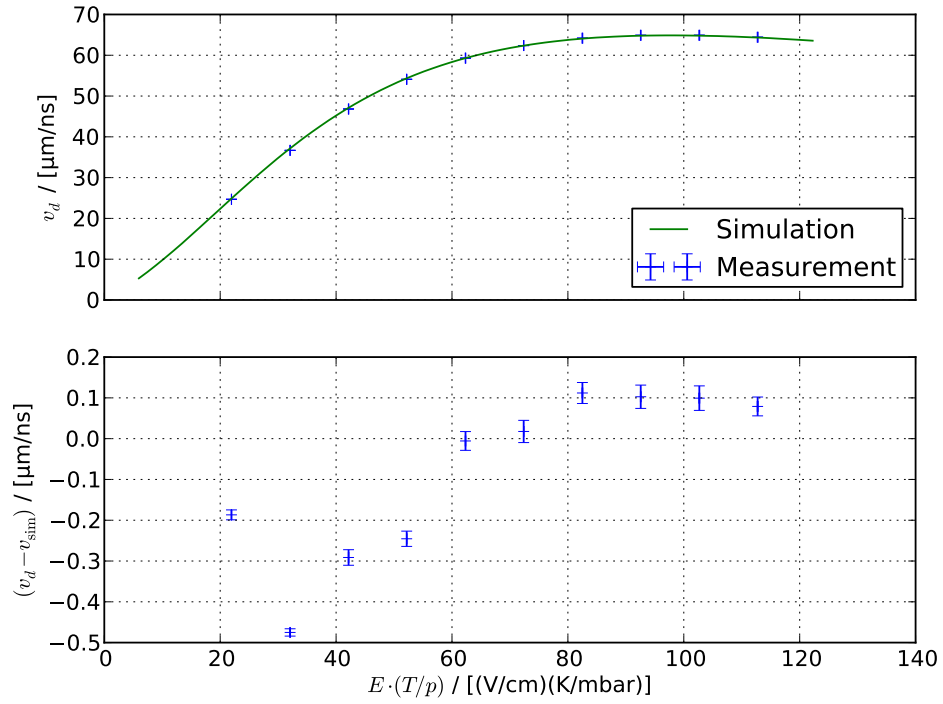
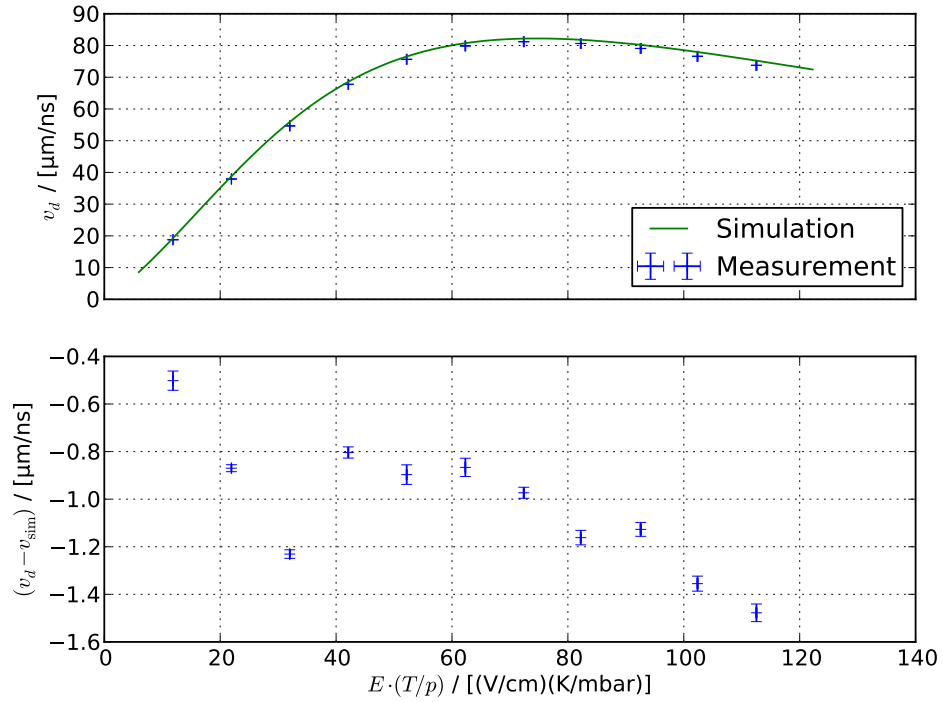
Ar 97 % – CF₄ 2 % – iC₄H₁₀ 1 %Ar 96 % – CF₄ 2 % – iC₄H₁₀ 2 %

Ar 95 % – CF₄ 2 % – iC₄H₁₀ 3 %

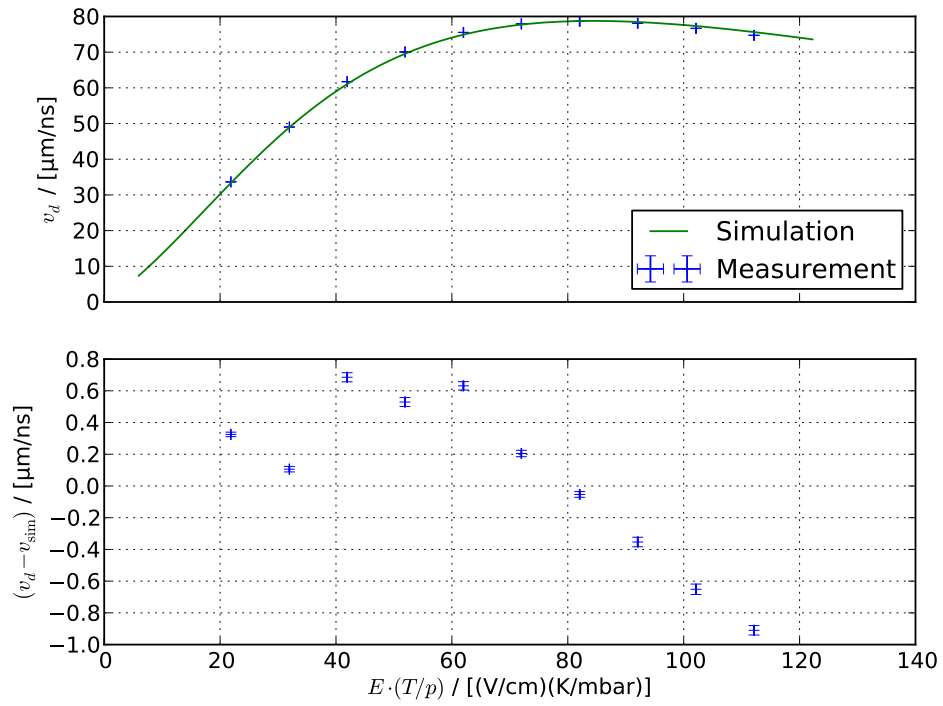


Ar 94 % – CF₄ 2 % – iC₄H₁₀ 4 %

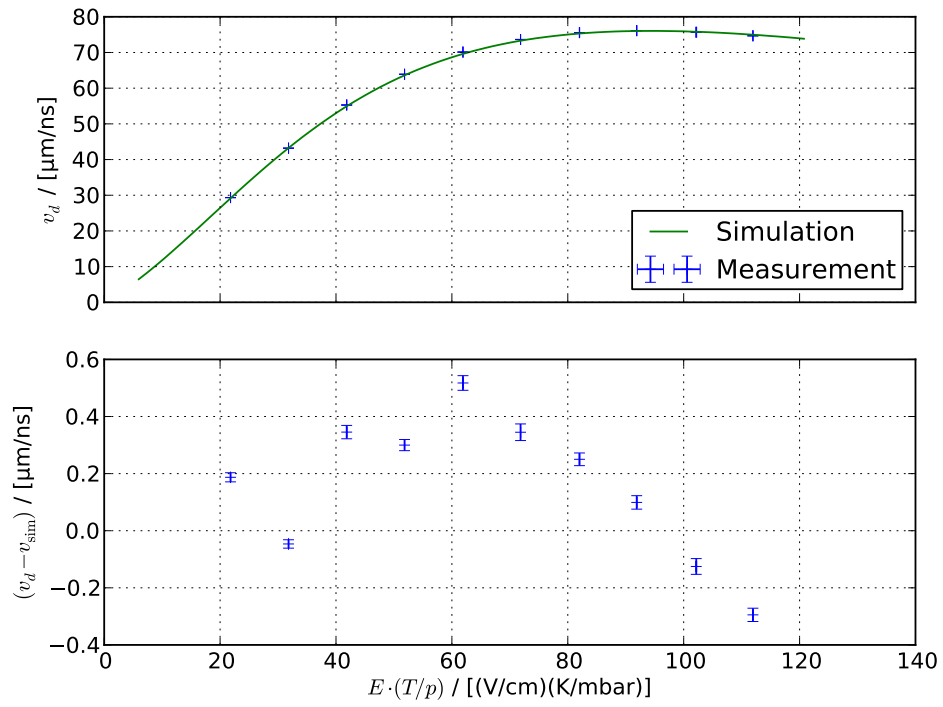


Ar 93 % – CF₄ 2 % – iC₄H₁₀ 5 %Ar 96 % – CF₄ 3 % – iC₄H₁₀ 1 %

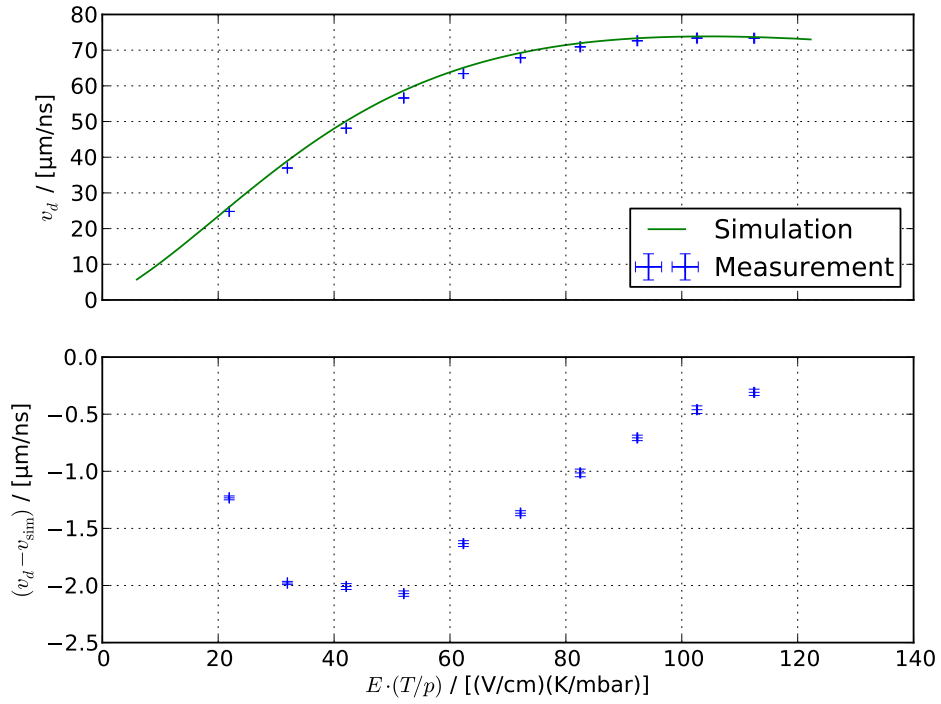
Ar 95 % – CF₄ 3 % – iC₄H₁₀ 2 %



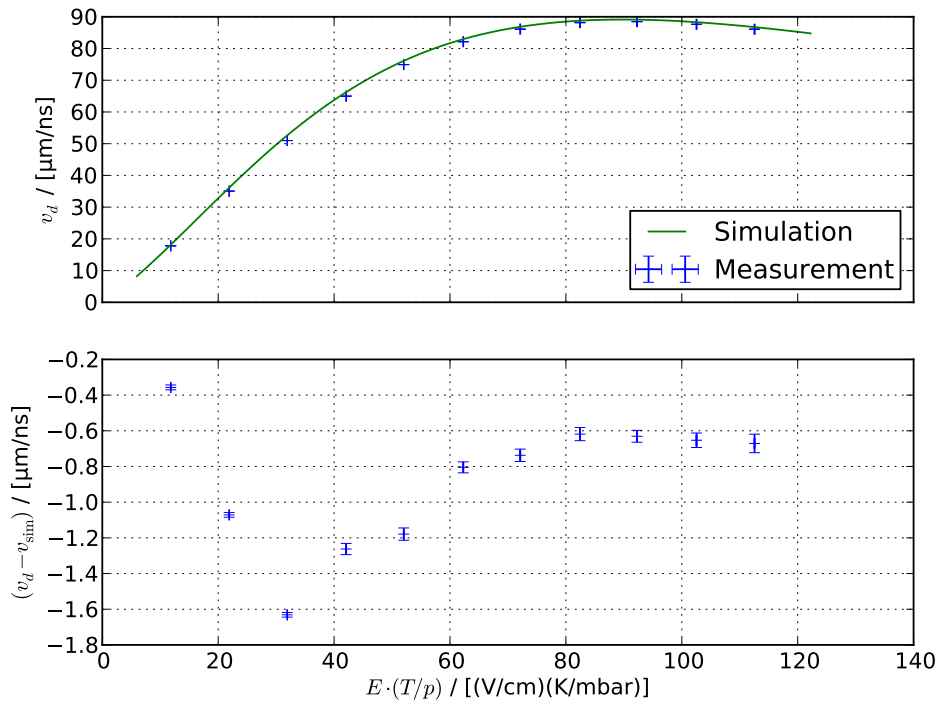
Ar 94 % – CF₄ 3 % – iC₄H₁₀ 3 %



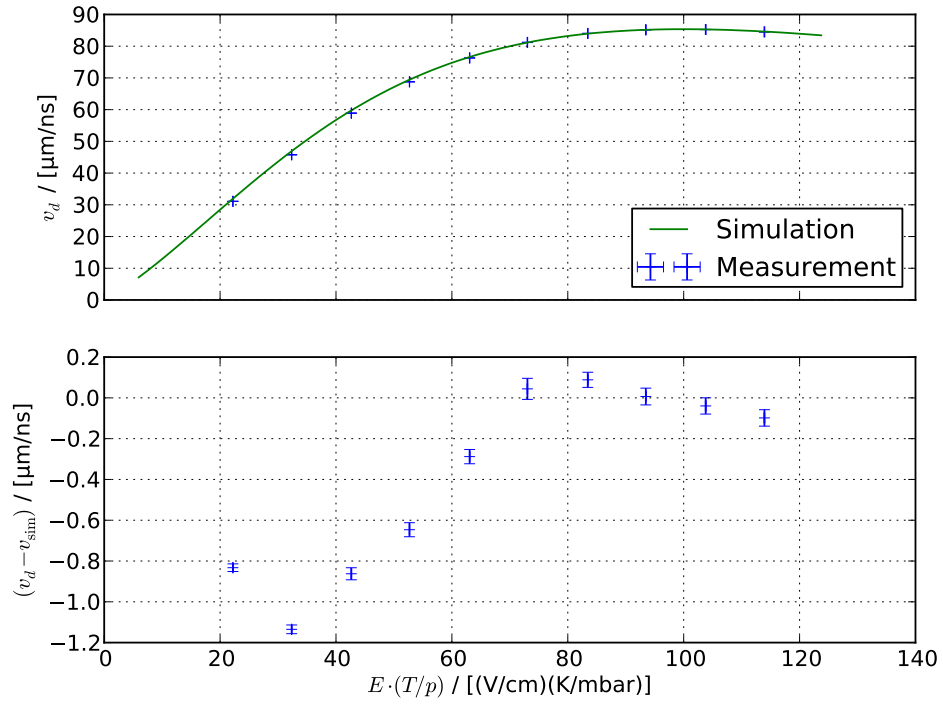
Ar 93 % – CF₄ 3 % – iC₄H₁₀ 4 %



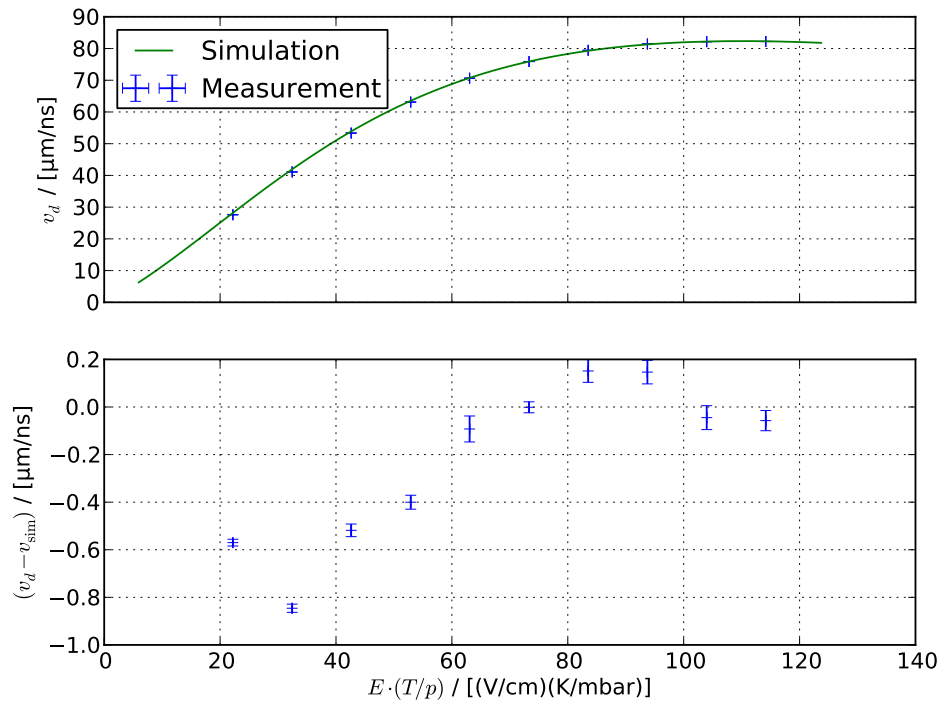
Ar 95 % – CF₄ 4 % – iC₄H₁₀ 1 %



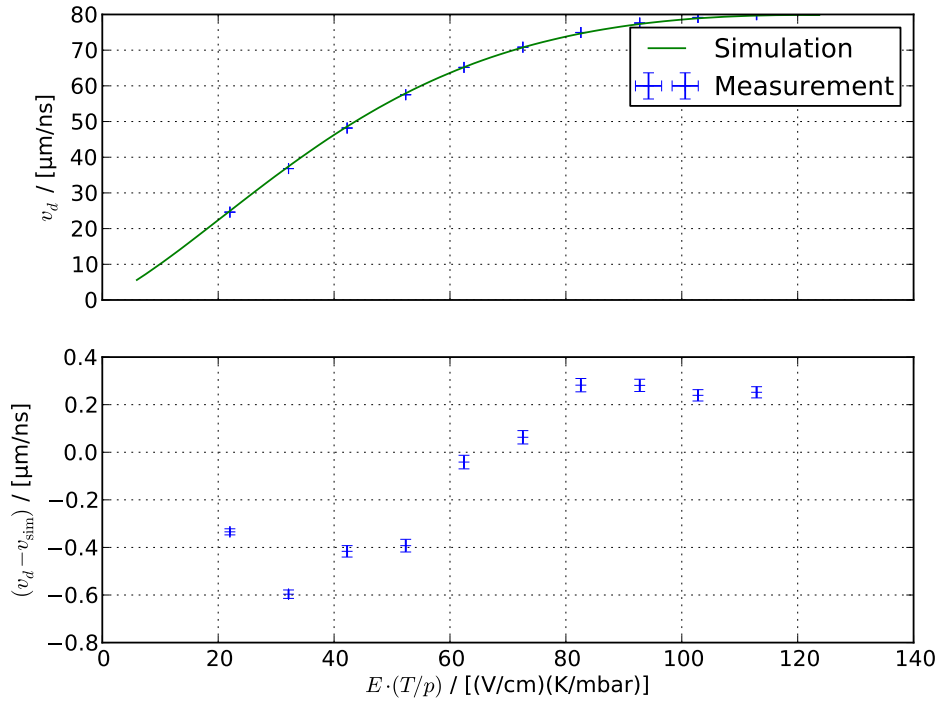
Ar 94 % – CF₄ 4 % – iC₄H₁₀ 2 %



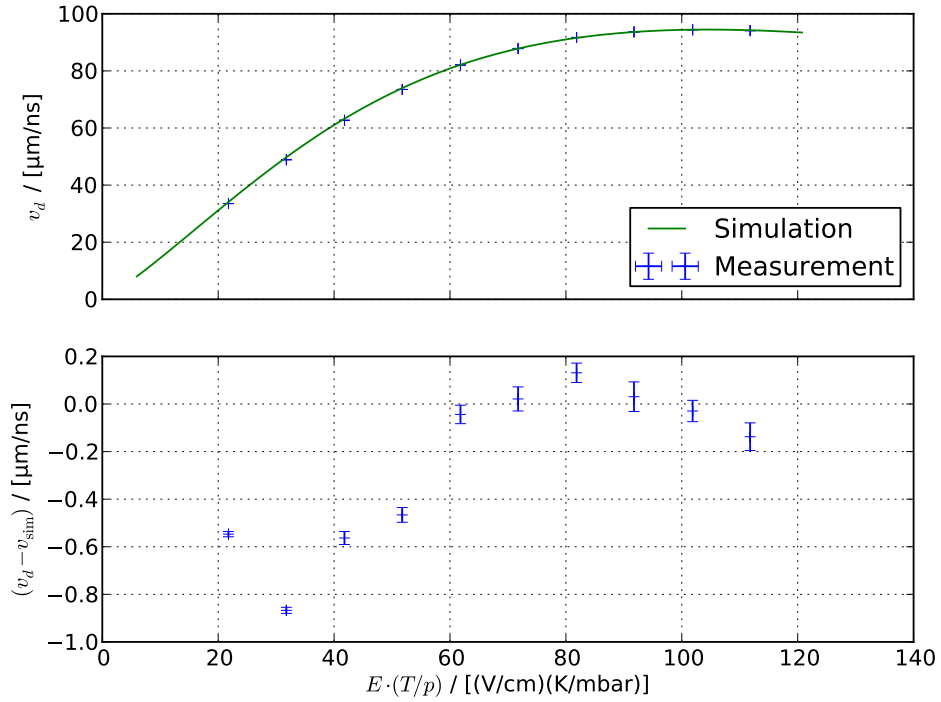
Ar 93 % – CF₄ 4 % – iC₄H₁₀ 3 %



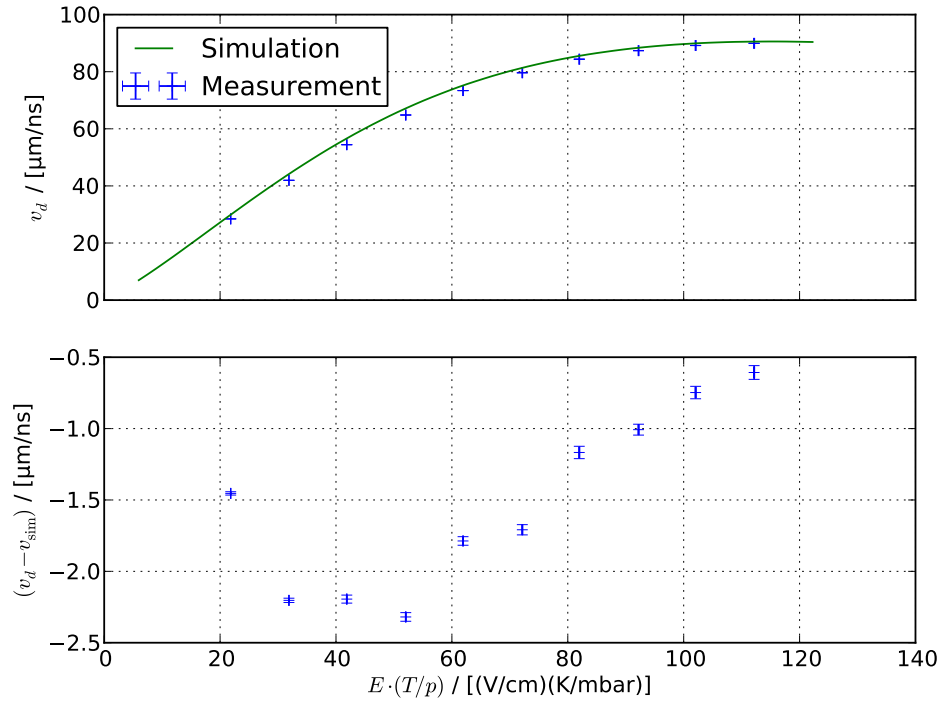
Ar 92 % – CF₄ 4 % – iC₄H₁₀ 4 %



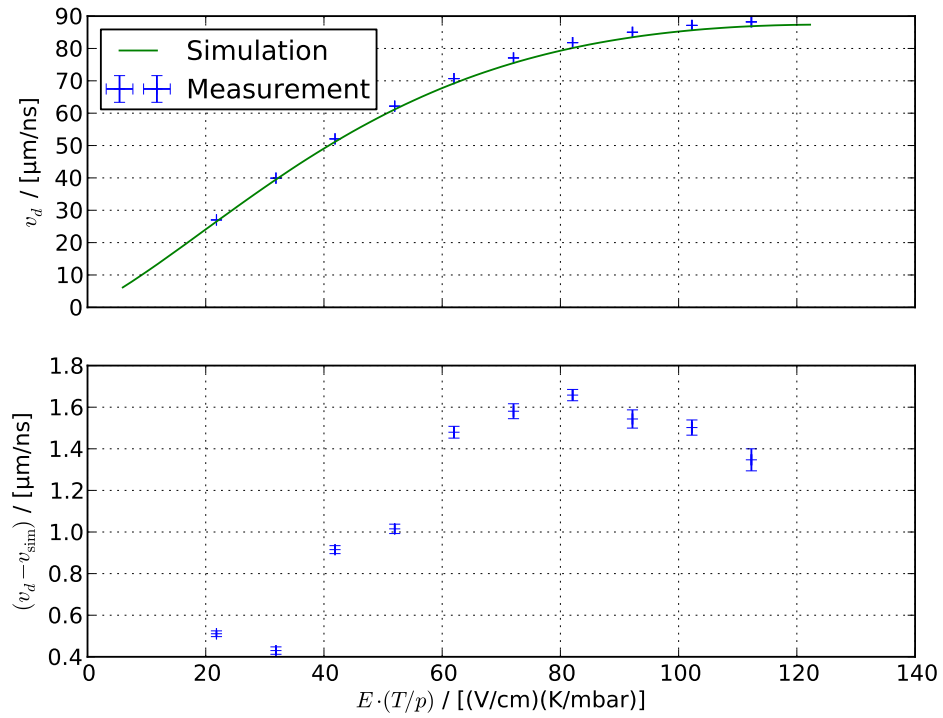
Ar 94 % – CF₄ 5 % – iC₄H₁₀ 1 %

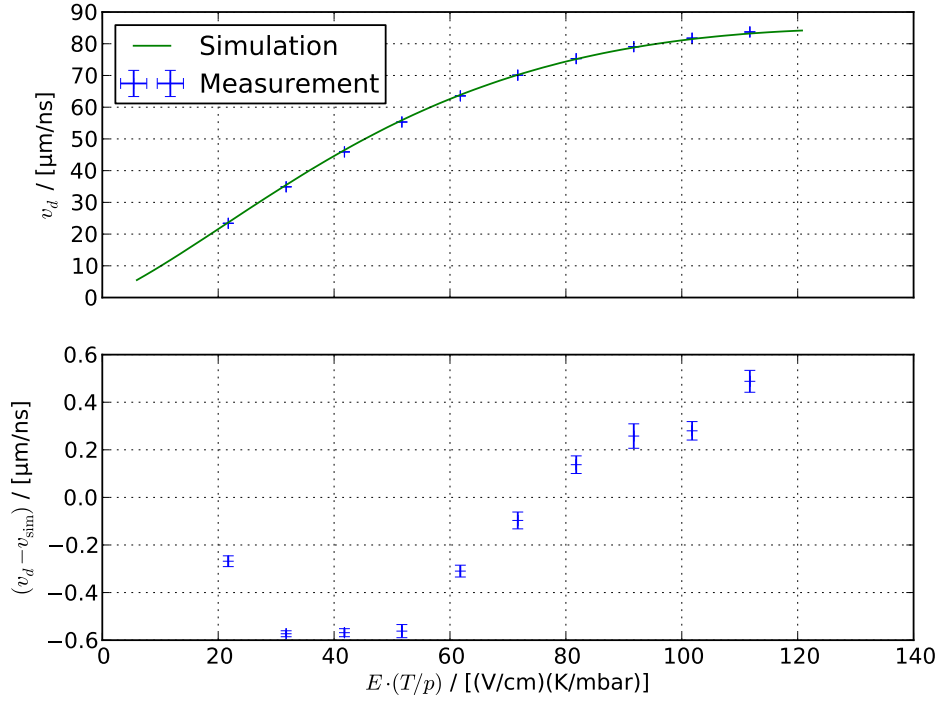


Ar 93 % – CF₄ 5 % – iC₄H₁₀ 2 %

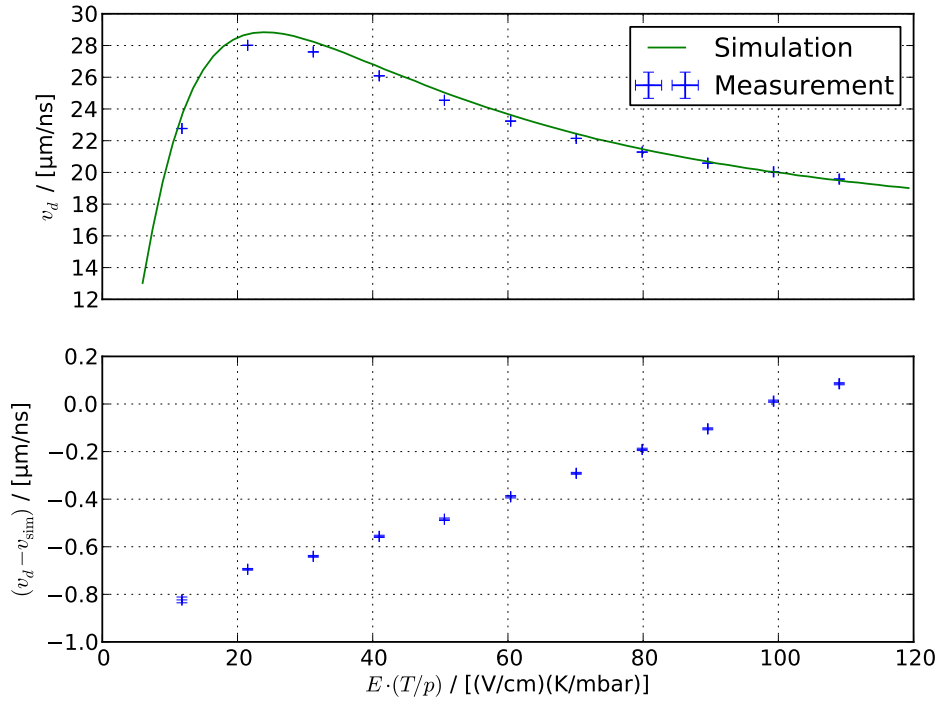


Ar 92 % – CF₄ 5 % – iC₄H₁₀ 3 %

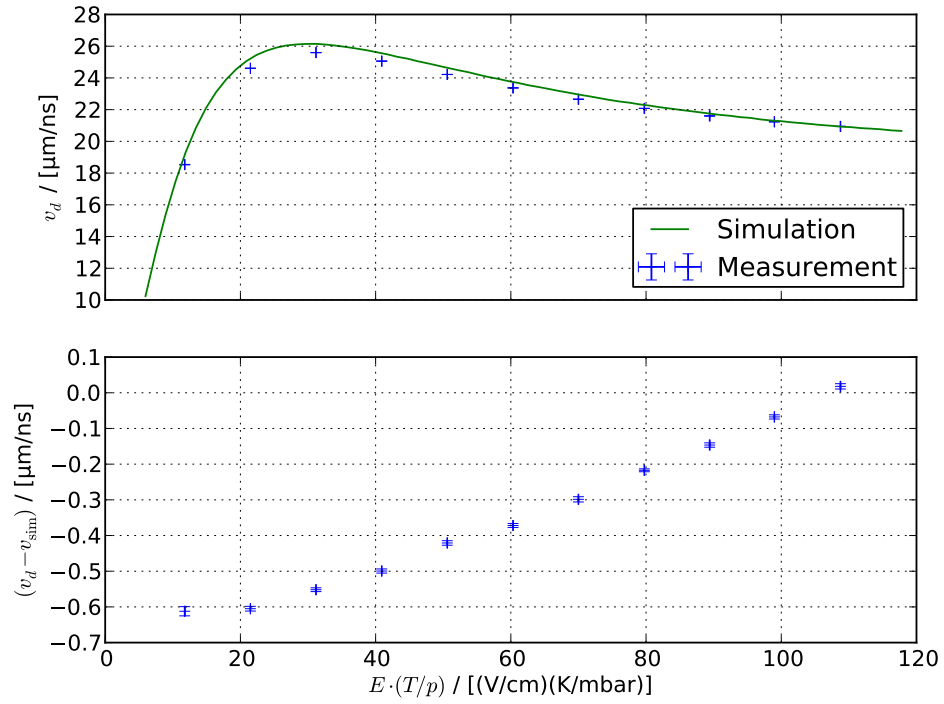


Ar 91 % – CF₄ 5 % – iC₄H₁₀ 4 %

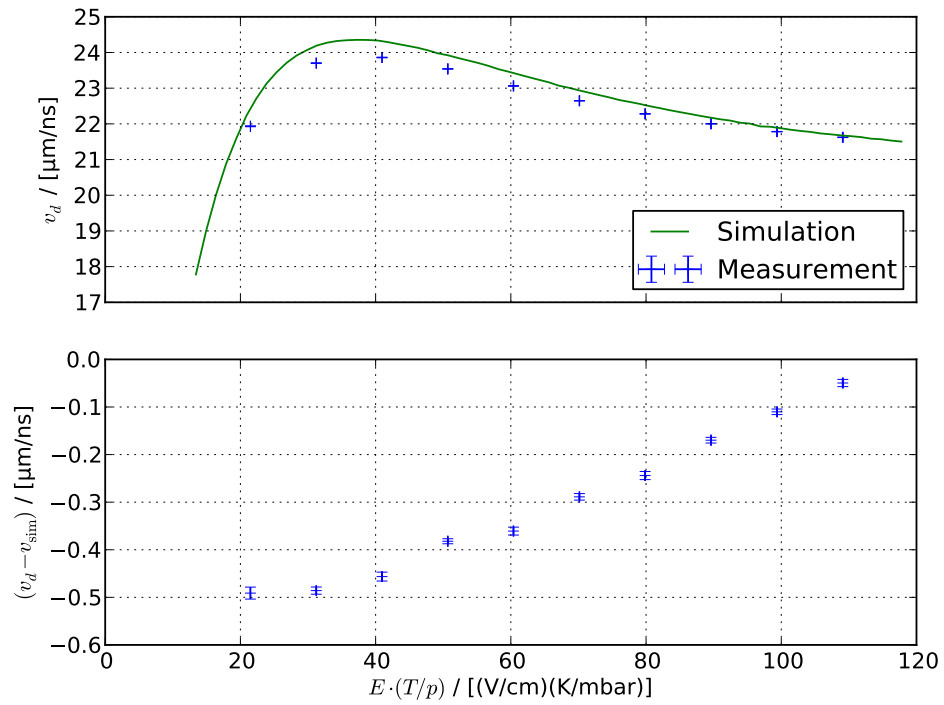
B.3. Ar-CH₄-H₂ mixtures

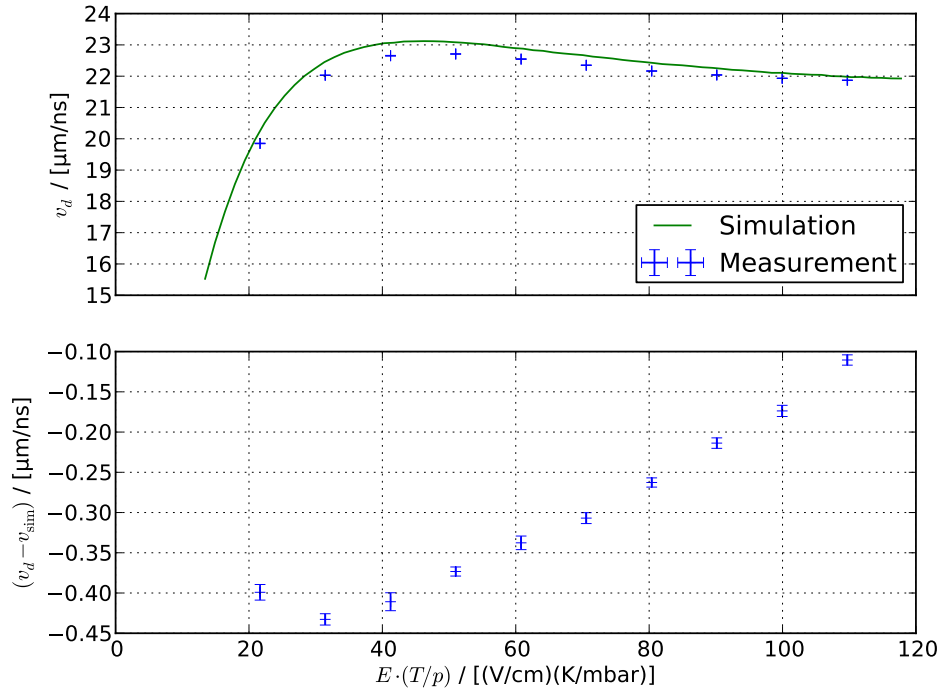
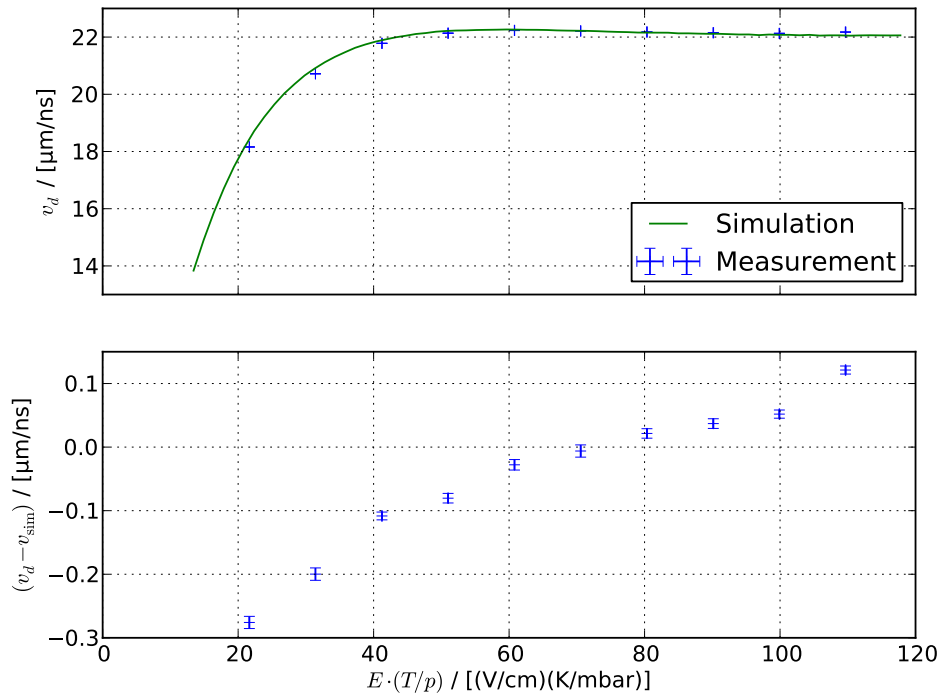
Ar 96 % – CH₄ 3 % – H₂ 1 %

Ar 95 % – CH₄ 3 % – H₂ 2 %

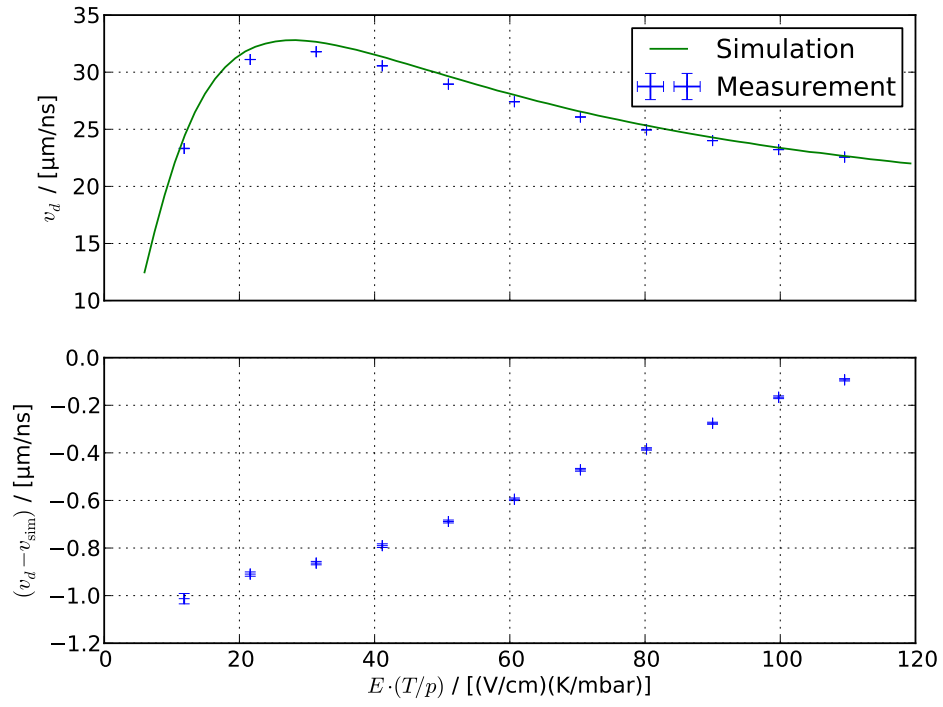


Ar 94 % – CH₄ 3 % – H₂ 3 %

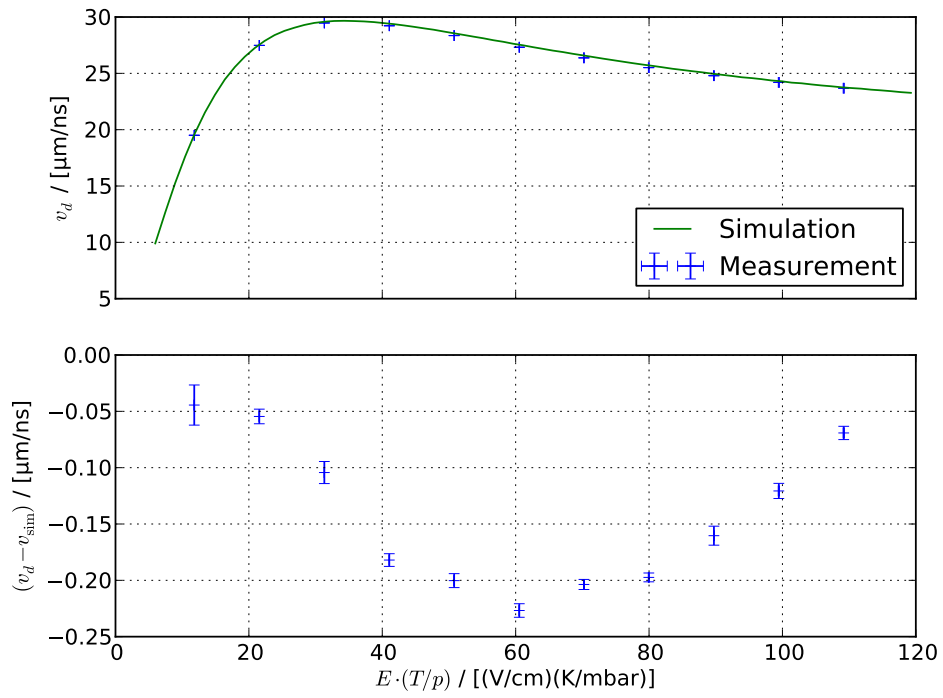


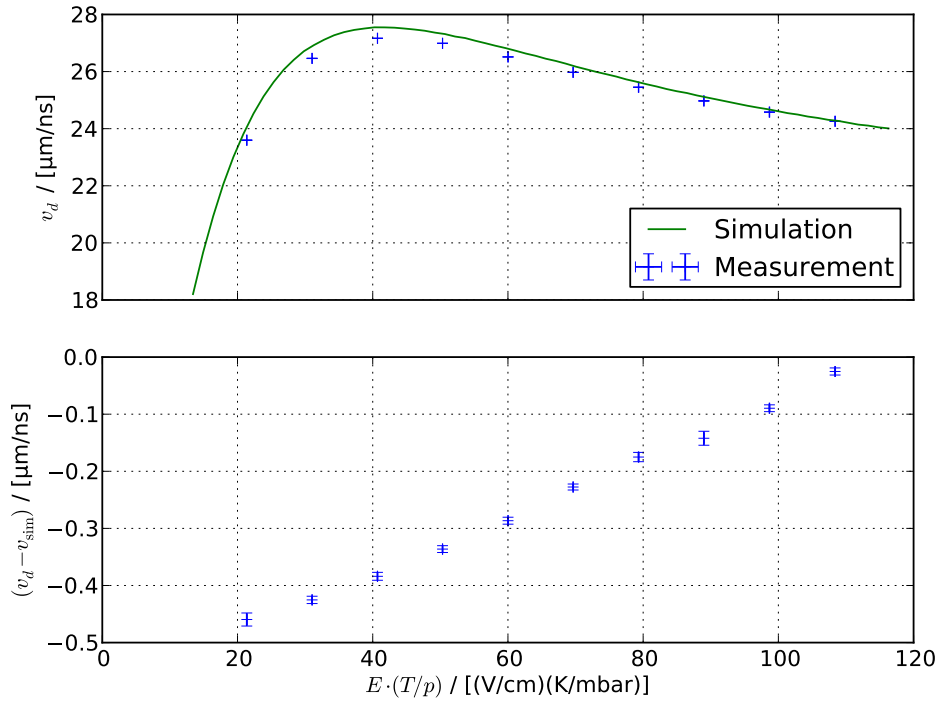
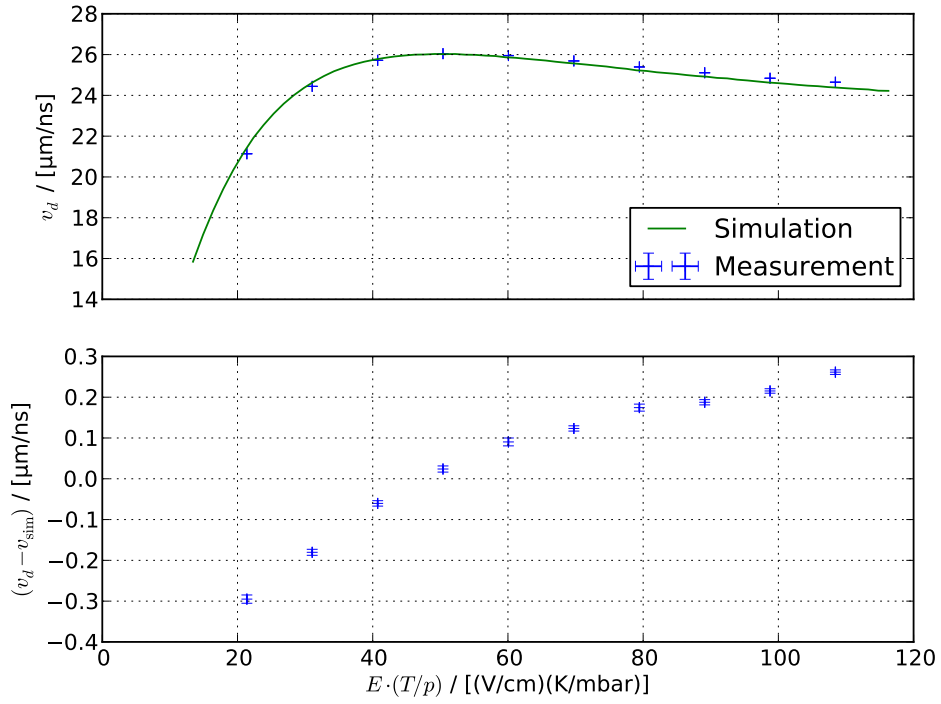
Ar 93 % – CH₄ 3 % – H₂ 4 %Ar 92 % – CH₄ 3 % – H₂ 5 %

Ar 95 % – CH₄ 4 % – H₂ 1 %

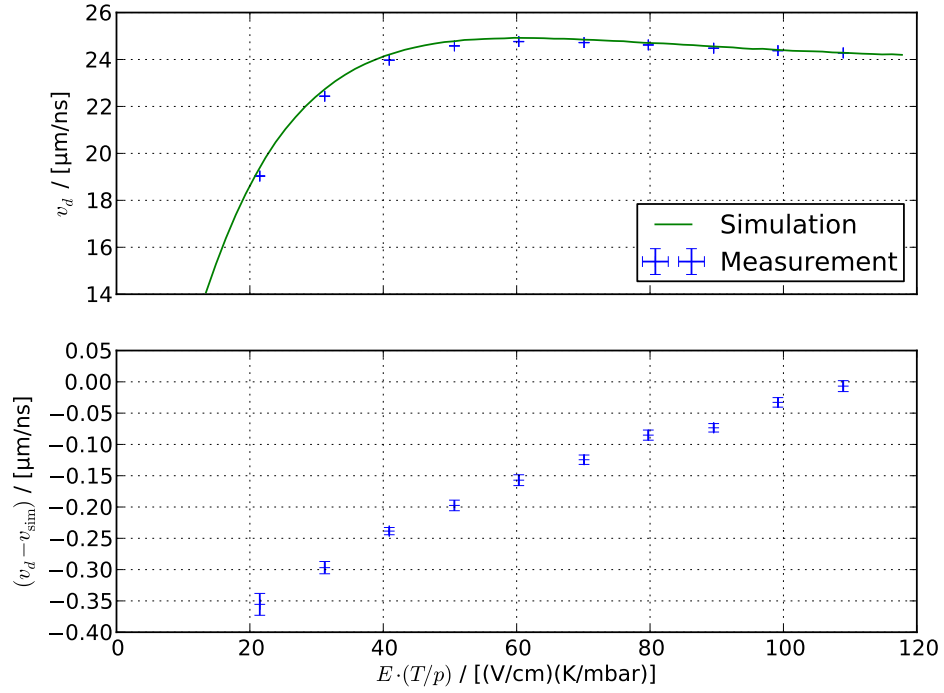


Ar 94 % – CH₄ 4 % – H₂ 2 %

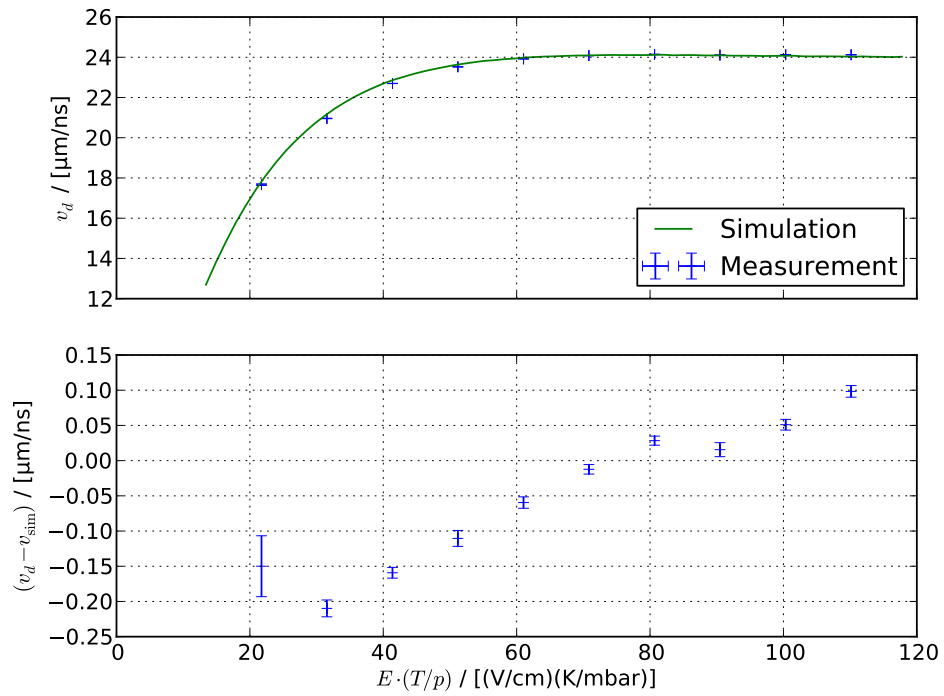


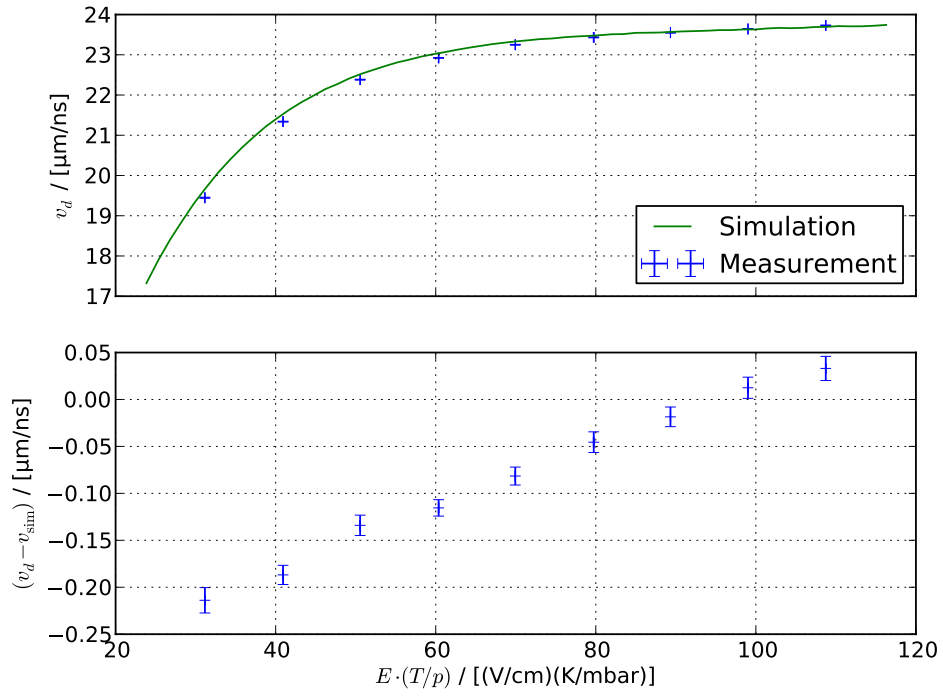
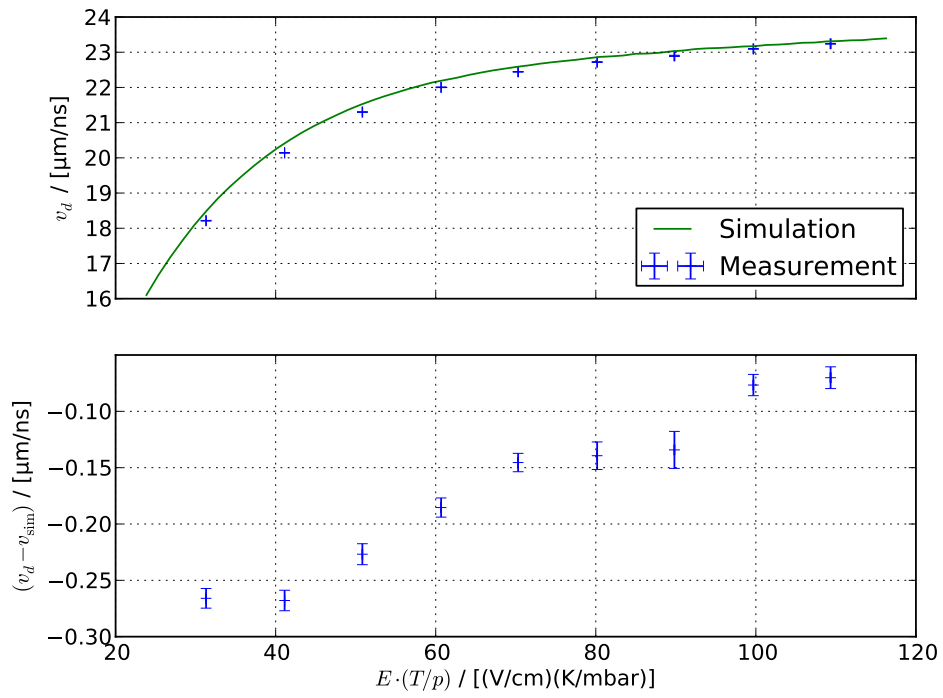
Ar 93 % – CH₄ 4 % – H₂ 3 %Ar 92 % – CH₄ 4 % – H₂ 4 %

Ar 91 % – CH₄ 4 % – H₂ 5 %

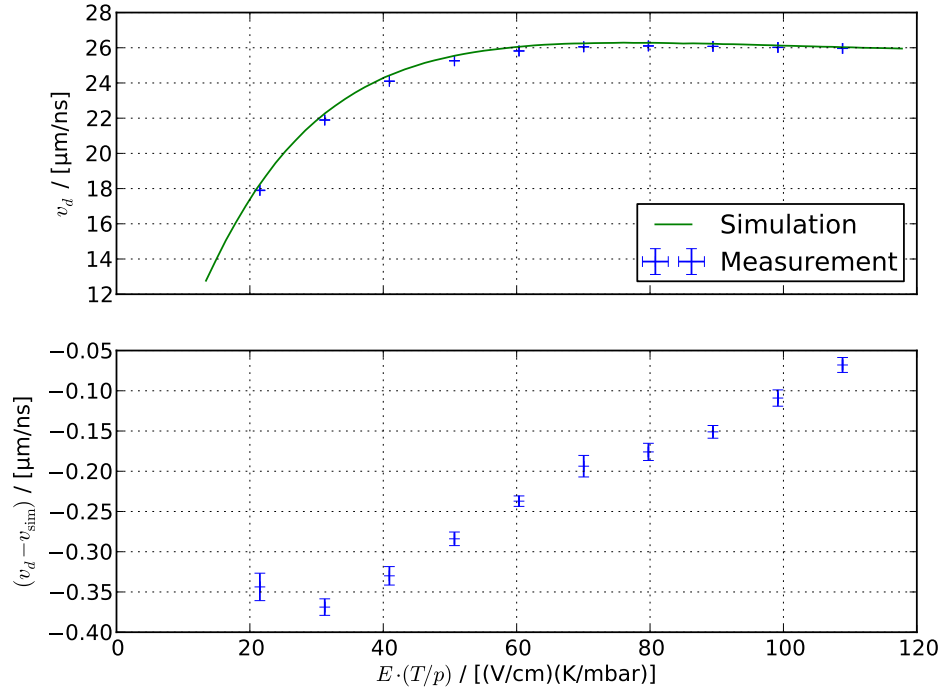


Ar 90 % – CH₄ 4 % – H₂ 6 %

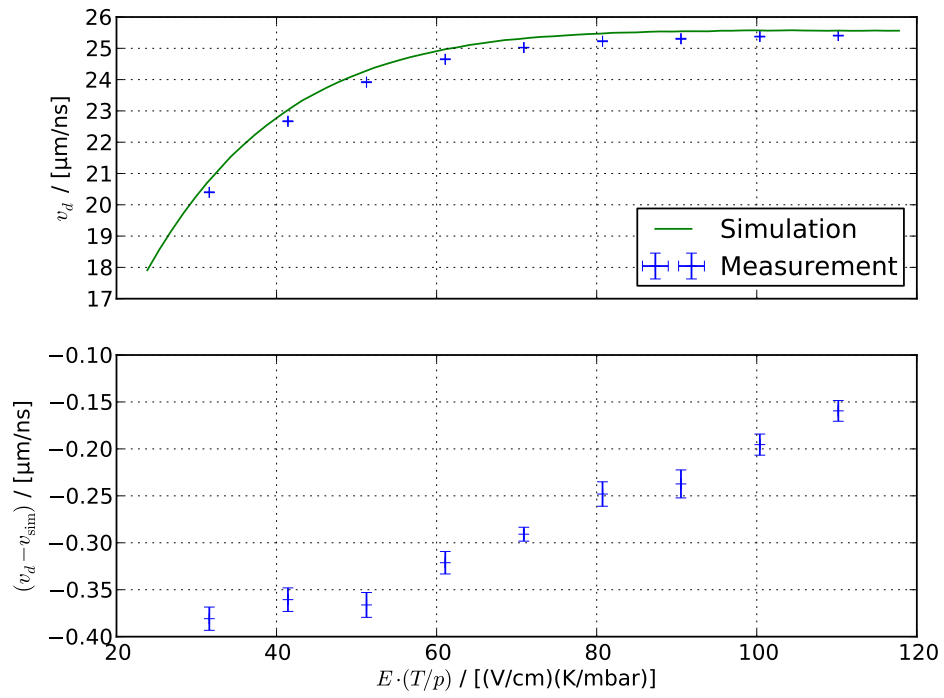


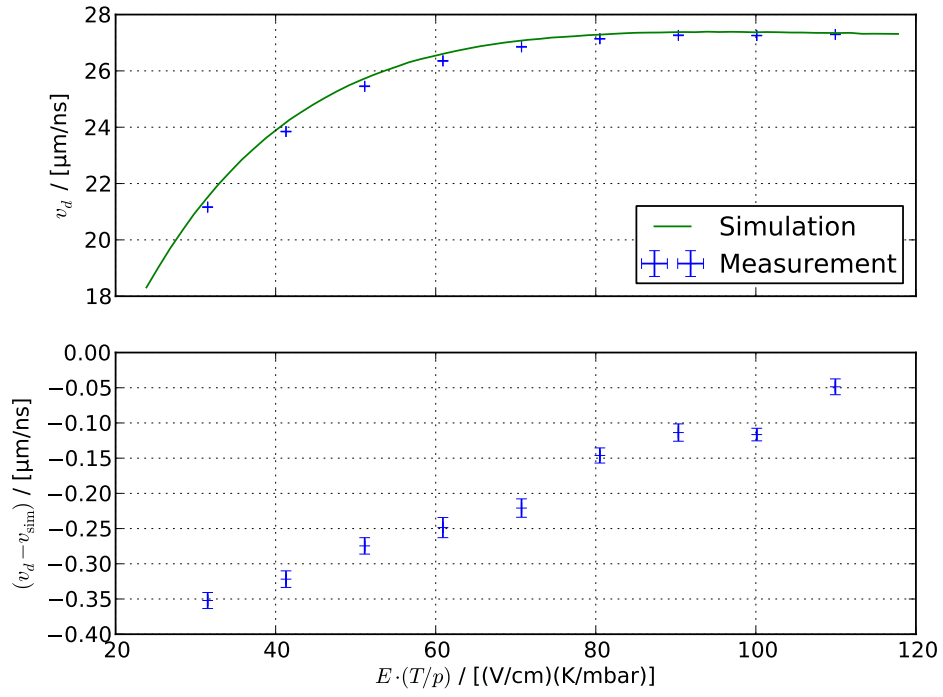
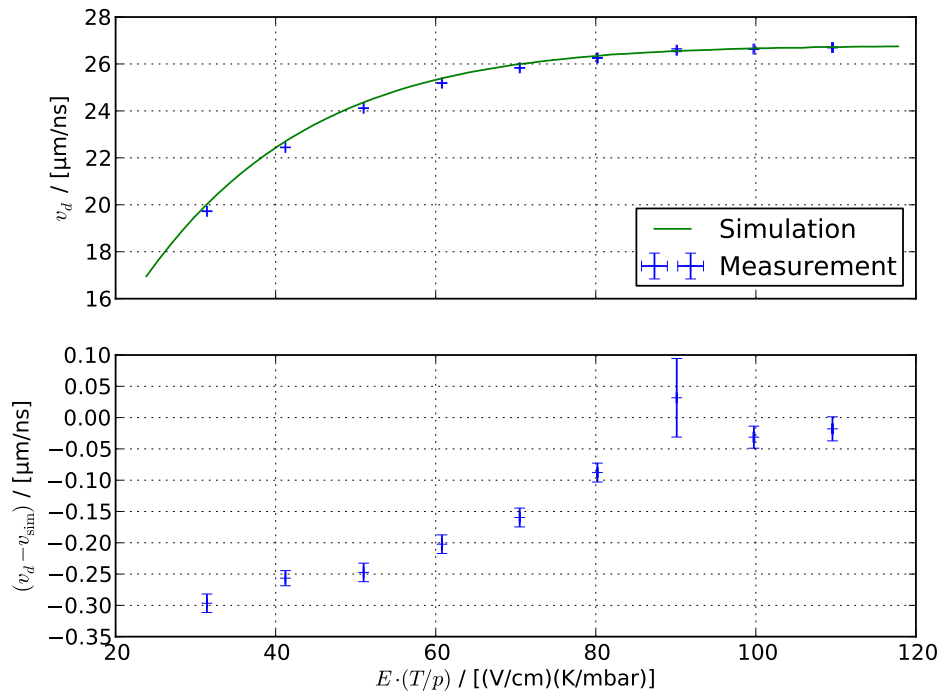
Ar 89 % – CH₄ 4 % – H₂ 7 %Ar 88 % – CH₄ 4 % – H₂ 8 %

Ar 89 % – CH₄ 5 % – H₂ 6 %

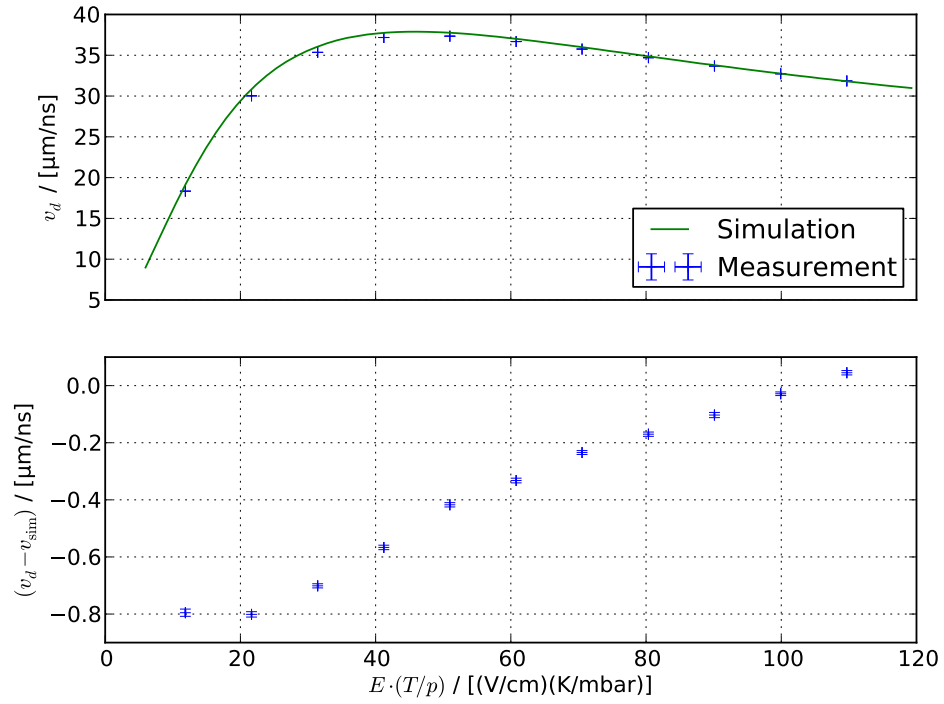


Ar 88 % – CH₄ 5 % – H₂ 7 %

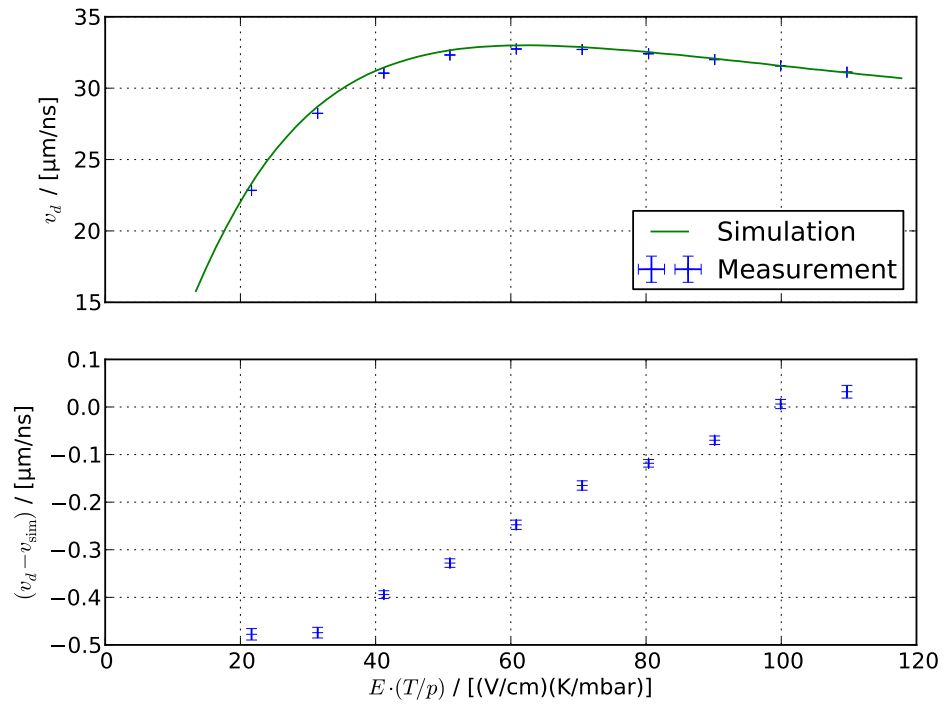


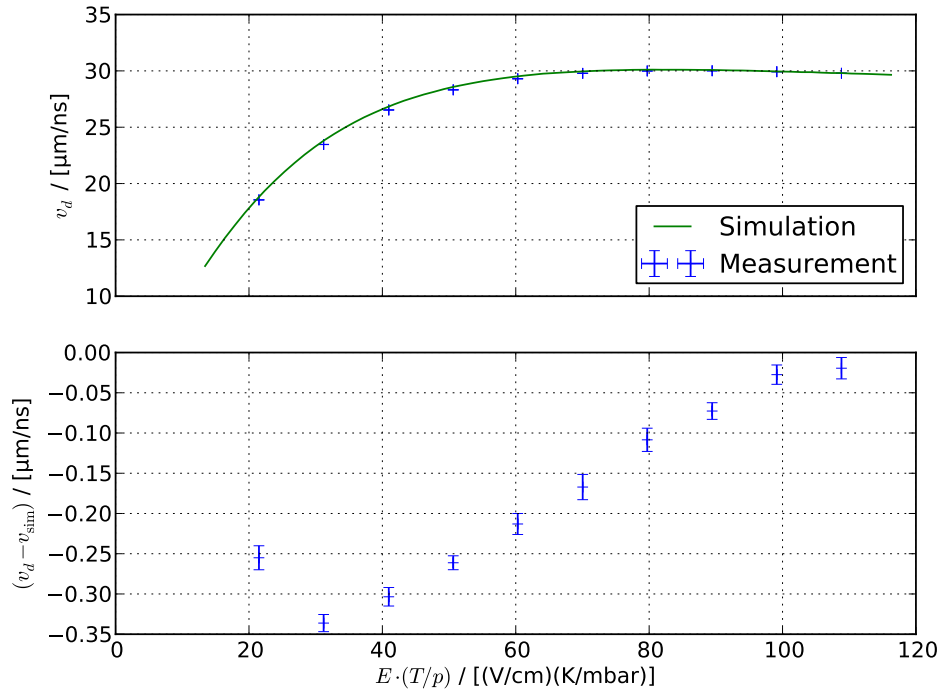
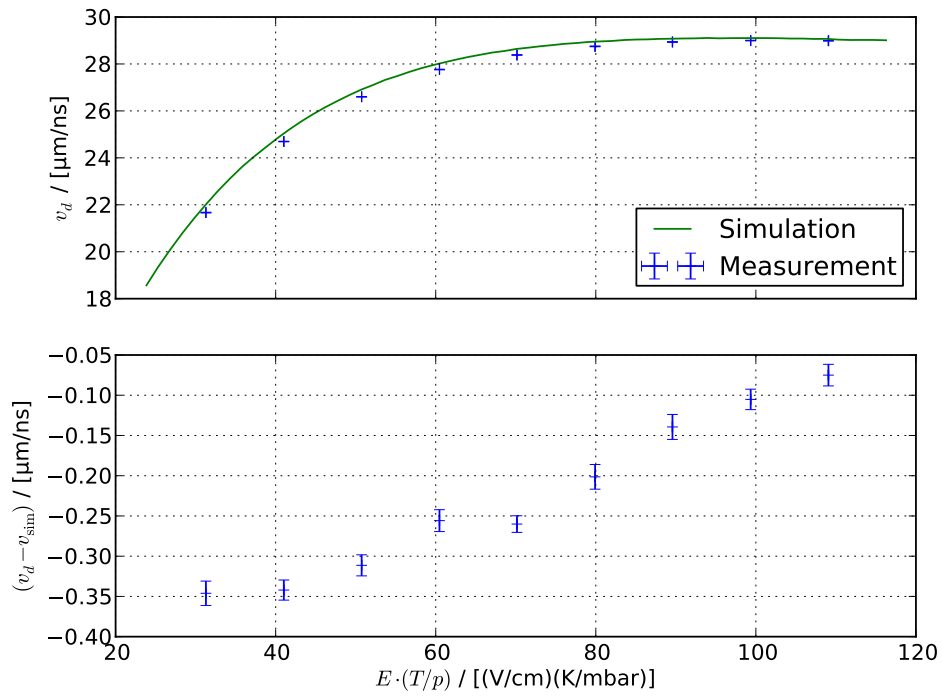
Ar 87 % – CH₄ 6 % – H₂ 7 %Ar 86 % – CH₄ 6 % – H₂ 8 %

Ar 91 % – CH₄ 7 % – H₂ 2 %

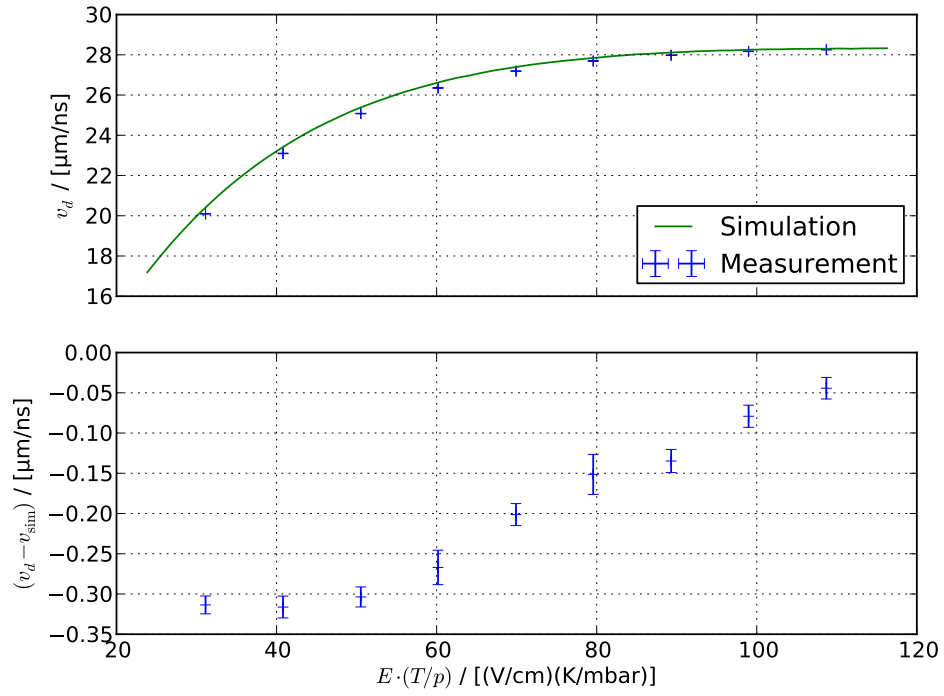


Ar 89 % – CH₄ 7 % – H₂ 4 %

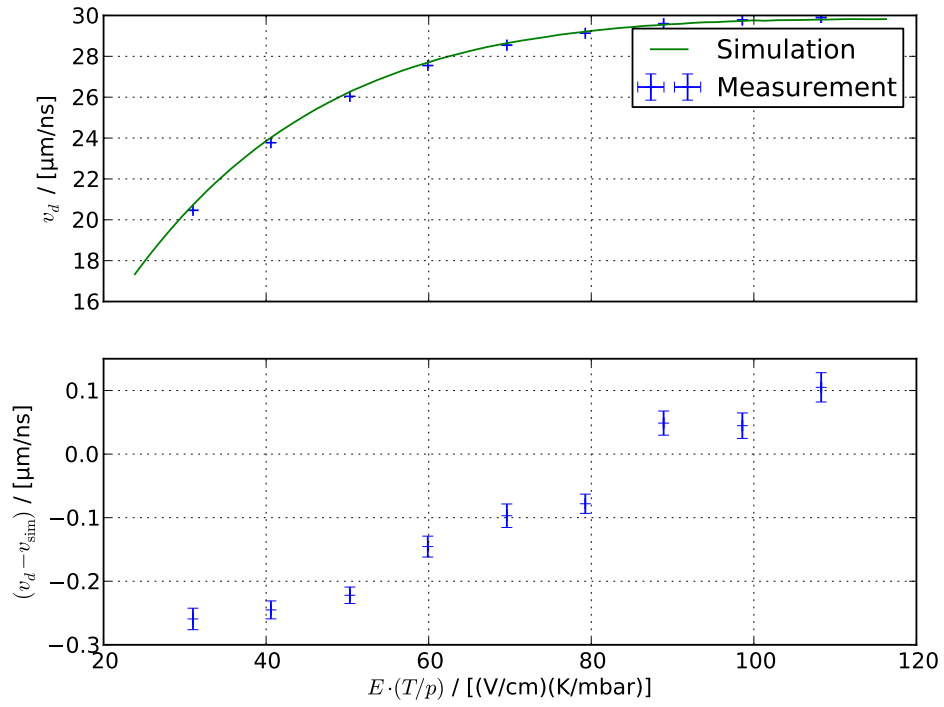


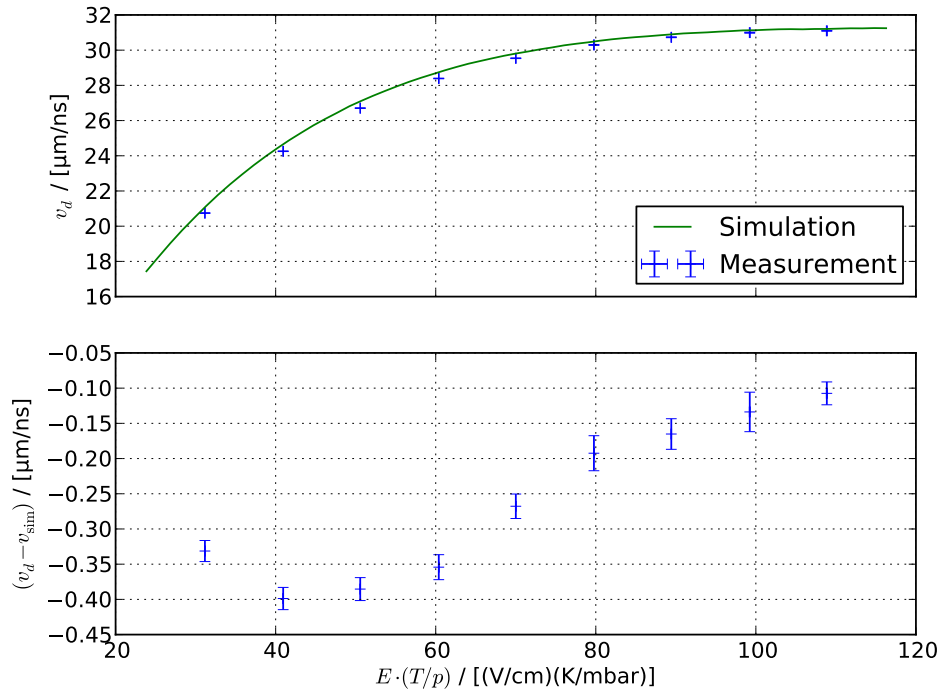
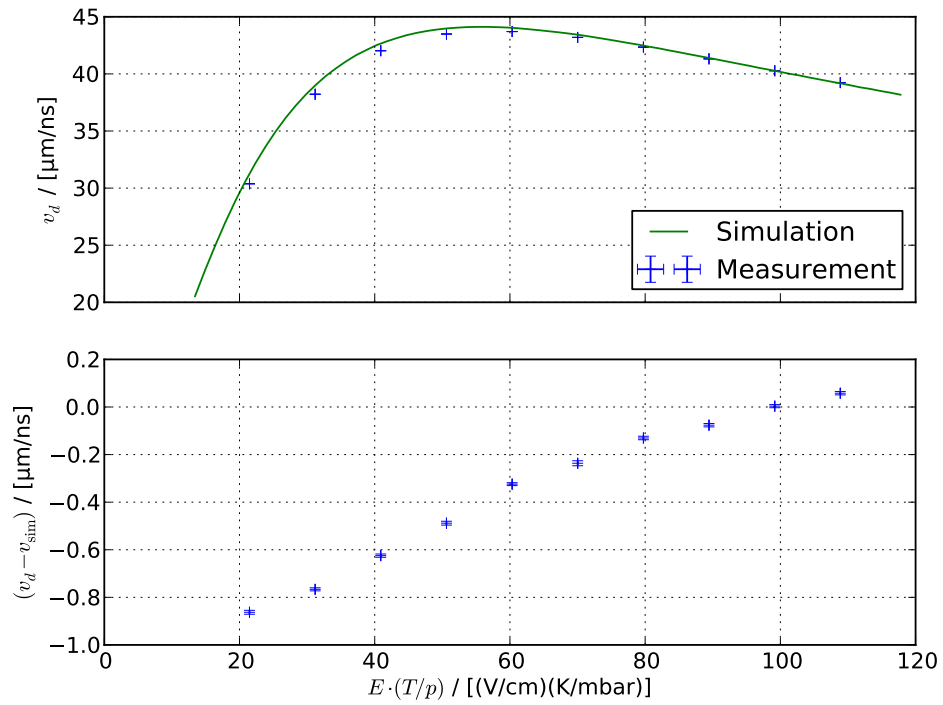
Ar 87 % – CH₄ 7 % – H₂ 6 %Ar 86 % – CH₄ 7 % – H₂ 7 %

Ar 85 % – CH₄ 7 % – H₂ 8 %

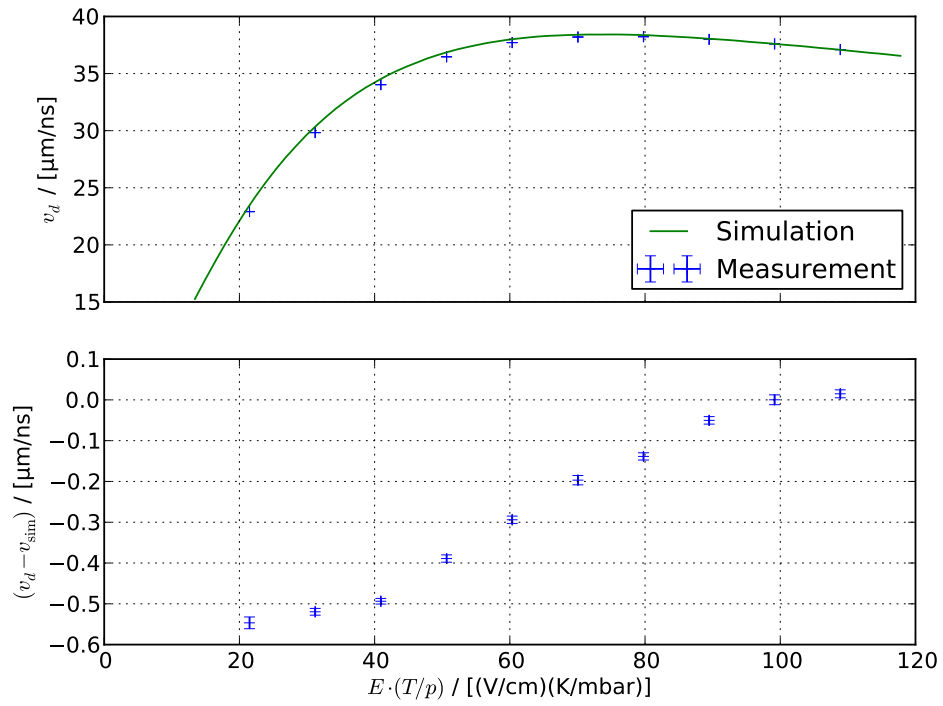


Ar 84 % – CH₄ 8 % – H₂ 8 %

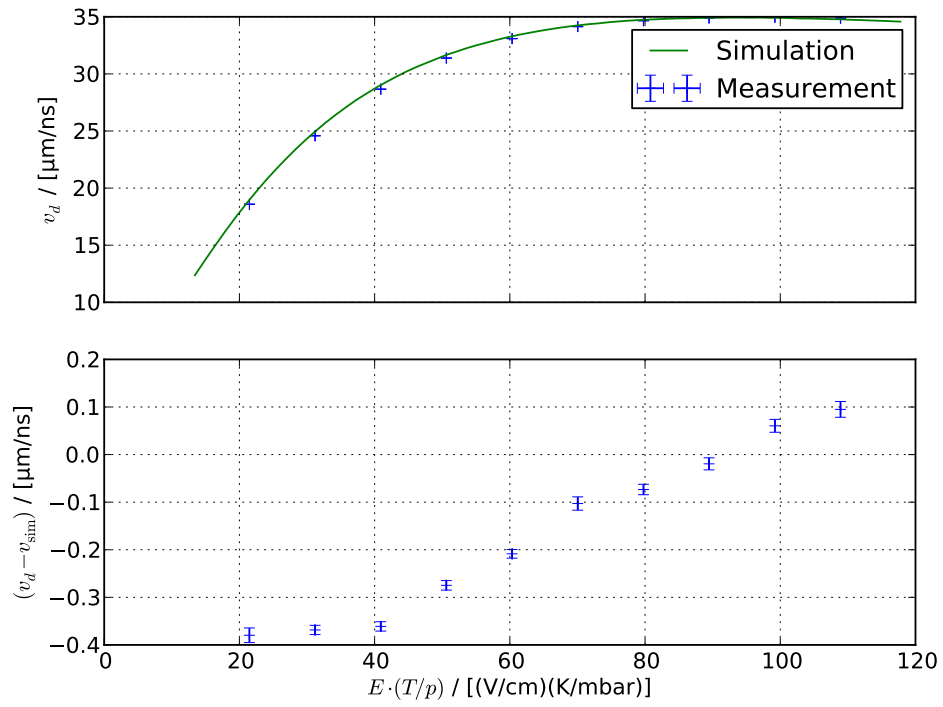


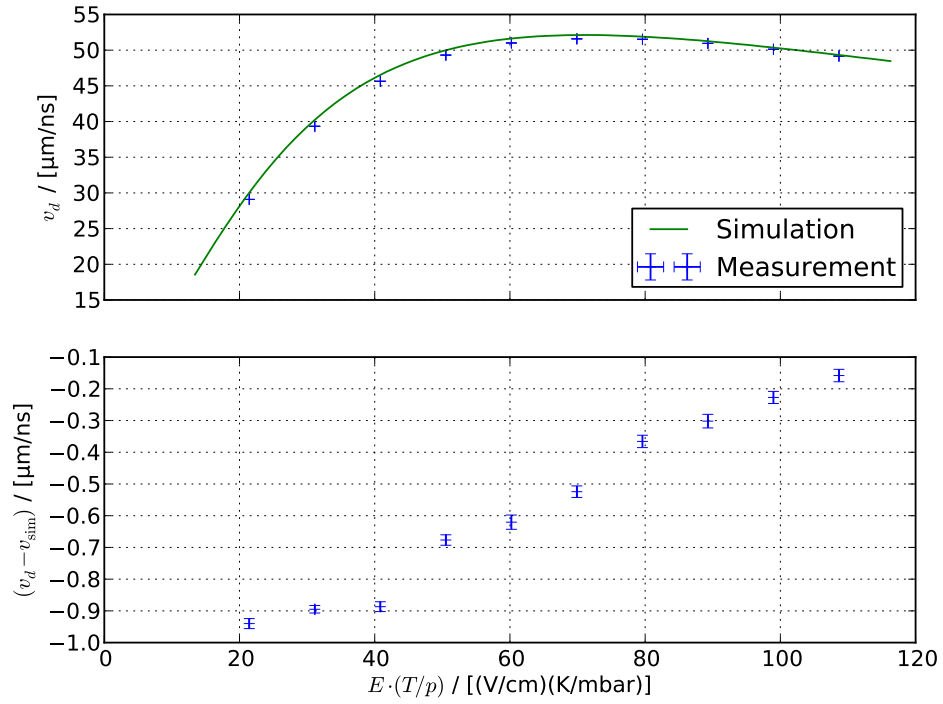
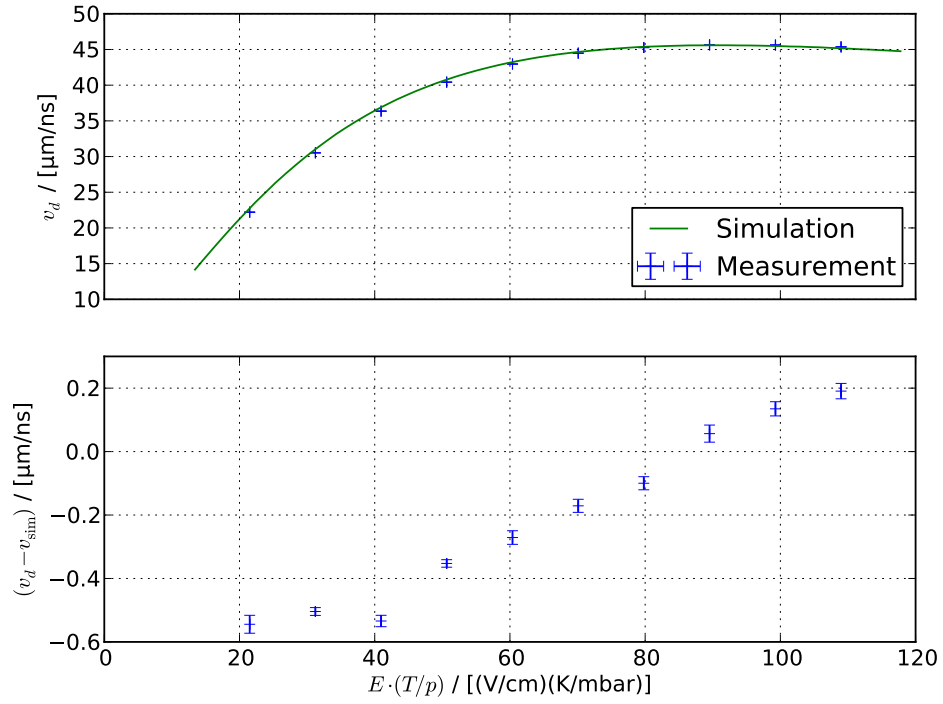
Ar 83 % – CH₄ 9 % – H₂ 8 %Ar 88 % – CH₄ 10 % – H₂ 2 %

Ar 86 % – CH₄ 10 % – H₂ 4 %



Ar 84 % – CH₄ 10 % – H₂ 6 %



Ar 83 % – CH₄ 15 % – H₂ 2 %Ar 81 % – CH₄ 15 % – H₂ 4 %

Ar 78 % – CH₄ 20 % – H₂ 2 %

